AN INVESTIGATION OF ULTRASHORT LASER PULSE MODIFICATION OF DIAMOND

AN INVESTIGATION OF ULTRASHORT LASER PULSE MODIFICATION OF DIAMOND

By

NICHOLAS A. MAILMAN, B.ScH.

A Thesis
Submitted to the School of Graduate Studies
in Partial Fulfillment of the Requirements
for the Degree
Master of Science

McMaster University

©Copyright by Nicholas A. Mailman, 2009.

MASTER OF SCIENCE (2009)
(Physics)

McMaster University
Hamilton, Ontario

TITLE: An Investigation of Ultrashort Laser Pulse Modification of Diamond

AUTHOR: Nicholas A. Mailman, B.ScH.(Acadia University)

SUPERVISORS: Dr. H. Haugen and Dr. G. Botton

NUMBER OF PAGES: xvii, 122

Abstract

This thesis reports observations of modification to single crystal CVD grown diamond irradiated with ultrashort (~150 fs), infrared (800 nm) laser pulses. The first set of experiments reports on modifications when the pulses were focused on the surface of single crystal diamond. A second set of experiments was done where pulses were focused in the bulk to study the formation of internal structures. Diamond is a dielectric material that is normally transparent to infrared radiation. However, the high intensity of femtosecond laser pulses allows for nonlinear absorption of laser radiation. The surface features that formed on diamond were studied using optical microscopy, scanning electron microscopy, and atomic force microscopy. Thin cross sections of diamond were also made using a focused ion beam (FIB) machine. These thin membranes were analyzed in a transmission electron microscope (TEM) to study modifications in the crystal structure directly below the surface of areas irradiated with ultrashort laser pulses. A FIB was also used to prepare TEM samples from areas in the bulk that had been irradiated by femtosecond laser pulses.

Surface craters were made with single femtosecond laser pulses. A ring around the edge of the single pulse craters was observed for craters made with higher pulse energies. Atomic force microscope measurements of this ring revealed it was substantially deeper than the area in the center of the crater and therefore more ablation occurred in the outer ring than in the center. This left a protrusion in the center of the crater. The formation of this ring feature was initially unexpected because the laser pulse has a Gaussian profile. More ablation might be expected to occur in the center of the crater which received a higher intensity and fluence. TEM cross sections also revealed a modified layer of amorphous carbon or polycrystalline diamond on the surface of the crater which had a very uniform thickness inside the ring or central protrusion. This modified layer was thicker underneath the deeper ring feature.

Surface craters were also made with multiple laser pulses and surface lines were made by translating the sample as it was irradiated. In these experiments ripples were observed. Two different types of ripples formed. The first type had a spacing of 550-600 nm which was slightly less than the wavelength of the 800 nm laser pulses.

Another type of ripples, with a spacing of 200-250 nm, was also observed. These higher spatial frequency ripples formed in areas which received a lower fluence/pulse such as around the edge of craters made with multiple pulses or lines made with low energy pulses. Both kinds of ripples formed perpendicular to the direction of the laser polarization. This sections of the ripples viewed in a TEM revealed the high and low spatial frequency ripples had a similar structure. The center of each ripple was unmodified diamond that was part of the main single crystal lattice. The surface of the ripples was covered with a thin, uniform layer of polycrystalline diamond, amorphous carbon or graphite. The ripples had a very smooth, sinusoidal profile instead of forming more angular grooves.

Areas inside the diamond samples were irradiated by focusing the laser pulses in the bulk of the single crystal diamond samples. The sample was translated while being irradiated to make lines within the bulk. These lines appeared as darkened areas which could be seen in an optical microscope. TEM sections revealed that cracks had formed in the bulk along the cleavage planes of diamond. These cracks contained polycrystalline material. However, no periodic structures were observed inside diamond. Other dielectrics irradiated with femtosecond laser pulses have revealed periodic structures formed in the bulk.

The results of a TEM analysis on a specimen of laser irradiated single crystal InP are shown in Appendix A. The TEM sample was made by taking a section of a crater formed with a single laser pulse. The laser pulse had a central wavelength of 800 nm and a duration of 10 fs. The irradiation was performed at the Max-Born-Institut für Nichtlineare Optik und Kurzzeitspektroskopie in Berlin, Germany. This research was in collaboration with Jörn Bonse (Bundesanstalt für Materialforschung und-prüfung, Berlin, Germany) *et al.* The crater had a central protrusion feature similar to the feature seen in diamond craters made with single laser pulses. The crater was covered in a laser modified layer made up of polycrystalline and amorphous InP. This layer was much thicker in the area under the central protrusion. There was a very sharp boundary between the laser modified layer and the unmodified InP.

Acknowledgements

I would like to thank my supervisors, Dr. Harold Haugen and Dr. Gianluigi Botton, for helping me complete this thesis. They have given me the advice and guidance needed to make this research possible. I would also like to thank them for giving me the freedom to work on things I found interesting that were not directly related to my research.

I would like to thank all of the people who helped directly and indirectly with this research. I would especially like to thank Eugene Hsu for helping me use the laser system in the photonics research lab. I would like to thank Julia Huang who spent too many hours making some of my TEM specimens. I would also like to thank my fellow researchers including Shery Chang, Henry Tiedje, Clare Armstrong, Derek Sahota, and Travis Crawford.

I would like to thank Jörn Bonse for his collaboration.

I would like to acknowledge NSERC for providing me with financial support throughout my time at McMaster.

Lastly, I would like to thank all my friends and family who supported me during my time at McMaster.

CONTENTS

LIST OF FIGURES

CHAPTER 1

Introduction

In 1905 Einstein postulated the quantization of the electric field and in 1917 he proposed the process of stimulated emission [1]. These ideas formed the theory which Maiman used in 1960 to create the first laser [2]. Since that time, lasers have been made which emit radiation over a range of wavelengths and have output intensities which can be constant in time (continuous wave lasers) or pulsate at a desired frequency. Before the invention of the laser pulses of radiation with a time duration of a few nanoseconds were produced through electrical discharges. With the development of the laser, pulses of radiation with much shorter time durations were obtained. By 1965, picosecond pulses (10^{-12} s) were possible by placing a saturable absorber inside a laser cavity. In the following twenty years, radiation pulses from lasers with time durations of less than 10 femtoseconds ($1\text{ fs} = 10^{-15}$) were achieved [1]. Ti:sapphire based laser systems that use active and passive mode-locking techniques have become one of the most common ways to generate infrared femtosecond laser pulses. The methods for generating these light pulses using Ti:sapphire based systems will be described in the experimental setup sections in Chapter 3.

The invention of the laser opened many new areas of research. Lasers allow for the creation of intense radiation which can have a high temporal and spatial coherence and a short pulse duration. One application of this unique radiation is to study its interaction with matter. Ultrashort laser pulses (less than 10^{-12} s or 1 ps) are particularly interesting for studying the interaction of radiation with matter. These pulses can carry a low energy and still achieve a very high intensity. A 1 μJ laser pulse, with a 150 fs duration, focused to a diameter of 10 μm, has a peak intensity on the order of 10^{12} W/cm^2. At room temperature, the relaxation time of electrons in most solids is on the order of 1 to 10 fs [3]. The mean free path of the electrons at room temperature is on the order of 10 to 100 nm. Therefore, the result of irradiating a sample with a femtosecond laser pulse is a highly excited and localized region of material. Material from this highly excited region is either ejected from the surface or forms a resolidified region. In most instances, both ablation and resolidification occur. However, the amount of ablation and resolidification depends on the pulse energy and the type of material. Very well defined patterning can be done as there is not enough time for heat to be transferred away from the area which is being irradiated to create a large melted region or heat affected zone [4].

Another phenomena observed on the surface of materials irradiated with laser radiation was laser induced periodic surface structures (LIPSS). These periodic structures were first noticed shortly after the invention of the laser [5]. LIPSS are believed to form due to an interference effect between the incident laser radiation and the radiation being scattered from the surface of the material being irradiated. This interference effect is only possible because of the high temporal and spatial coherence of laser radiation.

A lot of work has been done studying the ablation of metals and semi-conductors with laser radiation varying from continuous to ultrashort pulses. The formation of LIPSS on semiconductors and metals using ultrashort pulses has also been extensively studied. More recent work has also been done on dielectric materials. Dielectrics are transparent in the infrared region of the radiation spectrum. However, they will absorb intense, infrared femtosecond pulses through multi-photon processes. Recent work has also revealed that periodic structures can be created inside dielectrics when femtosecond laser pulses are focused inside these materials [6].

This thesis will report the results of experiments on both surface and bulk irradiation of single crystal diamond (a dielectric material) by infrared (800 nm) pulses with a duration of ~150 fs. Changes in the surface topography of the diamond samples due to irradiation under a variety of conditions were studied using different forms of microscopy. Modifications to the crystal structure directly under the surface have also been studied using a FIB to make samples for analysis in a TEM. Changes to the diamond crystal structure in the bulk of single crystal diamond were also analyzed using a FIB to make TEM samples from areas inside the diamond samples that were irradiated with femtosecond laser pulses.

CHAPTER 2

Background

2.1 Material Excitation and Ablation by Femtosecond Laser Pulses

2.1.1 Material Excitation and Melting

Material excitation, melting, and removal (also called ablation) happen simultaneously on materials irradiated with continuous wave laser beams or longer pulse lasers. When ultrashort femtosecond pulses are used, excitation, melting, and ablation are temporally separated. The material is excited on the order of femtoseconds. Melting occurs on the order of picoseconds, and material removal happens on the order of nanoseconds [7].

Excitation of electrons in materials by infrared, femtosecond laser pulses depends on the initial electronic structure of the material. Metals have many free carriers in the conduction band, and will absorb energy from infrared pulses through single photon absorption. In semiconductors with band gaps less than the photon energy ($h\nu = 1.55$ eV for 800 nm light), single photon absorption is the dominant process where electrons are excited from the valence band to the conduction band. In wider band gap semiconductors and dielectrics, multi-photon processes are required where the electron absorbs multiple photons to acquire enough energy to be excited above the band gap. This nonlinear process only occurs with high probabilities at higher intensities. Infrared, ultrashort laser pulses are ideal for this nonlinear process due to their inherently high intensity.

The free electrons excited to the conduction band by ultra-short laser pulses gives a dielectric more metal-like properties. These electrons can now absorb single infrared photons and through electron-electron impact ionization excite other electrons to the conduction band in an avalanche process [8]. The dominant form of excitation with femtosecond laser pulses is multi-photon absorption. Electron-electron impact ionization becomes more important for lower intensity, picosecond pulses [9]. If the energy from the laser pulse is high enough it can generate an electron-hole plasma and destabilize the crystal lattice in approximately 100 fs. This disordering is often referred to as non-thermal melting because the breakdown occurs before the lattice is heated and has reached any equilibrium temperature [7].

Thermal melting of the lattice has also been considered as a mechanism for laser induced breakdown [10]. Thermal mechanisms are considered to be more likely to occur at lower pulse energies. Thermal melting also requires more time as electron-phonon collisions must first heat the lattice. This process occurs on the timescale of picoseconds. Normally, melting would start on the surface of a material and there would be a nucleation and growth process, or a melt front, which extends through the material. The speed of this melt front has been measured up to 1000 m/s in materials such as silicon [11]. Homogeneous melting has also been considered where the entire area excited by the laser pulse homogeneously transforms from a solid to a liquid [10].

2.1.2 Ablation

At low intensities, the irradiation of matter by laser radiation can be modeled by a two temperature model where the electrons and lattice are both in a thermal equilibrium. Energy is absorbed by the electrons and transferred to the lattice through electron-phonon interactions. The heat capacity of the electrons is much less than the lattice. Heat is transferred away from the irradiated area by mobile electrons and phonons [12]. Melting may occur and some evaporation depending on the intensity of the pulse.

Femtosecond pulses are more likely to cause a direct transition from solid to vapour where ablation has occurred [13]. The rapid heating does not allow for a thermal equilibrium to be reached, and thermodynamic models involving an equilibrium temperature do not apply. Materials have been shown to behave similarly when irradiated with femtosecond laser pulses because the time for substantial melting or heat diffusion is much longer than the time taken for the pulse to deposit energy. Also, most materials will absorb energy from infrared laser pulses due to non-linear processes. In any solid, the same general mechanisms are then believed to be responsible for material ablation by femtosecond laser pulses [14].

Many possible mechanisms have been considered for the ablation of solids by ultrashort pulses. Some of these mechanisms are outlined in Refs. [14] and [15]. These mechanisms include phase explosion, or homogenous nucleation, where a superheated fluid is created. Gas bubbles will form in this liquid and expand. These bubbles will eventually rupture and material will be ejected from the solid [10]. Vaporization, where laser energy is higher than the cohesive energy of the solid and atoms are atoms are simply ejected from the surface has also been considered.

Another mechanism which has been considered to cause ablation and nanostructuring on insulators and semi-conductors irradiated with femtosecond laser pulses is Coulomb explosion [16]. Coulomb explosion is caused by the laser pulse creating a charged surface due to the emission of free electrons. Electrons absorb photon energy which is turned into kinetic energy. As the electrons move away, they leave behind charged atoms. Electrostatic Coulomb repulsion between the charged atoms causes the lattice to destabilize and leads to what is known as a Coulomb explosion. This process only occurs at lower fluences where a dense plasma is not generated [17]. At lower laser fluences, nanoparticles were observed on 3C-SiC. The origins of these particles were thought to be due to nano-craters created by Coulomb explosions on the surface of 3C-SiC which could be seen as a nanoparticle patterning on the surface of the material[18].

2.2 Laser Induced Periodic Surface Structures

2.2.1 Theories on LIPSS Formation

Shortly after the invention of the laser, Birnbaum, using a ruby laser, observed the formation of ripples on the surface of germanium [5]. Up until this point, it was assumed that ablation by continuous wave lasers and laser pulses would create craters with only random features. Any periodic structures were then attributed to properties of the irradiating laser. These ripples or laser induced periodic surface structures (LIPSS) were first assumed to form because of diffraction effects caused by the lens used to focus the laser. The effect of diffraction through a circular aperture which is smaller than the width of the laser beam is to create an intensity pattern which oscillates between zero and some decreasing maximum as the square of the first order Bessel function. The periodic structures were then thought to be created by the oscillatory nature of the laser beam intensity along the sample surface as it would no longer be Gaussian [5].

It was soon found that LIPSS were more of a universal phenomena related to the interaction of laser radiation and the surface of materials. LIPSS were observed and reported on a Ge etalon used as an output coupling mirror in a CO_2 laser operating at a wavelength of 10.6 μm [19]. The effects of diffraction in the laser beam would not be a plausible reason for the creation of these ripples inside the laser cavity. A theory was presented which assumed LIPSS were caused by a surface scattering wave

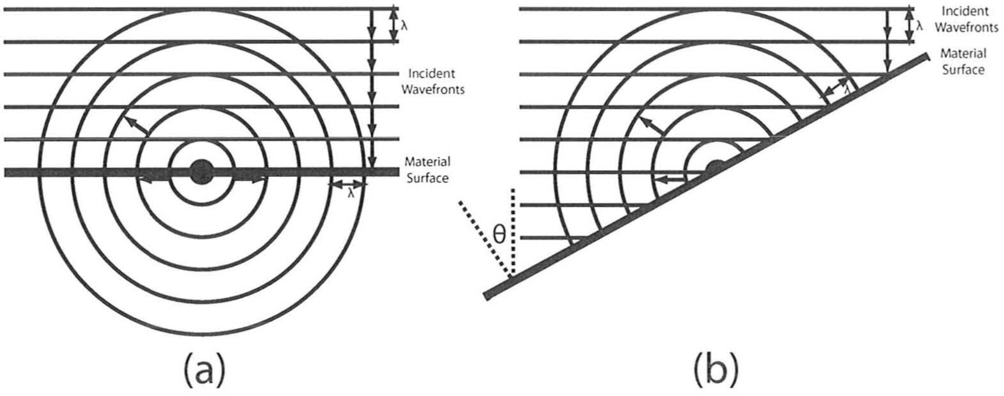

Figure 2.1: Schematic illustrating interference between the incident laser light and a surface scattering wave when the surface is normal to the propagation vector for the incident pulse (a) and at an angle (b).

created by the laser beam. The ripples occur due to variations in intensity along the sample surface caused by interference between this scattering wave and incident laser beam. The interference creates a standing wave as illustrated in Figure 2.1a. More ablation will occur at the anti-nodes and leads to the formation of ripples. The spacing of anti-nodes (the period of LIPSS) is

$$d = \lambda \tag{2.1}$$

for normal incidence. If the sample surface is at an angle, this theory would predict a spacing of

$$d = \frac{\lambda}{1 \pm \sin(\theta)} \tag{2.2}$$

where the (+) sign applies to the area left of the scattering center and the (-) sign applies to the area right of the scattering center for the configuration shown in Figure 2.1b. Experiments performed on Ge produced LIPSS with a spacing that followed this formula [19]. LIPSS were later observed on acrylic plastic and fused silica using 10.6 μm laser light with a 0.5 μsec equivalent square pulse width [20]. These LIPSS formed elliptical damage rings which were expected from the surface scattering wave theory presented by Emmony [19]. They also observed surface defects in the center of many of these ring patterns at lower fluences where there was little modification to the original surface. These observations supported the theory of a surface scattering wave.

LIPSS had now been observed on metals, semiconductors, and dielectrics irradiated over a range of radiation conditions. The theory of LIPSS formation on dielectrics was further expanded by Temple and Soileau [21]. In dielectrics local electric field enhancements during laser irradiation had been considered by Bloembergen [8]. He showed the role played by submicroscopic surface structures such as cracks and pores smaller than the laser wavelength accounted for the lowering of the breakdown intensity by a factor of 4 to 5 on the surface as compared to in the bulk of materials such as glass and sapphire. Temple and Soileau used this theory to create a model for optical breakdown in dielectrics. They assumed polarization charges induced on the surfaces of these defects from the electric field of the laser created a perturbation field with a period of

$$d = \frac{\lambda}{n} \tag{2.3}$$

where λ is the wavelength of the incident radiation in air. Temple and Soileau observed this spacing on NaCl irradiated with 200 ns laser pulses. This equation for LIPSS spacing in dielectrics would also be predicted by the simple model from Figure 2.1 if the surface scattering wave was assumed to move through the dielectric. However, this theory did not explain how multiple pulse craters and lines made with laser pulses were later seen to form parallel lines instead of concentric rings when linearly polarized light was used. The effects of polarization which change the direction of the LIPSS also could not be adequately explained.

Isenor *et al.* [22] observed the formation of ripples on $Ni_{0.8}P_{0.2}$ irradiated with with $\sim$50 ns pulses from a CO_2 laser. They found by varying the incident angle the period of the ripples changed according to Equation 2.2. However, this was only for π polarized light. If the light was σ polarized (E parallel to the sample surface) then there was no such variation and the spacing remained at approximately the incident laser wavelength. Ripple patterns were also found to rotate with the plane of polarization on Si [23] and the circular LIPSS pattern predicted by the simple surface scattering theory was only seen when using circularly polarized light.

It was found that LIPSS were a universal phenomena by Sipe *et al.* who observed ripples on a variety of materials including Ge, Si, Al, and brass using 0.53 μm and 1.06 μm wavelength laser pulses with a 15 ns pulse duration [24]. The LIPSS which formed on these materials were all equal to the wavelength of the laser. One important observation they found was ripples could be formed with a single pulse. They also found that ripple patterns could be altered if a defect or scratch was present as observed by other groups such as Emmony *et al.* [19]. However, for multiple pulses they found that a pattern emerged which did not change after about 20 pulses and did not depend on the initial surface conditions.

Sipe *et al.* presented what is currently the most widely accepted theory for LIPSS formation. Sipe theory is also based on a surface-scattered electromagnetic wave similar to the theories presented when LIPSS were initially discovered. However, Sipe took into account the interaction of the electromagnetic laser beam with a microscopically rough surface, and included the excitation of surface polaritons. Sipe theory uses a response function, η, to describe the rate of inhomogeneous energy absorption on the surface of a sample. It is also referred to as the efficacy factor for inhomogeneous energy absorption. This response function depends on the angle of incidence, wavelength, and polarization of the incident laser as well as the periodicity of the initially rough surface. It was found that the location of peaks in the response function were mostly independent of the initial surface conditions. Very sharp peaks were found to occur in the response function for particular surface roughness periods, Δ (the spatial period at which ripples or LIPSS will form). The period of LIPSS was predicted to be

$$\Delta_{\pm} = \frac{\lambda}{1 \pm \sin(\theta)} \tag{2.4}$$

for LIPSS or ripples perpendicular to the laser polarization. This equation gives the same spacing as Equation 2.2. However, Sipe theory also predicts possible spacings of

$$\Delta_{\pm} = \frac{\lambda}{n \pm \sin(\theta)} \tag{2.5}$$

which are more dominant for transparent dielectrics. Another type of LIPSS, designated c type ripples, with a spacing of

$$\Delta_c = \frac{\lambda}{\cos(\theta)} \tag{2.6}$$

were also predicted by this theory and had been previously observed [4]. These LIPSS are predicted to be parallel to the laser polarization and are not as common as LIPSS which are perpendicular to the laser polarization.

2.2.2 High Spatial Frequency LIPSS (HSFL)

The LIPSS described in the previous section all had periods on the order of the laser wavelength or $\frac{\lambda}{n}$ for normal incidence. They can be designated as low spatial frequency LIPSS (LSFL). However, in more recent studies of materials irradiated with picosecond and femtosecond pulses, LIPSS with spacings which can be much smaller than the wavelength of the laser or $\frac{\lambda}{n}$ have been reported [25]. These high spatial frequency LIPSS (HSFL) have been observed mainly on dielectrics and semiconductors with bandgaps larger than the incident photon energy [26].

The formation of HSFL and LSFL has been observed to depend on the pulse energy - or more importantly the fluence. Borowiec *et al.* [27] observed both HSFL and LSFL on InP using 2100 nm, 50-100 fs laser pulses. They observed LSFL on InP were most prevalent on areas irradiated with multiple pulses where each pulse had a fluence close to the threshold fluence required for modification by a single pulse. HSFL were observed on the edge of craters made with multiple femtosecond pulses where the fluence per pulse was far below threshold. HSFL could be seen using 1300 and 2100 nm laser pulses which have an energy less than the bandgap of InP (1.35 eV). At 2100 nm, the HSFL had a period of 430 nm ($\sim \lambda/4.9$). This value is also less than $\frac{\lambda}{n}$ (the index of refraction for InP is n$\sim$3 for 2100 nm light). HSFL could not be seen using 800 nm laser pulses where the photon energy was above the band gap. One possible theory for HSFL formation is second harmonic generation (SHG) on the surface due to initial defects and the surface boundary.

HSFL have also been observed on a number of wide band gap dielectrics [28, 29].

The HSFL observed on these dielectrics had periods which were more than a factor of two below the laser wavelength and did not correspond with a $\frac{\lambda}{n}$ spacing. Using Sipe theory and taking into account SHG does not give an explanation for the formation of these structures. It was also found that the spacing of the HSFL was more dependent on the laser pulse fluence than the laser pulse wavelength. A simple "self-assembly" model was suggested as the mechanism for HSFL formation [29]. In this model the femtosecond laser pulse creates an instability in the crystal lattice which relaxes after several hundred femtoseconds. The excitation results in surface ionization, Coulomb explosion and ablation which also occur on the order of several hundred femtoseconds. The remaining crystal is not in equilibrium and relaxation will not occur in a slow equilibrium thermalization. The surface has been roughened by Coulomb explosion will relax through reorganization and probably atomic diffusion which will result in self-organization in the form of periodic structures. However, this model does not take into account the effect of polarization on the direction of ripples or explain the correlation between the period of LIPSS and the laser wavelength.

It has also been observed that LSFL have a period which is always slightly less than the laser wavelength on semiconductors such as InP, GaP, GaAs and dielectrics such as sapphire irradiated with femtosecond laser pulses. The theory presented by Sipe *et al.* cannot reconcile this difference. A theory for the formation of LSFL with periods slightly below the laser pulse wavelength and HSFL has been presented more recently by Dufft *et al.* after observing LSFL and HSFL on ZnO [26]. Their experiment used 800 nm, 200 fs laser pulses incident normal to the surface of a ZnO sample. LSFL with a period of 680 to 730 nm and HSFL with a period of 230 nm were observed. HSFL became more dominant for higher numbers of low energy pulses incident on the same area. If higher energy laser pulses were used only LSFL were observed except for around the outer rim of craters where HSFL were present because the fluence was lower in this region. To account for the period of these LIPSS, a nonlinear version of Sipe theory on ripple formation was used. First, a Drude model was used to take into account changes in the refractive index, $\tilde{n} = n + ik$, due to free carriers in the conduction band. Changes in the refractive index due to the Kerr effect were found to be so small that they were ignored. Sipe theory that incorporated changes in the dielectric constant was then used. The efficacy factor, η, was calculated for different carrier excitations. Dufft *et al.* found peaks in η for 800 nm radiation that ran perpendicular to the polarization with a spacing that varied only sightly from ~800 nm over a range of carrier concentrations. These were concluded to be the cause of the LSFL. At higher carrier densities the amplitude of η decreased. This would explain the general disappearance of LIPSS at higher fluences.

Dufft *et al.* argue SHG is closely related to the formation of HSFL. It was observed using a linear polarizer and spectrometer that ZnO produced 400 nm light due to SHG when excited with a 800 nm pulse. The polarization of the 400 nm light was also found to be mainly perpendicular to the original 800 nm pulses. The efficacy factor for 400 nm light taking into account the free carrier concentration was found to have peaks with a spacing of ~200 nm that ran parallel to the SHG 400 nm light (perpendicular to the original 800 nm light). They attributed these peaks to the HSFL that had a period of 200-280 nm observed running perpendicular to the incident 800 nm laser pulses.

The dependence of the formation of HSFL or LSFL on the laser fluence was also explained by taking into account the number of free carriers. It was found that at carrier densities greater than ~5×10^{21} cm^{-3}, the extinction coefficient, k, for ZnO became quite large as in metals for 800 nm light. Only LSFL were observed because the pulses were either absorbed or produced scattered surface electromagnetic waves which interfered with the incident pulse and were also highly absorbed. This also explains why HSFL are generally not observed on metals which already have high free carrier densities. If the carrier densities were around 3×10^{21} to 5×10^{21} cm^{-3} and the laser intensity was still strong enough for SHG to occur, it was found that 400 nm light could still advance through the free electron plasma. HSFL would be produced because light created by SHG on the surface and transmitted slightly into the bulk would interfere with light created by SHG and scattered along the surface. This also explains why HSFL are generally observed for shorter, subpicosecond pulses. The intensity is high enough for SHG to efficiently occur but the overall fluence is not too large to create a metallic like state [26]. HSFL have been observed on gallium phosphide using pulse durations up to 80 ps which would not be as efficient at SHG. However, many pulses were required to form HSFL at this pulse duration and for pulse durations of 130 ps and longer only LSFL were observed [30].

2.3 Laser Induced Periodic Bulk Structures

Most work on the modification of materials by femtosecond laser pulses has been done by irradiating the sample surface and studying changes in the topography of the sample. However, recent work has revealed that laser induced periodic structures can also form in the bulk of dielectrics irradiated with femtosecond laser pulses. Shimotsuma *et al.* observed periodic planes in synthetic silica glass (amorphous SiO_2) after irradiation by 800 nm, 150 fs laser pulses focused 100 μm inside the sample [31]. The formation of these periodic structures was also attributed to an interference effect. However, it was argued that the electric field from the bulk electron plasma wave is what interferes with the incident laser light. The planes were perpendicular to the laser polarization and ~20 nm wide. The planes were observed in an SEM using backscattered electron images. Auger spectra mapping revealed the planes were deficient in oxygen. The grating periods were observed to change with the number of pulses. For a pulse energy of 1 μJ, with an intensity of 2×10^{14} W/cm^2, it was observed for 5×10^4, 20×10^4, and 80×10^4 pulses irradiating the same area that the spacing of the planes decreased from 240, 180 to 140 nm respectively. Also, it was observed using a constant 20×10^4 pulses with pulse energies of 1, 2, and 2.8 μJ that the grating periods increased from 180, 240, to 320 nm respectively. Using an electron plasma wave model, the observed increase in spacing could be explained by higher electron concentrations and temperatures [31].

Corkum *et al.* also showed that periodic planes could be produced inside fused silica by focusing femtosecond laser pulses in the bulk of samples [6]. The samples were irradiated using a Ti:sapphire laser system, which produced 800 nm, 50 fs laser pulses at a repetition rate of 100 kHz. The samples were then etched in HF and nanoplanes that etched at a much faster rate could be seen using an AFM or SEM. The planes were $\leq$ 10 nm wide and formed perpendicular to the direction of the laser polarization. The spacing of the planes was ~242 nm and did not change over the range of pulse energies used. These planes were not produced with circularly polarized light.

The planes observed by Corkum *et al.* were believed to form because small areas of plasma were created inside fused silica by the laser pulses. Local field enhancements around the plasma created the coherent structuring (nanoplanes) revealed by etching. These planes could not have formed out of a large area of plasma because energy from the laser pulses was not high enough to turn the entire region the planes were observed into a plasma. Instead, it was proposed the formation of these planes after irradiation with multiple low energy pulses was due to the inhomogeneous absorption of energy through color centers formed by the initial pulses or defects that were already present in the fused silica samples. The subsequent pulses were more strongly absorbed at these centers and, along with an avalanche effect, create small areas of plasma [6].

The displacement of an electron from its equilibrium position, $\vec{x}$ when experiencing an external harmonic electric field, $\vec{E}$, of frequency, $\omega = 2\pi f$, is given by

$$m\frac{d^2\vec{x}}{dt^2} = -e\vec{E} = -m\omega^2\vec{x}. \tag{2.7}$$

This equation assumes there is no collisions or other resistances to motion, and therefore a temperature of absolute zero so there is no thermal aggregation. If there are N electrons per unit volume the net dipole moment, $\vec{P} = -Ne\vec{x}$ is

$$\vec{P} = -\frac{Ne^2}{m\omega^2}\vec{E}. \tag{2.8}$$

The electric displacement is then given by

$$\vec{D} = \epsilon_0\vec{E} + \vec{P} = \epsilon_0\left(1 - \frac{Ne^2}{m\omega^2\epsilon_0}\right)\vec{E} = \epsilon_0\left(1 - \frac{\omega_p^2}{\omega^2}\right)\vec{E}. \tag{2.9}$$

Where plasma frequency, f_p, is given by

$$f_p = \frac{\omega_p}{2\pi} = \frac{1}{2\pi}\sqrt{\frac{Ne^2}{m\epsilon_0}}. \tag{2.10}$$

If the frequency of the radiation is less than the plasma frequency ($f < f_p$) the effective relative permittivity of the plasma will be negative. The index of refraction will be completely imaginary and the laser radiation is completely reflected. For $f > f_p$, electromagnetic waves can move freely through the plasma without attenuation. The carrier density required for the plasma frequency to be the same frequency as 800 nm radiation is

$$N = \frac{4\pi^2 m\epsilon_0}{e^2}\frac{c^2}{\lambda^2} = 1.75 \times 10^{21} cm^{-3}. \tag{2.11}$$

At free carrier densities above this value, 800 nm light is completely reflected. For densities less than this value, 800 nm light is transparent to the plasma based on this simple model for the propagation of light through a plasma.

Returning to the mechanism proposed by Corkum *et al.*, the nanoplasmas would initially be underdense, $N < 1.75 \times 10^{21}\mathrm{cm}^{-3}$. The boundary conditions for a sphere of underdense plasma requires the electric field to be enhanced around the equator of the pulse compared to the poles where it is suppressed (a line connecting the poles would be parallel to the direction of polarization). This enhancement in the electric field will cause the spheres of plasma to form into planes perpendicular to the laser polarization. With subsequent pulses the defects caused by plasma generation will cause stronger absorption in areas where plasma has already formed leading to a positive feedback loop. Plasma with electron densities above the critical density can form. These reflective planes will act similar to planar metal waveguides. It is argued that the spacing of the planes which is $\sim(\lambda_0/2n_{800}{=}276$ nm), ($n_{800} = 1.45$ for fused silica) is the same as the minimum spacing required in a planar metal waveguide with field maxima at the interface of the diamond-plasma surfaces. Only planes with this spacing that supports modes which reinforce their own growth will develop.

2.4 Determining the Laser Spot Size

The total energy output from a laser can be accurately determined using radiation power meters. However, the irradiance and overall fluence that is incident on the surface of sample is much harder to determine. Much more must be known about the spatial profile of the incident laser beam. Often, the laser beam is manipulated by a series of lenses, such as microscope objectives, to focus the beam. A simple, *in situ* method for measuring the spot size, w_0, was proposed by J. Liu [32]. This method assumes the laser pulse has a Gaussian profile. The incident intensity as a function of time and space is then given by

$$I(r,t) = I_0 e^{-2r^2/w_0^2} e^{-t^2/\tau^2}. \tag{2.12}$$

In this equation, I_0 is the peak intensity, r is the distance from the center of the beam, and w_0 is the distance from the center where the intensity drops to $1/e^2$ the peak intensity (the $1/e^2$ spot size which will be used throughout this thesis). τ is related to the pulse duration. Methods for measuring the pulse duration will be outlined in Section 3.4.1.

The spatial distribution of the fluence can be found by integrating the intensity over time to give

$$\phi(r) = \int_{-\infty}^{\infty} I(r,t)dt = \underbrace{I_0\sqrt{\pi}\tau}_{\phi_0} e^{-2r^2/w_0^2}, \tag{2.13}$$

where ϕ_0 is the maximum fluence experience by the irradiated sample at the center of the laser pulse. Materials, such as Si, when irradiated with laser pulses form craters and amorphous ring patterns due to ablation and melting by laser pulses. The formation of these patterns and craters occurs at a threshold fluence, ϕ_{th}, for a particular pulse duration. If the threshold fluence for a feature, such as an amorphous ring, is a distance r_a from the center of the laser pulse then

$$\phi_{th} = \phi_0 e^{-2r_a^2/w_0^2}. \tag{2.14}$$

Equation 2.14 can be rearranged to give

$$r_a^2 = \frac{1}{2} w_0^2 \left(\ln \phi_0 - \ln \phi_{th}\right). \tag{2.15}$$

This equation gives a method for determining the laser spot size by plotting the radius squared of a circular feature versus the logarithm of the peak fluence for different pulse energies. The slope of the straight line fit can then be used to determine w_0. However, it is not possible to directly measure ϕ_0. Instead the total energy, E_{tot}, from an entire pulse is measured. This quantity can be related to the peak fluence through the equations

$$E_{tot} = \int_{-\infty}^{\infty}\int_{-\infty}^{\infty} \phi_0 e^{\frac{-2\left(x^2+y^2\right)}{w_0^2}} dxdy = \frac{\phi_0 \pi w_0^2}{2}, \tag{2.16}$$

$$\phi_0 = \frac{2E_{tot}}{\pi w_0^2}. \tag{2.17}$$

Often the diameter, $D = 2r_a$, is measured instead of radius. The final equation where plotting D^2 versus $\ln E_{tot}$ gives a straight line equation with a slope of $2w_0^2$ is

$$D^2 = 2w_0^2 \left\{ \ln\left(E_{tot}\right) + \ln\left(\frac{2}{\pi w_0^2}\right) - \ln\left(\phi_{th}\right) \right\}. \tag{2.18}$$

This method for determining w_0 is called the D-squared method. The intercept can then be used to determine the threshold fluence for the ablation feature.

The above equations assume the incident fluence has a cylindrically symmetric Gaussian distribution. However, elliptical pulses and craters are often produced by laser systems. A more thorough method would be to measure a spot size for the major and minor axes of the elliptical pulse [33]. However, averaging the diameter of the major and minor axes should minimize this error. If the ellipticity of the crater is moderate to high then the geometric average of the crater diameters should be used instead of the arithmetic average. The geometric average is equal to the radius of a circle that has the same area as the ellipse. The arithmetic average is always greater than or equal to the geometric average.

Errors in spot size measurements when high band gap materials were used to measure the spot size have also been reported by Bonse *et al.* [34]. It was observed that the use of high band gap materials to measure the spot size can lead to a measured spot size which is smaller than the actual spot size. Bonse argued that for the method presented by Liu to be accurate there must be linear absorption at the laser photon energy used. For 800 nm light ($h\nu = 1.55$ eV), this would require materials with a band gap less than 1.55 eV. Bonse measured the spot size of pulses produced on a laser system using fused silica ($E_g = 7.2$ eV) and then $Ge_2Sb_2Te_5$ ($E_g = 0.5$ eV). The spot size measured using $Ge_2Sb_2Te_5$ was 16% larger than the spot size measured using fused silica. Moderate band-gap materials, such as borosilicate glass (E_g = 4 eV), were also noted to provide correct values.

Materials with high band gaps compared to the photons from the incident laser must absorb through non-linear, multi-photon processes. If the threshold intensity for a feature is considered instead of the fluence, using equation 2.12 the threshold intensity is

$$I_{th}(r_{th}, 0) = I_0 e^{-2r_{th}^2/w_0^2}. \tag{2.19}$$

The intensity was taken at $t = 0$ because any other time the intensity would be below threshold at r_{th}. Rearranging this equation to a form similar to equation 2.18 gives a linear fit for determining the spot size using the peak intensity instead of the fluence according to the equation:

$$D^2 = 2w_0^2 \left(\ln I_0 - \ln I_{th}\right). \tag{2.20}$$

The value of I_0 can be determined from E_{tot} as well from equations 2.13 and 2.17 giving

$$I_0 = \frac{\phi_0}{\sqrt{\pi}\tau} = \frac{2E_{tot}}{\pi^{3/2} w_0^2 \tau}. \tag{2.21}$$

As I_0 and ϕ_0 are linearly related plotting D^2 versus the logarithm of either I_0 or ϕ_0 will give a linear fit with a slope of $2w_0^2$. For multi-photon processes, the threshold is related to some higher power of the intensity, ξ. The threshold as a function of distance from the center of the Gaussian laser beam is then given by

$$I_{th}^{\xi} = I_0^{\xi} e^{-2\xi r_{th}^2/w_0^2}. \tag{2.22}$$

Rearranging this equation to form a straight line fit gives a function independent of ξ and indicates the method introduced by Liu should still be valid. Other unknown factors beyond an intensity threshold must have to be taken into account.

The main error in the arguments presented until this point is that the model assumes any changes to the irradiated sample are because of the fluence experienced by the sample in that localized area. This assumption becomes invalid when features form due to the fluence experienced at a different location in the crater. Particularly, at higher energies, a lateral transport of material away from the center of the crater can form a rim on the edge of the crater that is not due to the local fluence. The crater would then grow at a higher rate with increasing energy because of this lateral transport. The spot size determined from D^2 measurements of this rim would be larger than the actual spot size [35]. However, this error is caused by using inappropriate pulse energies and does not explain discrepancies in spot size measurements because of the band gap of the material used to take the measurements.

CHAPTER 3

Experimental

3.1 Laser System

The sample irradiation was carried out using the femtosecond laser machining setup in the Photonics Research Lab at McMaster University. A schematic of the femtosecond laser modification setup is shown in Figure 3.1. The lower half of the figure is a schematic for the laser system used to generate and amplify ultrashort pulses. The laser system will be outlined in the following sections.

After the pulses are generated, dielectric mirrors are used to steer the pulses down the optical table through a 20/80 beam dump where only 20% of the pulse energy is retained and used for most experiments in the machining setup. A highly reflecting dielectric mirror can be used instead of the beam dump if a higher energy laser pulse is required. The beam has a diameter of approximately 10 mm at the beam dump. A telescope, consisting of a positive and negative lens, was used to reduce the beam diameter down to about 4 mm to prevent clipping on optical equipment farther along the beam line. A zero-order wave plate on a rotation mount and a thin film polarizer were then used to further attenuate the pulses. The laser pulses still have energies in the range of 40-60 μJ even after going through the beam dump. Most experiments do

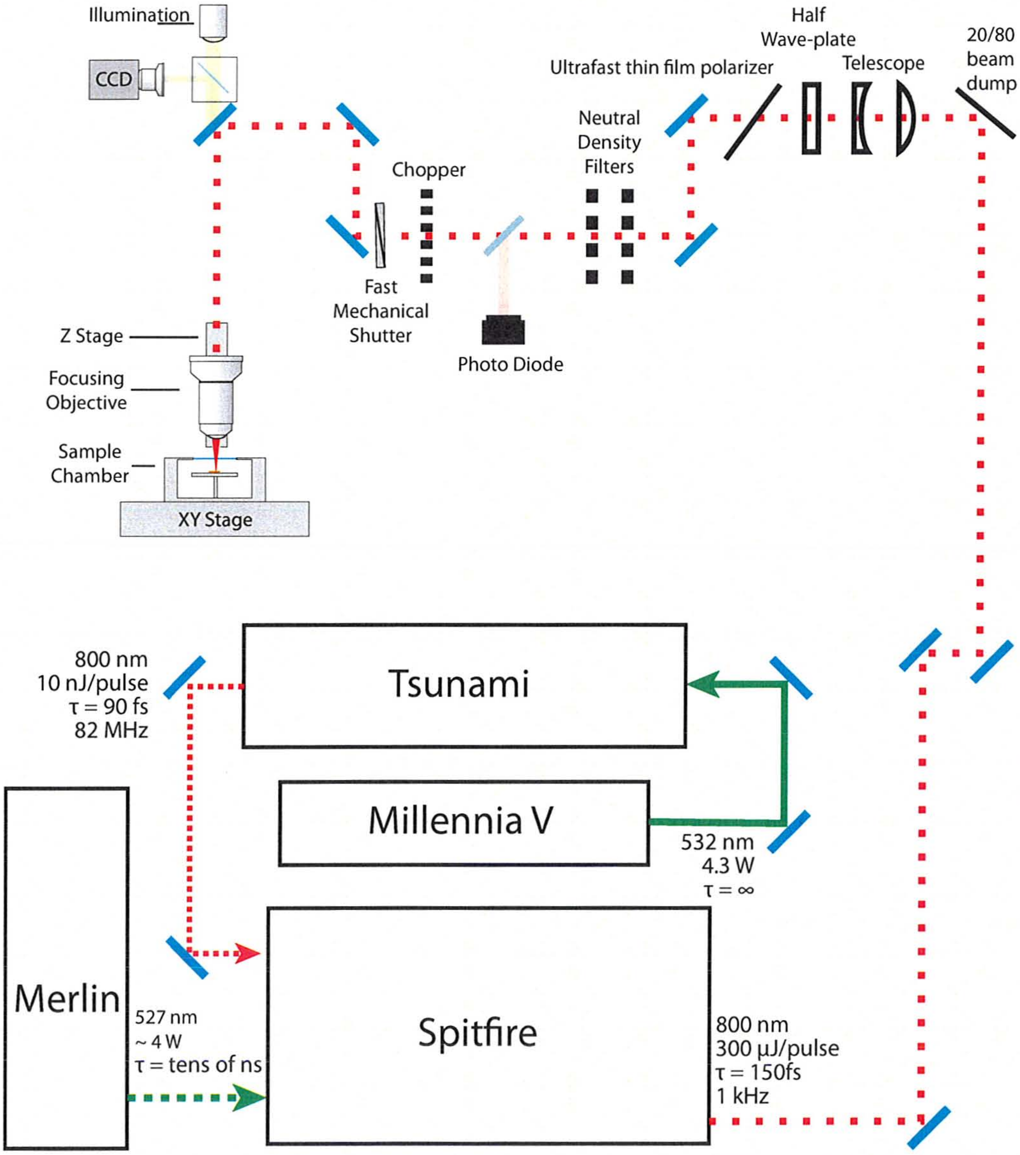

Figure 3.1: Overview of the machining setup and laser system. This is only a representation of the setup and is not drawn to scale. The xyz translation stage, shutter, and neutral density filter wheels are all controlled by software used to run the micromachining setup.

not require pulses with this much energy. Two mirrors then steered the beam through two neutral density filters. The filters were on two wheels. The first wheel had filters with optical densities (ODs) of 0, 0.5, 1, 1.5, 2, and 2.5 ($OD = -log_{10}\left(\frac{I}{I_0}\right)$). The second filter wheel had ODs of 0, 0.1, 0.2, 0.3, and 0.4. Together, these two wheels allowed for setting ODs from 0 to 2.9 in increments of 0.1. The beam then went through a chopper that could be used to reduce the repetition rate of the pulses from 1 kHz to 50 Hz. The reduced repetition rate allowed for the shutter to open, let a single pulse pass, and then close to control the exact number of pulses irradiating a sample.

The pulses were then steered by a series of mirrors and focused on a sample inside a vacuum chamber mounted on a computer controlled translation stage. The focusing was done with a long focal length microscope objective. Different microscope objectives were available to focus the laser pulses. In this thesis, a 5x microscope objective was used for experiments that involved focusing pulses on the surface of samples and a 50x microscope objective was used to focus pulses in the bulk of samples. A CCD camera was used to observe modifications to the sample during irradiation and for adjusting the focus of the laser pulses to correspond with the sample surface. The chamber was evacuated with a roughing pump for all of the experiments to a pressure of $\sim$0.05 mbar. Shielding around the chamber was used to protect users from any X-ray radiation that may be generated when irradiating a sample. Although this is more of a concern for metals, X-rays can also be produced by infrared femtosecond laser pulses irradiating low atomic number elements. A handheld radiation monitor was used to monitor radiation levels. For all experiments performed no X-rays were observed.

The sample chamber was mounted on a XY computer controlled translation stage. The microscope objective was also on a computer controlled translation stage that adjusted the vertical focus position of the pulse inside the chamber. The software that controlled the translation stage and microscope objective position also controlled the mechanical shutter and filter wheels. This centralized control allowed for automated experiments to be performed. The energy of the laser pulse and the number of laser pulses used to make each crater could be automatically adjusted to make a matrix of craters. Lines could be made by translating the sample while it was being irradiated with the chopper turned off and shutter left open. A more detailed description of the laser machining setup can be found in [36].

3.2 Short Pulse Generation

3.2.1 Tsunami Ti:Sapphire Oscillator

The femtosecond pulses were created by a Spectra Physics Tsunami Ti:Sapphire oscillator. The Tsunami is pumped by a Spectra Physics Millennia V neodymium yttrium vanadate (Nb:YVO_4) laser that is intra-cavity frequency-doubled to generate a continuous 532 nm beam of light with a power of ~4.3 W. The Tsunami generates ~7 nJ pulses with a duration of approximately 90 fs at a repetition rate of 82 MHz. This gives an average power output of approximately 900 mW. The gain medium inside the Tsunami is a titanium doped sapphire crystal (Ti:sapphire or Ti:Al_2O_3). The energy levels of the Ti^{3+} are broadened by the crystal field when placed at Al^{3+} sites in sapphire [37]. This leads to a wide absorption (400 to 600 nm) and emission band for Ti:Sapphire which makes it an excellent material for creating a broadly tunable laser [38]. The Tsunami can be tuned to wavelengths from 690 nm to 1080 nm if the right optical components are used [39]. This wide emission is important for the generation of short pulses. From the point of view of the Fourier Uncertainty Principle, the duration of a pulse is limited by the inequality

$$\Delta t \Delta \nu \geq 0.441 \tag{3.1}$$

where Δt and $\Delta \nu$ are the FWHM values for a Gaussian pulse. A 100 fs laser pulse would require a FWHM spectrum greater than 9.4 nm. Including the tails of the pulse, this requires a wide output spectrum.

Unlike a conventional laser with a linear cavity, the Tsunami has a folded cavity. A series of mirrors fold the beam back to create a long cavity but minimize the overall space required for the instrument. A longer cavity is required for pulsed lasers because

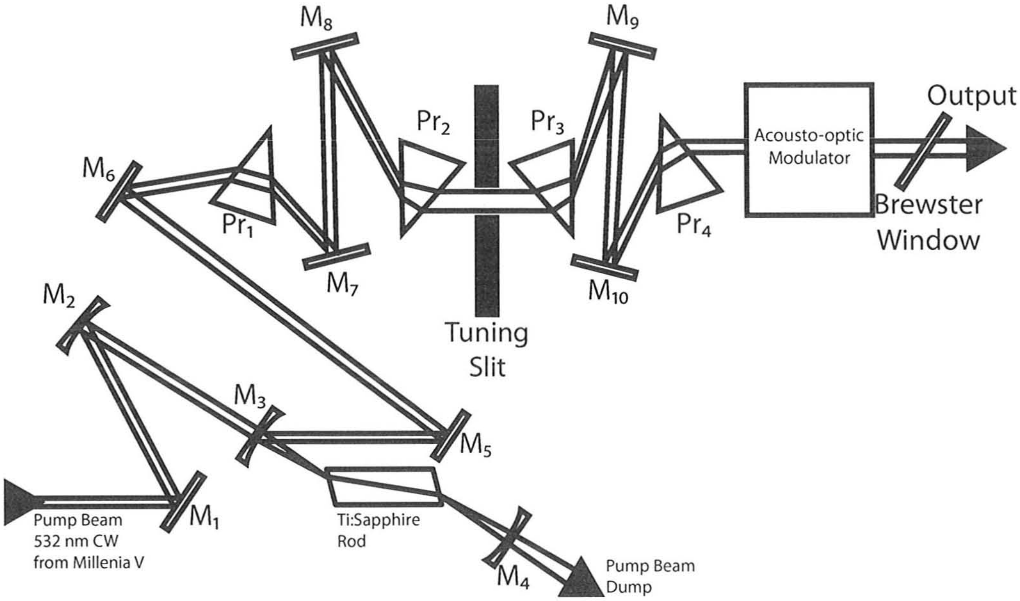

Figure 3.2: Schematic of the Tsunami Oscillator. The diagram has been simplified and excludes some components used for active mode-locking.

the repetition rate for the pulses is determined by the round trip time for a light pulse propagating in the cavity. To decrease the repetition rate to a more convenient frequency, but minimize the overall space of the instrument, a folded cavity is used.

The Millennia V must maintain a population inversion in the volume of the Tsunami's Ti:Sapphire crystal for the modes to experience a net gain. To achieve this condition, the Tsunami is pumped longitudinally as shown in Figure 3.2. Longitudinal pumping requires the pump laser beam to be collinear to modes in the Tsunami laser cavity as they pass through the gain medium. The advantage of this setup is the pump laser can be focused on the area of the Ti:Sapphire crystal where the laser beam will be traveling through the crystal. It would be very difficult to maintain a population inversion in the entire Ti:Sapphire crystal. Mirrors M_3 and M_4 are transparent to the green, 532 nm light, so that radiation from the pump laser does not pass beyond M_3. The optical components such as the prisms and the Ti:Sapphire rod were also aligned at the Brewster's angle to minimize losses due to reflections within the cavity [39].

3.2.2 Mode-Locking

Other conditions beyond simply requiring a population inversion in the gain medium and a gain medium with a wide output spectrum must be met to form ultrafast pulses inside a laser cavity. The modes that can be amplified in a laser cavity must satisfy the condition $n_I\lambda = 2L$ to undergo constructive interference. Here n_I is some integer, λ is the wavelength in air, and L is the optical path length. This condition means the output over the Ti:Sapphire emission range will be in discrete longitudinal modes given by

$$\nu = \frac{n_I c}{2L}. \tag{3.2}$$

The output from the laser will be the summation of the electric field for all these modes. Figure 3.3 shows the square of the electric field output from a laser with three modes.

In Figure 3.3a the phases are random. The output of the laser is more constant and the average intensity will remain relatively constant. Figure 3.3b shows the result for all the modes with the phases fixed so that the peaks of the sine waves add at the same point in time. The output is now more pulsed than continuous. This illustrates two operating regimes of a laser. Continuous wave lasers have one or more modes which output a constant intensity. Ultrashort pulse lasers have many modes with the phases between the different modes fixed to create short pulses. As more modes are introduced, the width of the peak in the fixed mode scenario becomes narrower and much more intense. The laser will output radiation only in the form of short, intense pulses. In a Ti:Sapphire laser the wide emission bandwidth allows for on the order of 100 000 modes which can be used to generate short pulses. A laser operating with all of its modes locked is said to be "mode-locked." Normally, each mode is competing with other modes to be amplified by stimulated emission in a laser cavity [1]. Due to this competition, the phase difference between two modes, $\phi_i(t)$ and $\phi_j(t)$, and their amplitudes fluctuate randomly in time [40].

A variety of techniques have been developed to lock or couple these modes to produce ultra-short pulses. One method is active mode locking. Active mode locking uses an external modulation, such as pumping the gain medium in the cavity with

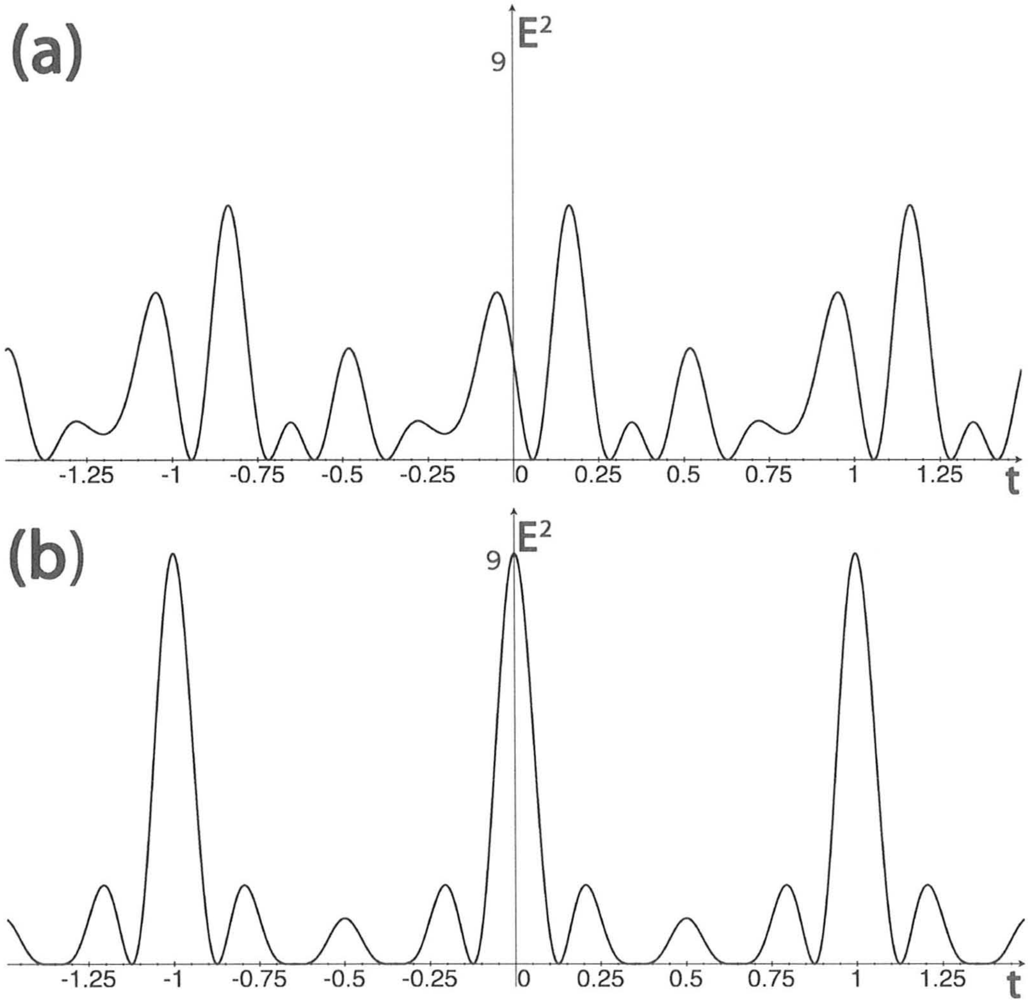

Figure 3.3: A plot of $E^2 = \left(\sum_{n=1}^{3} \cos(2n\pi t + \phi_n(t))\right)^2$ for (a) $\phi_n(t)$ random and varying randomly in time and (b) $\phi_n(t)$ fixed so that the modes add constructively at particular points in time.

another mode-locked laser, or placing an acoustic-optical crystal in the laser cavity, to fix the relative phases of each mode. An acousto-optical crystal has a permittivity which changes due to a mechanical strain on the crystal. If a mechanical strain is applied to an acousto-optical crystal in a laser cavity it will modulate the frequency of modes in the cavity. The modulation can be made close to the spacing between longitudinal modes, and the sidebands will have frequencies equal to the adjacent longitudinal modes in the frequency spectrum. These side bands and the adjacent longitudinal modes will then compete for maximum gain. This competition will lead to the phases between the side bands and the adjacent longitudinal modes locking to achieve the maximum gain. As each mode is modulated, there will be an overall coupling between all the modes. This technique is referred to as active mode-locking by amplitude modulation [1].

A laser can also be mode-locked by passive mode-locking techniques that do not require an external signal. A saturable absorber is placed in the laser cavity. Only intense light pulses which saturate the absorber will experience a net gain in the laser cavity. Because this method encourages the creation of an intense pulse which is only possible for fixed modes, the laser must be mode-locked.

Mode-locking in a Ti:Sapphire laser can be achieved by "self-locking" where the gain medium, the Ti:Sapphire crystal, invokes mode-locking [1]. This technique is used in the Tsunami. Self-locking takes advantage of the non-linear optical Kerr effect and is often called Kerr lens mode-locking. An intense electromagnetic field can produce a variation in the index of refraction [41] according to the equation

$$n = n_0 + n_2 I. \tag{3.3}$$

In this equation, the index of refraction depends on the intensity, I. A Ti:Sapphire crystal will have an index of refraction given by equation 3.3. If the pulse is considered to have a Gaussian profile given by Equation 2.12 (the time dependence can be considered part of I_0 as the beam will always have a Gaussian spatial profile at any time) then for $n_2 > 0$ this gives a change in n lateral to the direction of the pulse as shown by the plot in Figure 3.4a. In terms of the optical path length, this is equivalent to a Gaussian shaped lens. Therefore, there will be a focusing of the laser

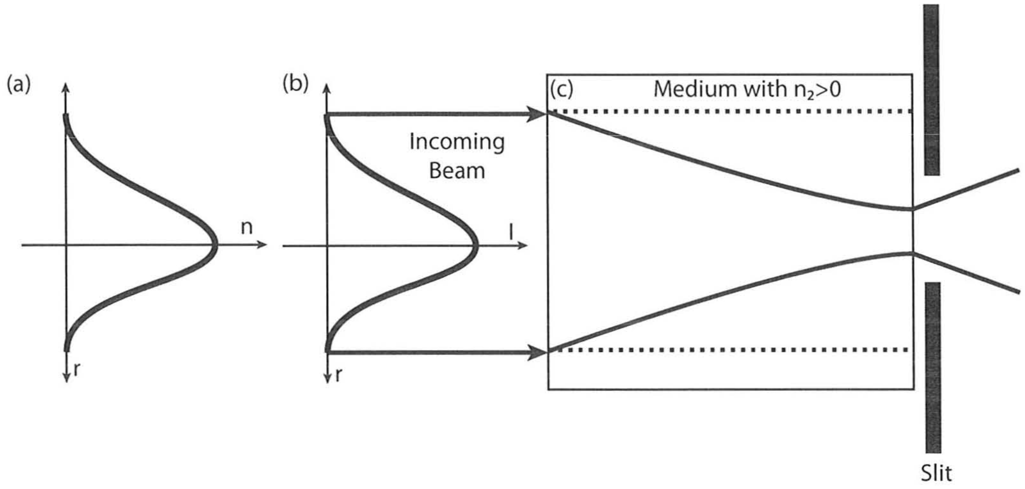

Figure 3.4: (a) the variation in refractive index, n, inside the an optical medium with $n_2 > 0$ due to a Gaussian profile beam with the intensity profile shown in (b). The Kerr lens effect will focus the beam through the slit as shown in (c). Once the laser pulse leaves the medium it will expand because of diffraction.

light towards the center of the cavity. The laser cavity is designed so that only focused light is allowed to propagate without attenuation; only intense pulses which are more strongly lensed will propagate and be amplified in the cavity. This may be done with a slit, such as the one shown in Figure 3.4c, or by simply having the cavity mirrors arranged so the cavity is only stable for these strongly focused pulses. The Tsunami operates without the requirement for a slit. Once again, the result of mode-locking by the Kerr lens effect is equivalent to fixing the overall phases between the different modes because the net result is light in the form of pulses. However, this scheme requires that there be an initial pulse in the laser cavity to start the self-locking process. The Tsunami uses an active-mode locking scheme where an acousto-optical modulator is used to start the initial mode-locking. The components required for active mode locking except for the acousto-optic modulator are missing from Figure 3.2.

3.2.3 Self-Phase-Modulation and Group Velocity Dispersion

Self-phase-modulation is caused by a time-varying index of refraction as a laser pulse passes through a medium. The nonlinear index of refraction of a material depends on the time varying intensity of a laser pulse, and therefore also varies in time. If the time dependence for the intensity of a laser pulse is given by Equation 2.12, then for a plane wave propagating through a nonlinear medium a distance, x, with a frequency, ω_0, in air, the electric field can be described by the equation

$$E(t,x) = E_0 e^{i\left(\omega_0 t - \frac{\omega_0}{c} n(t) x\right)} = E_0 e^{i(\Phi(t))}. \tag{3.4}$$

The frequency is then given by

$$\omega(t) = \frac{\partial \Phi(t)}{\partial t} = \omega_0 - \frac{\omega_0}{c}\frac{\partial n(t)}{\partial t} x = \omega_0 + \frac{\omega_0 n_2}{c} x I_0 e^{\frac{-2r^2}{w^2}} \frac{2t}{\tau^2} e^{\frac{-t^2}{\tau^2}}. \tag{3.5}$$

A plot of Equation 3.5 is shown in Figure 3.5b. A pulse with a Gaussian temporal profile (Figure 3.5a) can be thought of as a sum of plane waves. Each of these waves generates new lower frequencies at the leading edge of the pulse and new higher frequencies at the trailing edge of the pulse when traveling through a nonlinear medium with $n_2 > 0$ [1]. The overall effect will be a positively chirped pulse where the temporally leading part of the pulse is made up of longer wavelengths (lower frequencies) than the trailing part of the pulse. The net effect can be seen in the frequency spectrum shown in Figure 3.5c. The initially Gaussian frequency spectrum has developed minima and maximum due to interference between the new frequencies which were generated. As shown in Figure 3.5b, at times t_1 and t_2 the same frequency is being generated. Pairs of frequencies are generated at all other time delays as well. These pairs interfere constructively and destructively to create the overall minima and maximum seen in Figure 3.5c.

The pulse is also being spread by the optical components in the laser cavity. These components have a positive group velocity dispersion (GVD) where longer wavelengths travel faster through the cavity. This effect also produces a positively chirped pulse [39]. To compensate for this positive GVD from the optical components

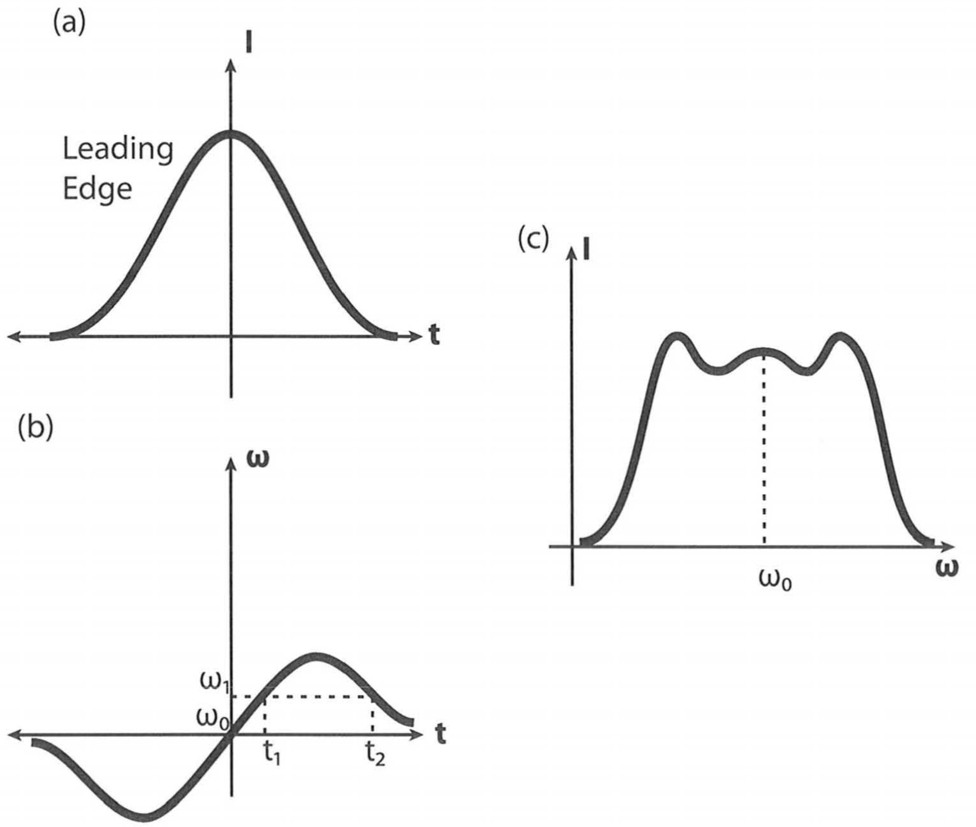

Figure 3.5: (a) a Gaussian profile beam showing the intensity versus time. (b) the new frequencies created as a function of time due to self-phase-modulation of a plane wave of frequency ω_0 (plot of Equation 3.5). (c) the intensity profile of an initially Gaussian pulse due to self-phase-modulation.

and self-pahse-modulation, pairs of prisms as shown in Figure 3.2 are used to produce a net negative GVD. The prisms force the longer wavelength light to go through a longer path in the cavity.

3.2.4 Wavelength Selection

The prism pairs shown in Figure 3.2, besides compensating for a positive GVD, are also used to select the central wavelength of the pulses generated by the Tsunami. The prism pairs split the different wavelengths lateral to the cavity and using a slit the wavelengths allowed to travel through the cavity can be selected. This slit can be moved to tune the laser to different wavelengths. Although a Ti:Sapphire crystal can be made to lase from 690 nm to 1080 nm, other factors, such as the reflectivity of the mirrors that varies with wavelength, makes it impossible to tune the Tsumami over this entire range. Different mirrors can be used for different ranges. The standard mirrors used in the Tsunami allow for tuning from 720 – 850 nm. The Tsunami was tuned to output pulses with a central wavelength of 800 nm and a bandwidth, measured as the full width half maximum (FWHM), of 10 nm for all the experiments performed in this thesis.

3.3 Pulse Amplification

3.3.1 The Spitfire LCX Ti:Sapphire Chirped Pulse Amplifier

The pulses from the Tsunami seed the Spectra Physics Spitfire LCX Ti:Sapphire chirped pulse amplifier. This is a regenerative chirped pulse amplifier where the pulse undergoes a group velocity dispersion to first stretch the pulse before it is amplified and compressed. Amplifying a short pulse would create too high of an intensity in the laser cavity and damage the Ti:Sapphire crystal [42]. A high intensity pulse would also be subject to self-focusing by the Kerr lens effect which would further intensify the pulse in a Ti:Sapphire crystal. Keeping the intensity below 10 GW/cm^2

should minimize this effect. The chirped pulse amplification (CPA) process overcomes this problem by first stretching the pulse to reduce the intensity while it is being amplified and then compressing the pulse after it leaves the laser cavity and can no longer damage the gain medium. This technique was developed in the 1980s [43] and has become the standard method for amplifying femtosecond laser pulses. It is only possible because laser pulses are made up of a range of wavelengths.

3.3.2 Pulse Stretching and Compression

A pulse stretcher consists of one or more gratings which cause light to be deflected at different angles depending on the wavelength. Depending on the geometry, higher frequency light can be made to travel a longer path than lower frequency, redder, light using a series of mirrors and lenses. This kind of stretcher is said to have a positive GVD and the resulting pulse is positively chirped. The opposite configuration, where the higher frequency light travels a shorter path, has a negative GVD and produces a negatively chirped pulse. The Spitfire uses a stretcher with a positive GVD that produces a positively chirped pulse. A compressor with a negative GVD is then used to compress the amplified the pulse [44]. A schematic of the pulse as it goes through the amplification process is shown in Figure 3.6. A schematic of the actual pulse stretcher and compressor can be found in the Spitfire user manual [44].

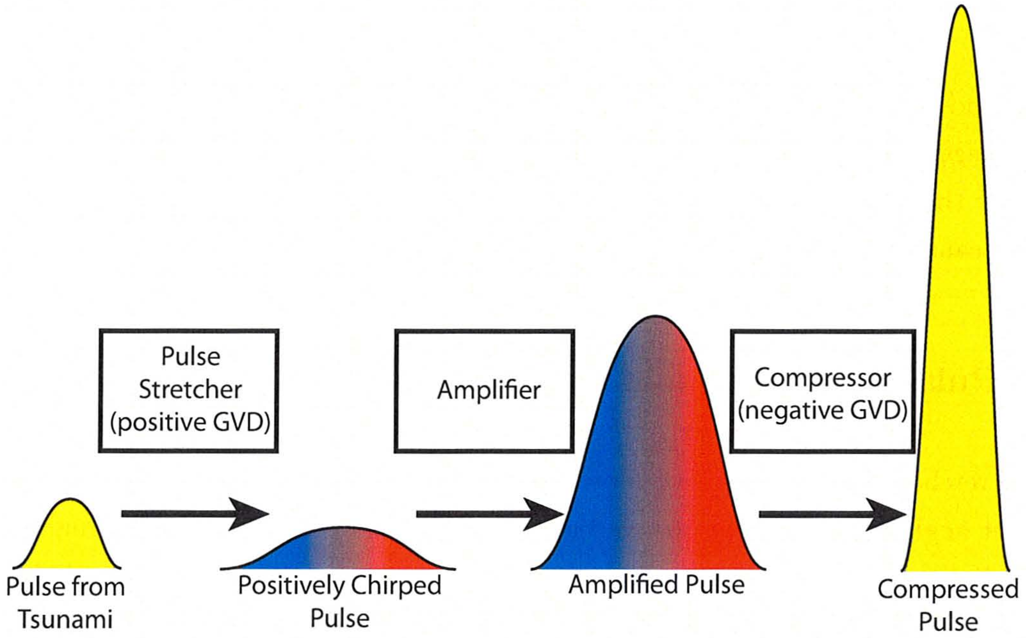

Figure 3.6: Symbolic representation of a pulse undergoing amplification in the Spitfire regenerative amplifier.

3.3.3 Regenerative Pulse Amplification

The Spectra Physics Spitfire regenerative pulse amplifier uses a Ti:Sapphire rod as the gain medium that is pumped by a Spectra Physics Merlin LCX Nd:YLF (or Nd:LiYF$_4$). The Merlin is a Q-switched laser that is intra-cavity frequency doubled to generate 527 nm pulses at a repetition rate of 1 kHz with an average output power of 3-4 W. Figure 3.7 shows a schematic of the Spitfire cavity where pulse amplification occurs. A stretched seed pulse from the Tsunami is incident on the left face of the Ti:Sapphire crystal. If both Pockels cells are off, a pulse enters the cavity, is reflected off the left hand mirror, right hand mirror, and back off the left hand mirror. It has gone through the quarter-wave plate a total of four times at this point as it is incident on the left surface of the Ti:Sapphire rod. It will have a vertical polarization and it will be reflected from the cavity at the same place it entered. A pulse can be trapped in the cavity if the following sequence of events occur. A pulse enters the cavity, is reflected off of the left hand mirror, and goes back through the input Pockels cell which is still shut off. It is then horizontally polarized and goes through the Ti:Sapphire

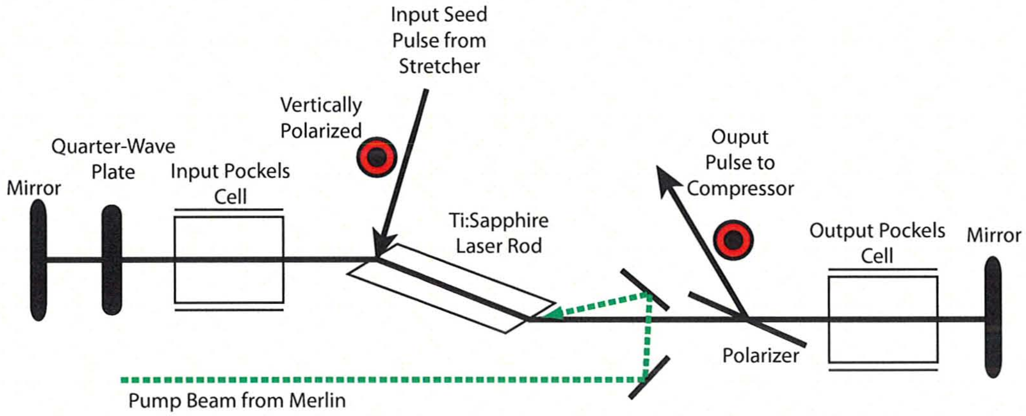

Figure 3.7: Schematic of the Spitfire cavity where regenerative amplification occurs (vertical direction into the page). The Pockels cells can either be off, and not change the polarization of pulses which pass through the cells, or on and act as quarter wave plates. The Ti:Sapphire rod and polarizer are set at the Brewster's angle and will entirely transmit a pulse that is incident on the surface with a horizontal polarization and reflect most of a pulse that is incident on the surface with a vertical polarization.

crystal and is reflected back off the left hand mirror. If the input Pockels cell is turned on before the pulse has returned to the input Pockels cell, it will trap the pulse. The input Pockels cell acts as a quarter-wave plate when turned on. This causes pulse incident from the left on the Ti:Sapphire crystal to be horizontally polarized. Because the rod is set at Brewster's angle, the pulse will be entirely transmitted instead of mostly reflected back toward the input direction which occurred when both Pockels cells were off. As long as the input Pockels cell remains on and the output Pockels cell is off, the pulse will remained trapped in the cavity. New input pulses which enter the cavity while the input Pockels cell is on will go through the input Pockels cell in the on position, through the quarter wave plate, reflect off of the left hand mirror, go back through the quarter wave plate and Pockels cell, and be incident on the left side of the Ti:Sapphire rod in the same vertically polarized state at which they entered. The pulse will then be mostly reflected back in the input direction.

The pulse that is trapped within the regenerative amplifier cavity will pass back and forth through the Ti:Sapphire crystal which has been pumped by the Merlin. Each pass provides a gain of ~3 to the seed pulse [44]. For pulses to be amplified from approximately 10 nJ to 300 μJ, requires many passes through the Ti:Sapphire crystal. A pulse is eventually ejected from the cavity by turning on the output Pockels cell. The pulse then travels from the left through the output Pockels cell, reflects off the mirror, goes back through the Pockels cell, and is incident on the polarizer. The pulse is now vertically polarized after going through the output Pockels cell twice. The pulse is mostly reflected by the polarizer because it is not at the right polarization to be transmitted. The amplified pulse is then compressed to approximately 150 fs.

The regenerative amplifier produces pulses at a repetition rate of 1 kHz and dumps most of the pulses created by the Tsunami which produces pulses at a repetition rate of 82 MHz. The repetition rate of the Spitfire is determined by the Merlin pump laser. The Merlin pumps the Ti:Sapphire rod in the Spitfire with a single pulse. A seed pulse from the Tsunami enters the regenerative amplifier cavity and makes multiple passes through the Ti:Sapphire rod until the rod no longer has a population inversion and the pulse is ejected as it will no longer be amplified. The Ti:Sapphire rod is then pumped again by another pulse from the Merlin and the process repeats. The Pockels cells must be switched on and off at very precise times for the sequence of events described above to occur. The Spitfire uses fast electronics and is synchronized with the Tsunami and Merlin pump laser to achieve the correct timing.

3.4 Pulse Diagnostics

3.4.1 Measuring the Pulse Duration

The duration of femtosecond laser pulses cannot be directly measured using a photodiode because the response time of photodiodes is much longer than the pulse. Therefore, the pulse duration is measured by a more indirect method using an optical non-collinear second order autocorrelator. The setup for this device is similar to a Michelson interferometer where the incident laser pulse goes through a beam splitter and is separated into two pulses that travel along different paths. One travels collinear to the original pulse and the other travels at a 90° angle to the original pulse. The pulses are then reflected back to the beam splitter by mirrors. The mirror for one path is fixed while the mirror for the other path is on a translation stage used to create an optical delay. The pulses then go back through the beam splitter and travel collinear to each other at a ninety degree angle to the original pulse. These collinear pulses go through a lens and are focused to the same point in a frequency doubling crystal. The output from the crystal is a frequency doubled pulse [45]. The intensity of the frequency doubled pulse will be related to the overlap between the two original pulses because the rate of second harmonic generation inside a frequency doubling crystal is highly dependent on the intensity. By varying the delay between pulses (moving the mirror) and measuring the output intensity as a function of this delay, the second order autocorrelation function can be measured. The temporal width of this function can be used to determine the temporal width of the actual pulse if the original pulse shape is known. The standard used in the scientific community is to assume the pulse has an inverse hyperbolic secant profile when calculating the temporal width from the second order autocorrelation function [1].

GRating-Eliminated No-nonsense Observation of Ultrafast Incident Laser Light, or GRENOUILLE technique can also be used to make sure the pulses are not chirped and have a minimal pulse-front tilt. This is done periodically to ensure the laser system produces pulses with a low pulse-front tilt and minmal chirp.

3.4.2 Satellite Pulses

The femtosecond laser system creates pre-pulses and post-pulses from the regenerative amplifier and neutral density filters. Post pulses with substantially less energy delayed relative to the main pulse on the picosecond scale (~10 ps) are produced by the neutral density filters because of reflections off the surface of the filters. Pre-pulses and post-pulses are also produced by the Spitfire in multiples of ~7 ns before and after the main pulse. The transmission and reflection of pulses in the Spitfire relies on the polarization of the pulses and optical elements set at the Brewster's angle to discriminate between different pulses that are either ejected or trapped and amplified in the Spitfire cavity. However, at the Brewster's angle, referring to the orientations in Figure 3.7, vertically polarized pulses inside the Spitfire cavity will not be completely reflected by the Ti:Sapphire crystal interface and there will be some transmission. Pulses that are supposed to be completely ejected at the Ti:Sapphire interface when the input Pockels cell is on will be slightly transmitted and output at the polarizer interface. Post pulses are also produced because when the output Pockels cell is turned on not all of the light from the pulse will be ejected by the polarizer. Some will remain in the laser cavity and make another round trip through the cavity before being ejected as a post-pulse. The post-pulse traveling through the cavity will be vertically polarized, and will be highly attenuated with each round trip. The response time of the Pockels cells also causes pre- and post-pulses. Pockels cells have a characteristic response time to turn on and off. During this time the Pockels cells will alter the polarization of the pulses differently from a quarter wave plate. Therefore, the satellite pulses adjacent to the main pulse will be the strongest because the output Pockels cells is turning on and off to eject the main pulse from the Spitfire cavity. Measurements of the pre-pulse adjacent to the main pulse using a fast photodiode showed the peak intensity of these pulses was $\sim$0.1% of the main pulse.

One way to eliminate these pulses would be to use a frequency doubling crystal to modify materials with 400 nm light. As the generation of 400 nm light depends nonlinearly on the intensity, the low intensity, 800 nm satellite pulses would produce very little 400 nm satellite pulses. The post pulse from the neutral density filter could be removed by using a computer controlled wave plate to attenuate the signal instead of the filter wheel. Adding a Pockels cell with the right timing to the Spitfire could remove most of the energy in the nanosecond pre-pulses and post-pulses.

3.5 Microscopy

3.5.1 Transmission Electron Microscopy

One of the main challenges of using transmission electron microscopy to study materials modified by femtosecond laser pulses has been the ability to make TEM samples. Conventional mechanical methods for TEM sample preparation generally require a large sample area (at least 500 μm wide) to make a thin TEM foil. The areas modified by the laser are generally only a few microns in diameter. It would be impossible using conventional polishing techniques to select only the modified area of the sample to make a TEM specimen. Extra challenges arise in the case of diamond because of its extreme hardness. Conventional sample preparation equipment cannot polish such a hard material. Instead, samples were made using a Zeiss NVision 40 focused ion beam machine (FIB) and SEM. The FIB allows for precise selection of the area where a TEM slice will be made. First, an electron beam is used to deposit a protective amorphous platinum layer over the area used to make a TEM specimen by ion-beam assisted chemical vapour deposition. Ga ions were then used to deposit more platinum. Electrons were initially used to reduce the possibility of surface damage. However, the Ga ions are more efficient at ion-beam assisted chemical vapour depostion and were used after the electrons produced a small platinum surface layer. After depositing platinum, a thicker layer of carbon was also deposited. Material was milled away from around the area of interest using a focused ion beam of Ga ions to create a thin membrane. The *in situ* lift-out technique was used to mount the specimen to a TEM grid. The membrane was then further thinned until it was electron transparent [46, 47]. An overview of the sample preparation process is shown in Figure 3.8.

A TEM was used to analyze changes in the diamond crystal structure after irradiation with femtosecond laser pulses. Bright field images which form an image from only the non-diffracted electrons by placing a small aperture on the optical axis at the the back focal plane of the objective lens were used to observe changes in the crystal structure on the nanometer scale. The contrast in these images is a result of changes in the amount of electrons which are diffracted from a particular area. There will be a contrast between different grains because the number of diffracted electrons depends on the orientation of the different grains with respect to the incident electron beam. These images can be used to determine areas which are single crystal, polycrystalline or amorphous. The size of larger grains can also be estimated depending on the size of the grains and the sample quality. Dark field images that use the diffracted electrons to form an image can also be taken. These images generally show more contrast between the different grains. However, dark field images generally require very thin

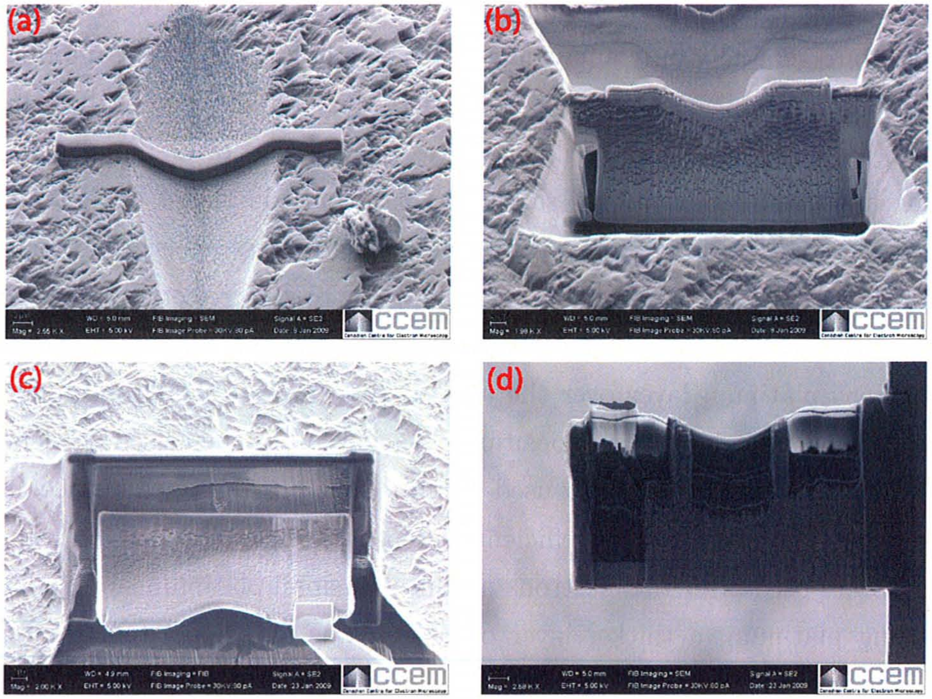

Figure 3.8: Overview of the *in situ* lift out technique. (a) the area of interest was coated in a protective layer of platinum and carbon to protect the surface from damage. (b) a thin membrane was made by milling away material. (c) the membrane was glued to a manipulator and cut free of the main sample. (d) the membrane was attached to a TEM grid and the area close to the surface was thinned until it was electron transparent.

samples to form an image which has enough brightness.

Selected area electron diffraction patterns were also taken to determine the crystal structure. These patterns are formed at the back focal plane of the objective aperture and projected onto the screen. An aperture is placed at the image plane of the objective lens. This is called a virtual aperture. It is equivalent to placing an aperture in the specimen plane which only allows electrons to pass through the sample in this small area. Because this is not physically possible, the aperture is placed at the image plane. Therefore, the diffraction pattern is only formed from electrons that pass through the sample in the area chosen by the aperture.

3.5.2 Optical Microscopy

Images of the diamond surface were taken with an optical microscope using the differential interference contact (DIC) or Nomarski technique. This technique enhances the contrast in transparent samples. It works on the principle of interferometry where the light beam is split into two polarized rays which are given a slight lateral offset, focused on the sample surface at adjacent locations, and then recombined to form an image. The image will show contrast due to the interference between the two beams which have traveled slightly different paths lengths depending on the topography of the sample. The interface between two materials with different optical densities will also create contrast in a DIC image. Materials with different optical densities will have different reflectivity coefficients. One beam may therefore be more highly reflected than the other beam which was incident on the opposite side of the interface.

3.5.3 Atomic Force Microscopy

An atomic force microscope (AFM) was used to measure the absolute heights of the diamond surface post irradiation. The microscope was used in tapping mode where the cantilever operates with a constant oscillation amplitude and lightly taps the surface while scanning. It can maintain a constant height above the surface because the vibration frequency changes as more force is applied to the cantilever as it approached the surface. Contact mode, where the cantilever is dragged along the surface and a constant deflection is maintained, was not used because the silicon cantilever tips were easily destroyed by the hard diamond surface. Cantilevers that were also made of diamond may have made it possible to use contact mode.

3.5.4 Scanning Electron Microscopy

SEM images were taken using a JEOL 7000 SEM and the SEM in a Zeiss NVision 40. Diamond was a difficult material to image in the SEM because it is prone to charging. The SEM was operated at 2 kV with a low beam current to reduce charging. This charging was also an issue when using a FIB to make TEM samples. The ions would be deflected from the area they were supposed to be focused because of charging. If the charging could not be controlled the sample was coated in a thin layer of platinum ($\sim$1 nm) to reduce charging.

CHAPTER 4

Results and Discussion

4.1 Overview

This chapter presents the results of an analysis of the structures formed on the surface and in the bulk of laser-irradiated diamond. The laser setup described in Chapter 3 was used to focus femtosecond laser pulses both on the surface and in the bulk of CVD grown diamond.

Diamond is an excellent material for researching the modifications from irradiation with femtosecond laser pulses. As previously described, high spatial resolution machining with a laser can only be obtained when the energy is deposited in a short time scale to avoid a large heat affected zone. The high thermal conductivity of diamond makes it very susceptible to this kind of damage [50]. Advances in growth techniques for synthetic diamond are also making diamond a more affordable material for use in a variety of applications such as in deep ultraviolet lasers and photodetectors, high power semiconductor devices, and field emitting displays. These technologies could all benefit from new techniques for high resolution micro-patterning and machining of diamond.

4.2 Diamond Sample Specifications

Diamonds are generally grouped into four different categories or types based mainly on variations in color caused by impurity levels and defects in the crystal structure. Type Ia is the most common type of diamond found in nature and contains up of 0.3 % nitrogen. Type Ib is a much rarer form. It contains nitrogen at levels up to ~500 ppm. Both types of diamond appear yellow or brown because they absorb blue light. Even rarer forms of diamond found in nature are type II diamonds. These types of diamond contain much less nitrogen. Type IIa can be colorless and are often referred to as optical grade diamond. They can also be red or brown because of defects in the crystal structure which cause absorption in the visible range [48]. Type IIb are generally blue and contain a large concentration of boron. Some type IIb diamonds are p-type semiconductors because of high boron concentration.

The lack of impurities in type IIa diamond gives it superior optical and thermal properties compared to other forms of diamond. Type IIa diamond at room temperature has a thermal conductivity of ~2600 W/m·K or about six times the thermal conductivity of copper. However, type Ia has a thermal conductivity that is only two times greater than copper [49]. Other physical properties of type IIa diamond include a heat capacity of ~2000 J/kg·K and a sublimation temperature of approximately 4000 K [49].

The optical properties of diamond include a refractive index of 2.397 at 800 nm and an absorption edge of 235 nm [51]. Therefore, diamond, like other dielectrics, will only absorb infrared pulses through multi-photon processes. Four photons at 800 nm (1.55 eV) are required to excite an electron across the band gap of diamond (5.5 eV). It is only because of the high intensity of femtosecond laser pulses that absorption through multi-photon and avalanche processes can occur.

All of the diamond samples used for experiments in this thesis were grown, cut, and polished by Element Six Inc. into 3×3 mm squares with a thickness of 0.5 mm. These samples were single crystal, and all were grown and cut to have {001} type faces. The growth specifications given by Element Six included impurity concentrations that were less than 1 ppm for nitrogen and less than 0.05 ppm for boron measured in terms of mass. These samples could be classified as type IIa diamond due to the low impurity levels. The samples were colorless and transparent. Some of the samples had a top and bottom both polished to have an overall average surface roughness (Ra value) of less than 10 nm while some samples had only one side polished. Any surface experiments were performed on samples which had only one side polished because there was no benefit to having both sides polished. Bulk experiments were performed on samples which had both sides polished because any modifications in the bulk could be more easily seen with the optical microscope using transmitted light. The edges of the diamond squares were cut with a laser and then polished to have a Ra < 250 nm by Element Six Inc.

The quality of the diamond samples was less than ideal. Figure 4.4 shows an overview of one of the samples post irradiation. The unmodified areas (such as the top right area of the sample) were covered in small pits. Using an atomic force microscope (AFM) it was found that the pits were on the order of $10 - 20$ nm deep. The effects of these surface features could not be noticed at some of the higher pulse energies. However, it will be shown using lower pulse energies that these defects appear to help in the production of LIPSS.

4.3 Determination of the Spot Size and Damage Threshold

Accurately measuring the spot size of the laser pulses is important to obtain correct values for the fluence. The spot size was determined using the method described in Section 2.4 which is based on the approach of Liu [32]. The spot size was measured using both the CVD single crystal diamond plates and silicon to determine if the spot size measurements were affected by the band gap of material used to make the measurements as described by Bonse *et al.* [34]. The diameter of the single pulse craters versus the natural logarithm of the energy was plotted to give a straight line fit according to Equation 2.18 for silicon and diamond. The results for the 5x microscope objective are shown in Figures 4.1 and 4.2.

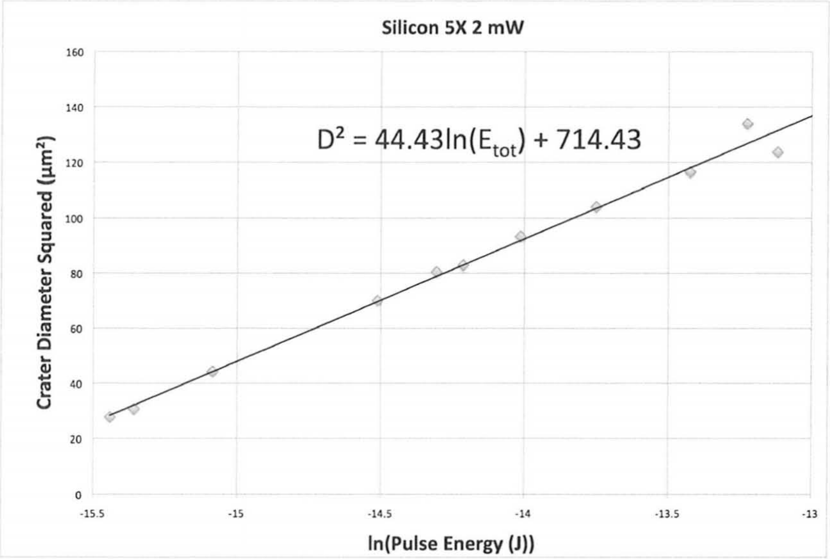

Figure 4.1: D-squared measurements on silicon using the 5x microscope objective and a peak power of 40 mW. The slope gives a $1/e^2$ spot size, $w_0 = 4.7$ μm.

The plot for silicon in Figure 4.1 gave a straight line fit over all of the energy values used. The higher energy values used for diamond are marked in red in Figure 4.2, and were not included in the straight line fit. At these high energy values, material from the crater was ejected out in the lateral direction and features on the edge of the rim were no longer due to the localized fluence. This lateral movement of material makes the diameter of the crater increase at a faster than would otherwise occur if the features on the edge of the crater were only due to the local fluence. The spot size measured on silicon was 4.7 μm and was higher than the 4.0 μm spot size measured using diamond. These results are in agreement with Bonse *et al.*, who found the spot size measured on higher band gap materials ($E_g = 5.5$ eV for diamond) was less than the value measured using lower band gap materials ($E_g = 1.1$ eV for silicon) which undergo linear absorption of 800 nm light. Repeated measurements of the spot size using the 5x microscope objective on different experiment days also gave a spot size of $4.6 - 4.7$ μm when using silicon and lower values when using diamond. These measurements were done using images taken on the optical microscope in Nomarski mode. Similar results were obtained when using images taken on the SEM.

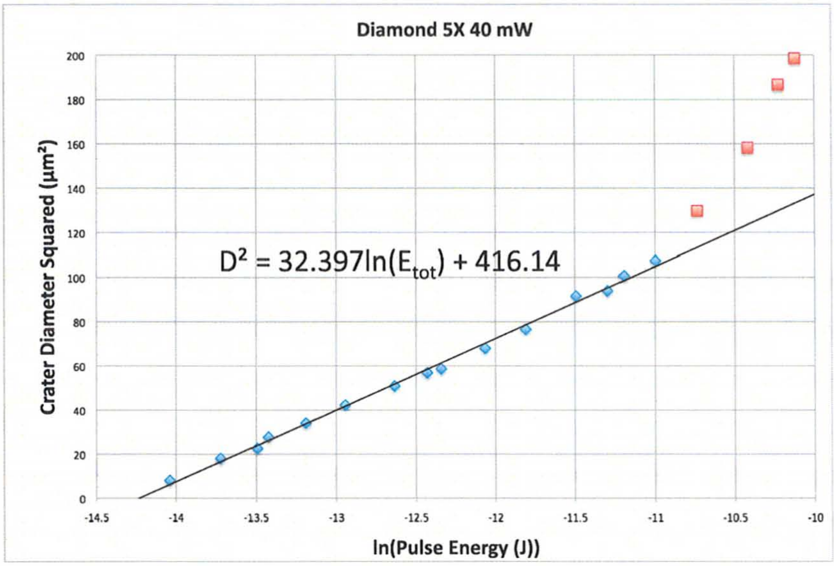

Figure 4.2: D-squared measurements on diamond using the 5x microscope objective and a peak power of 2 mW. The slope gives a $1/e^2$ spot size, $w_0 = 4.0$ μm. The red data points were not included in the regression.

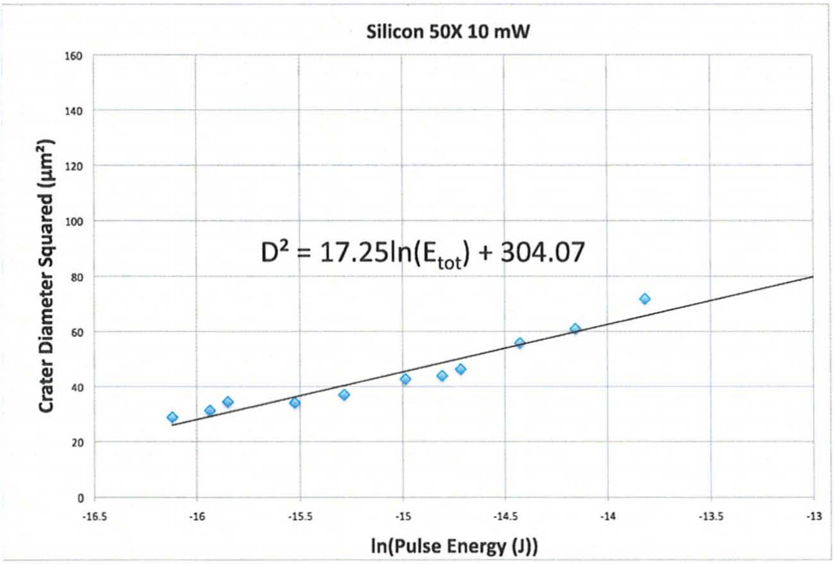

Figure 4.3: D-squared measurements on silicon using the 50x microscope objective and a peak power of 10 mW. The slope gives a $1/e^2$ spot size, $w_0 = 2.9$ μm.

Measurements of the laser pulse spot size when using the 50x microscope objective to irradiate silicon are shown in Figure 4.3. The beam energy was initially set to 10 mW; however, only the lower energy pulses were used for reasons described above. The measured spot size for the 50x microscope objective was 2.9 μm. The fluence values reported for different experiments throughout this thesis used the spot sizes measured from silicon. One concern, especially with the 50x microscope objective which has a much smaller Rayleigh range than the 5x microscope objective, is that the spot size will change as the sample surface is moved away from the plane of focus. Although focusing is done carefully, the pulses may not always be focused on the sample surface. This would also introduce an error in spot size measurements and the fluence values for samples irradiated with the sample surface not directly in the plane of focus would be be overestimated.

The straight line fit used in the D-squared method to calculate the spot size can also be used to determine a threshold fluence for modification of a material. This value can be determined from the intercept of the straight line fit (equation 2.18). The damage threshold fluence or the ablation threshold fluence can be measured depending on which feature is tracked in the craters to make the diameter measurements [52]. It can be quite difficult to accurately measure and track either an ablation feature or a modification feature for a series of craters. The intercept of the graph in Figure 4.2 gave a threshold for diamond of 1.9 J/cm^2. This value is close to the ablation threshold value of 1.6 J/cm^2 measured by Dumitru *et al.* using 800 nm, 150 fs pulses [52]. This measurement was made using the same intercept method. Dumitru *et al.* also measured a damage threshold fluence of 0.4 J/cm^2 by tracking an outer edge feature in single pulse diamond craters [52]. The diameter measurements in this thesis were taken using the rim of the crater. The measured threshold was then expected to give a value more closely related to the ablation threshold fluence. Ramanathan *et al.* [49] measured a damage threshold fluence for diamond of 4 J/cm^2 using 775 nm, 200 fs laser pulses. This discrepancy could be caused by differences in the pulse parameters. Any change in pulse duration and intensity could play an important role in dielectrics because the laser intensity is strongly related to the rate of absorption. Also, the D-squared method of measuring threshold fluences may not be very accurate because as described above, it is difficult to track ablation features. There may also be changes in the damage threshold due to the quality of the diamond surface. The role played by cracks and pores is believed to be important in the breakdown of materials by lasers. Bloembergen [8] believed submicroscopic surface structures accounted for the lowering of the breakdown intensity by a factor of 4 to 5 on the surface as compared to the bulk in materials such as glass and sapphire. He showed the accumulation of surface charge in cracks and pores could enhance the electric field in those areas and cause an apparent decrease in the damage threshold of transparent dielectrics [53].

4.4 Surface Experiments on Diamond

4.4.1 Overview

Surface modification of single crystal diamond was one of the two main areas of study. The main goal of this work was to characterize the LIPSS and other structures made on the surface of diamond. Single and multiple pulse craters were made as well as surface lines for a range of pulse energies. Although some work has been done on studying LIPSS formed on diamond, not much work has been done on LIPSS formed on single crystal diamond by femtosecond laser pulses. Also, most of this work has only involved studying the surface using scanning electron microscopes (SEMs) or optical microscopy. The facilities provided by the Canadian Centre for Electron Microscopy (CCEM) allow for studying changes to the subsurface using a FIB to make TEM samples.

4.4.2 Experimental Setup

Figure 4.4 shows an optical microscope image of a typical surface experiment on one of the diamond plates. All of the surface experiments were performed in vacuum at $\sim$0.05 mbar and used 800 nm laser pulses that had a duration of $150 - 200$ fs. The 5x microscope objective was used in all the surface experiments to focus the laser light on the surface of the samples. The laser pulses were always incident perpendicular to the sample surface. The spot size was measured on silicon once each day experiments were performed.

Single and multiple pulse craters were made at variety of pulse energies. A matrix of craters was automatically made using the software which controls the femtosecond laser machining setup. Lines were also made at a variety of pulse energies. To make the lines the sample was translated at 500 μm/s with the shutter fully open and chopper turned off to allow for pulses to irradiate the sample at a repetition rate of 1 kHz. The laser polarization was kept perpendicular to the scan direction because the ripples formed perpendicular to the direction of the polarization. The ripples then formed with lines along the crests of the ripples parallel to the direction of the line. TEM cross-sections could then be made across the line and the sections showed the profile of the crests and valleys of the ripples. The craters and lines were each made in groups of five to keep track of their positions when viewed in the microscopes.

4.4.3 Initial Observations

One of the first observations made when ablating diamond was the formation of a black layer around areas that were modified with a higher fluence. This layer appears to be black graphite which formed during the irradiation and was ejected away from the area the laser pulses were focused. For craters formed with 10 repeated pulses or less, the formation of a surrounding graphite layer is not noticeable with the optical microscope probably because the layer is too thin. Much of the carbon which was ablated may also have formed CO_2 or CO by reacting with the oxygen in the chamber.

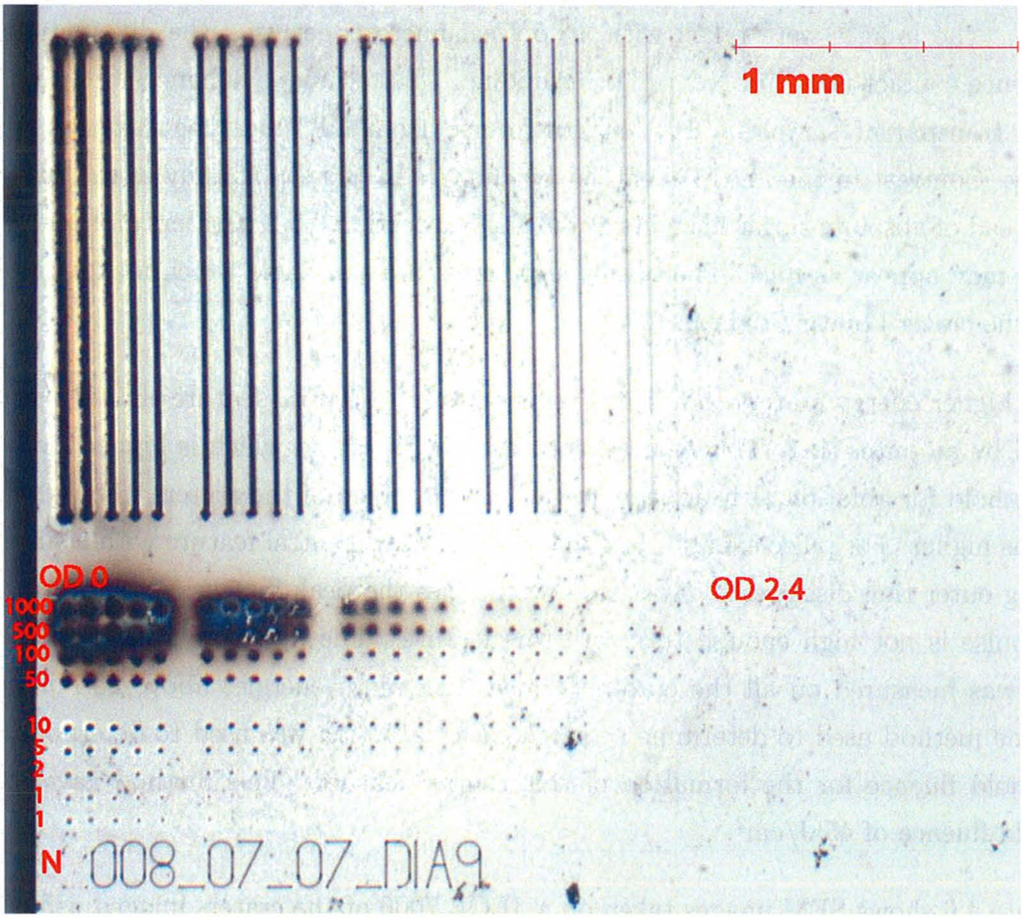

Figure 4.4: Optical microscope image of a typical surface experiment performed using ~160 fs laser, 800 nm pulses with a peak power of 40.2 mJ/pulse. The lines at the top of the image were made by moving the sample at 500 μm/s with optical density filter wheel settings from 0 to 2.4. The pulses irradiated the sample at a repetition rate of 1 kHz. The craters below the sample range from single pulse to 1000 pulses per crater (N denotes the number of pulses) at energy levels denoted by OD values from 0 to 2.4.

4.4.4 Single Pulse Craters

Figure 4.5 shows a series of images of single pulse craters made with different pulse energies. The images were taken with an optical microscope using the differential interference contact (DIC) or Nomarski technique. This technique enhances the contrast in transparent samples. The images formed from DIC must be interpreted carefully. Contrast in the image is caused by changes in the topography of the surface instead of absolute surface heights as outlined in Section 3.5.2. Craters and other features may appear as hills. The beams also come in at an angle which makes one side of the crater appear brighter.

The higher energy craters shown in Figure 4.5 have a central feature that is surrounded by an outer ring. This central feature has a threshold which is higher than the threshold for ablation as it appears in the central region of the craters where the fluence is higher. For pulse energies less than 16.7 μJ, this central feature with a surrounding outer ring disappears. At these low energies the peak fluence at the center of the pulse is not high enough to create this feature. The diameter of this inner feature was measured on all the craters formed with pulse energies above 16.7 μJ. The same method used to determine a threshold for ablation was used to determine a threshold fluence for the formation of this central feature. This method gave a threshold fluence of 45 J/cm^2.

Figure 4.6 shows SEM images taken on a JEOL 7000 of the craters imaged using an optical microscope in Figure 4.5. Imaging diamond in a SEM is difficult and required using low accelerating voltages (below 2 kV) to reduce charging. The higher energy pulses show a very rough outer ring compared to the inner region. These small rough features cannot be seen in the optical microscope images. The central area appears to be quite smooth compared to the outer region for pulse energies above 29.9 μJ. At pulse energies below 21.8 μJ this central feature with an outer ring disappears. A new feature can be seen in the center of the craters made with energies below 21.8 μJ. However, it is not surrounded by an outer ring and appears to be more from splattering of molten material from the center of the crater. This feature disappears when the peak fluence of the laser pulse used to make the crater

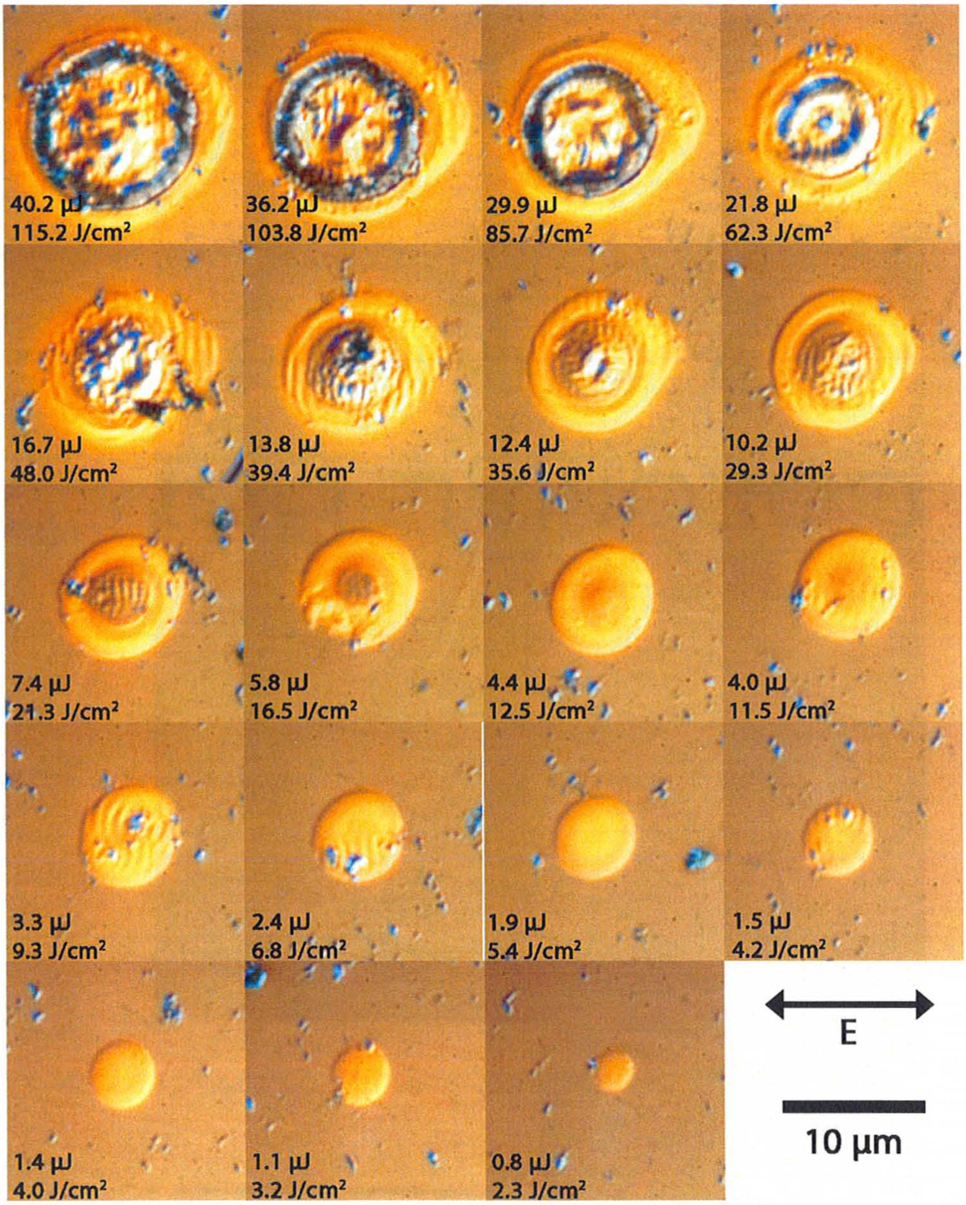

Figure 4.5: Single pulse craters made with 800 nm, 160 fs pulses on diamond. The images were taken using differential interference contrast microscopy on the optical microscope. The energy for each pulse is given along with the peak fluence. The laser polarization was in the horizontal direction. Some of the craters may appear as hills for reasons outlined in Section 4.4.4.

goes below 12.5 J/cm^2 for this particular experiment. This splattering could occur at lower pulse energies because the fluence of the laser pulse is not high enough for

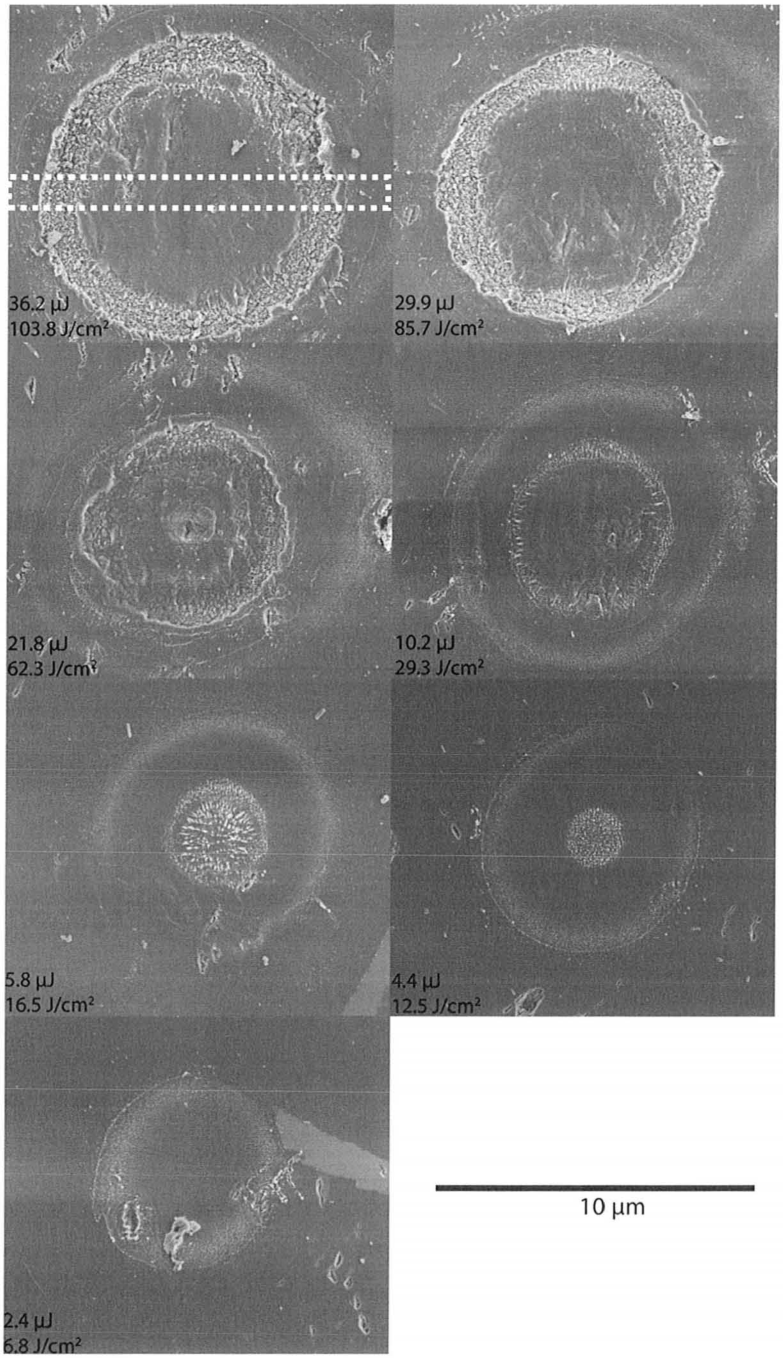

Figure 4.6: SEM images of select single pulse craters from Figure 4.5.

most of the excited material to be ablated and vapourized.

The optical microscope and SEM images appear to show that the higher energy single pulse craters have undergone less ablation in the center compared to the outer rough ring. However, these images can be misleading and to further investigate the topography of the craters requires using an AFM to take absolute height measurements. The experiment was first repeated to determine if these central features could be reproduced used the laser system. The same central feature with an outer rough ring at the higher energies was still present. AFM measurements of the higher pulse energy craters are shown in Figure 4.7. The ellipticity of the craters was due to the profile of the laser pulses which were slightly elliptical when viewed with the beam profiler for this particular experiment.

The AFM results confirm there is a central region which has undergone less ablation compared to the surrounding ring. The AFM measurements of craters made with pulse energies greater than 21.5 μJ appear very similar. Some ablation has occurred in the central region, with approximately 50 to 100 nm of diamond removed in the center. The outer ring is approximately 150 to 200 nm deep and is about $1 - 2$ μm wide. The outer ring disappears abruptly between the 21.5 μJ and 16.7 μJ pulse craters. The ring occurs in an outer region of the crater where the pulse in-

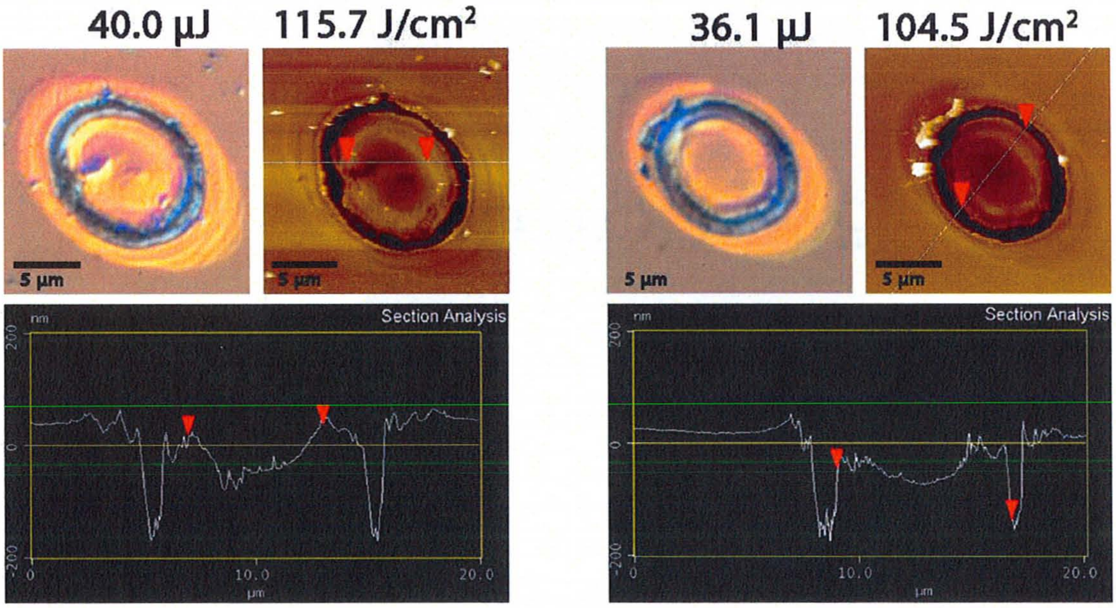

Figure 4.7: This figure is continued on the following page.

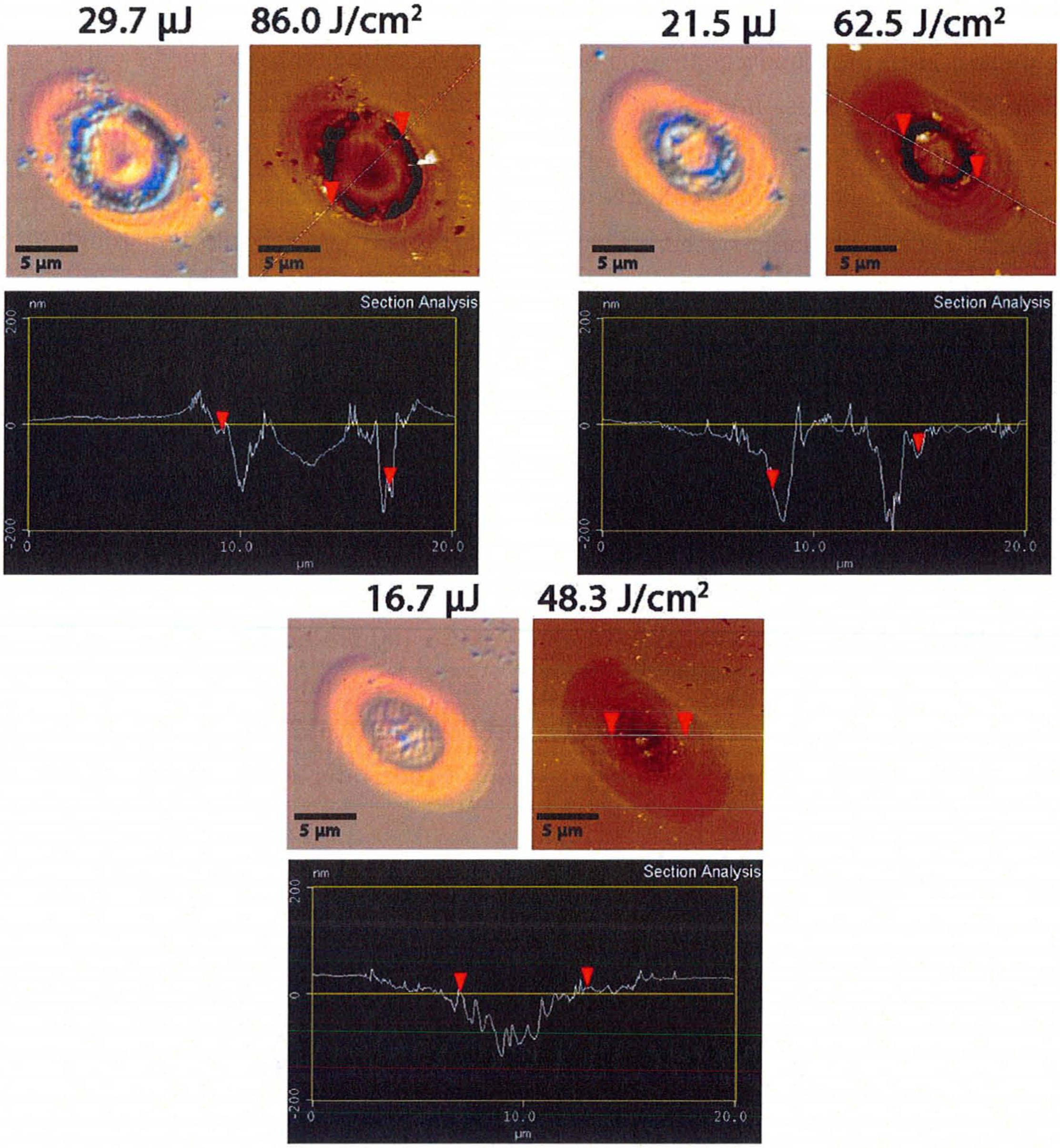

Figure 4.7: Optical DIC and AFM images of single pulse craters. The figure starts on the previous page. Each AFM image also contains a line and the depth profile along this line is given in the graph below each image. The red arrows correspond to the same points in the AFM image and the cross sectional profile. Note: these craters were from a separate experiment and are not the same as the craters shown in Figures 4.5 and 4.6.

tensity and the localized fluence is less than in the center of the crater. It appears that above a certain intensity and fluence the rate of ablation rapidly decreases. The central regions in the crater which receive a fluence above ~45 J/cm^2 then undergo less ablation creating the central protrusion and surrounding deep ring for the higher energy pulses.

Central features inside craters made with single femtosecond laser pulses have been previously reported. Craters made on InP using 800 nm, ~150 fs laser pulses with a 1/e^2 spot size of 5 μm were observed by by Borowiec *et al.* to have a central feature with a threshold which was higher than the threshold for normal ablation. However, AFM measurements showed this central feature actually underwent more ablation [35].

Bonse *et al.* irradiated indium phosphide with single pulse, 130 fs, 800 nm pulses to form surface craters [54]. The pulses were incident on the surface at an angle of 54° and were s-polarized. The effective spot size of the elliptical pulses was 100 μm by 60 μm. The threshold fluence for ablation of InP at this incident angle was $\Phi_{\mathrm{abl}}(54^\circ) = 0.30$ J/cm^2. At higher energies, above a peak pulse fluence of 1.76 J/cm^2 and at an incident angle of 54°, a permanent circular feature was observed in the center of InP craters. This central area protrudes out and more material ablates from around the edge of the crater leaving a deeper outer ring as observed in the single pulse craters made on diamond at higher energies.

Bonse was able to make time resolved measurements of the reflectivity of the irradiated area using a low powered probe laser. Four hundred femtoseconds after the initial irradiation, Bonse observed an increase in reflectivity over the entire ablated area. This was attributed to a sharp increase in the carrier density and suggested nonthermal melting was also taking place where a high density electron-hole plasma $(10^{21} - 10^{22})$ cm^{-3} was destabilizing the lattice before reaching a thermal equilibrium with the carriers [55, 56]. At 100 ps the craters for all energies appeared uniformly dark (less reflectance) because of absorption and scattering by ablating material. However, at 8 ns, the craters formed using higher energy pulses exhibited a central area which reflects more light surrounded by an outer dark ring where material was still being ablated.

Bonse attributed the formation of this central protrusion observed in craters made with higher pulse energies to the formation of a dense plasma on the surface of InP. It is believed a large amount of energy is deposited in a very thin layer on the InP surface due to non-linear absorption and an electron avalanche process. This highly excited layer is then expelled from the surface, carrying away most of the laser energy, and depressing any further ablation in this region. This argument is supported by the idea that there is a threshold for the formation of this central protrusion. At energies below this threshold the material is not as highly excited and energy is absorbed farther down into the lattice. This allows for ablation to occur at deeper depths and explains the ring pattern which is observed for these single pulse craters where the outer region of the crater, which was irradiated with a lower fluence, experienced the most material removal [54]. Similar features have been seen in GaAs irradiated with extreme ultraviolet femtosecond laser pulses. These features were also attributed to the formation of a high density plasma on the surface which limits the absorption depth [57].

One concern with the formation of this central feature in single pulse craters is the possible role played by satellite pulses. It is possible a reflective state is produced before the main pulse irradiates the sample if the pre-pulses were to excite electrons to the conduction band before the main pulse irradiates the surface. The carrier lifetime for single crystal CVD diamond has been measured to be from 170-580 ps depending on the number of defects (mainly higher levels of nitrogen). Lifetimes for HPHT were measured to be as high as 2.8 ns [58]. Free carriers generated on the surface by pre-pulses incident $\sim$7 ns before the main pulse should therefore be mostly recombined before the main pulse irradiates the sample. Also, to excite these electrons and form electron-hole pairs requires a nonlinear four photon process. The weaker intensity of the pre-pulses ($\sim$0.01% of the main pulse) makes this process unlikely. The 10 ps post-pulse could be of more concern as it is the strongest satellite pulse and the sample is in a highly excited state where free electrons can absorb single photons. However, for craters made without the neutral density filters which cause the 10 ps post-pulse the same overall features were seen.

Another feature present in the single pulse craters was ripples (LIPSS) perpendicular to the laser pulse polarization as seen in the optical microscope images from Figure 4.5. These LIPSS had a period of $600-700$ nm and can be classified as LSFL. For pulse energies from 16.7 μJ down to 5.8 μJ ripples were seen which form in the central region and the outer edge perpendicular to the laser polarization. The LIPSS seen in an optical microscope are not as visible in a SEM. However, they can be seen in the SEM images of the 21.8 and 10.2 μJ single pulse craters in Figure 4.6.

LIPSS have been known to form from irradiation by single laser pulses with durations on the order of nanoseconds and greater [24]. However, for femtosecond laser pulses LIPSS are generally only observed when areas are irradiated with two or more pulses and become more noticeable when multiple pulses irradiate the same area [27]. Most of the work done on ripple formation outlined in Section 2.2 assumes there is an interaction between the laser light and a surface scattering or diffracted wave [24]. The LIPSS which form require initial seeding pulses to roughen the surface and create scattering centers. One reason for the formation of LIPSS on the CVD diamond samples with a single laser pulse was the initial quality of the diamond surface. In Figure 4.5, the 3.3 μJ and 1.5 μJ single pulse craters both exhibit ripple patterns which form from areas where initial surface defects were present. Similar energy pulses, such as the 2.4 μJ and 1.9 μJ pulses, both show no ripple formation because no surface defects were initially present in these areas. Figure 4.8 shows how surface defects provide the initial scattering centers required to form LIPSS. The LIPSS form around the defects and are mostly linear and perpendicular to the polarization although there is also a tendency for these LIPSS to have spherical wavefronts around the defect. It will be shown in later sections that multiple pulses lead to more linear LIPSS patterns perpendicular to the laser polarization.

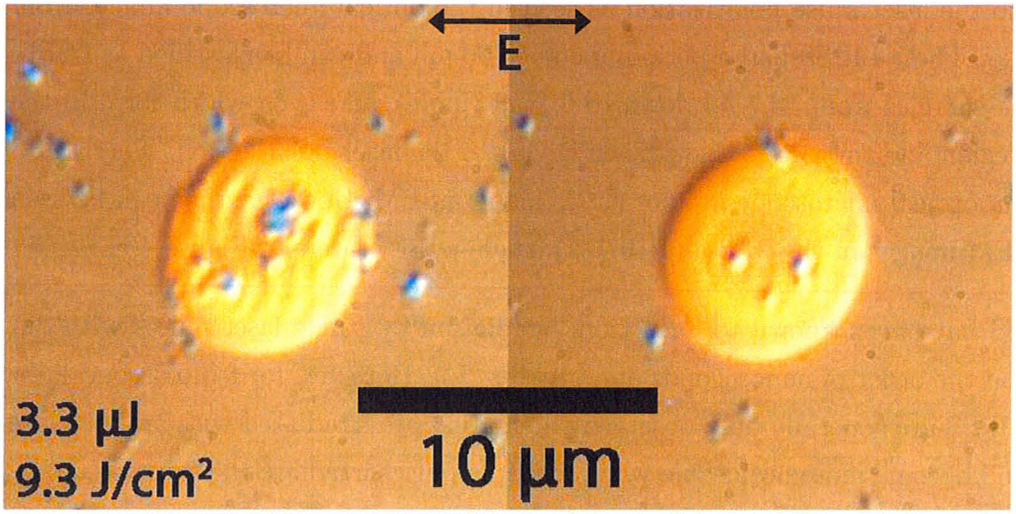

Figure 4.8: Comparison of two craters both made using single 3.3 μJ pulses with different initial surface conditions. The images were taken in Nomarski mode on the optical microscope.

A TEM sample of the 36.2 μJ pulse from Figure 4.6 was made using a FIB in the area indicated by the white rectangle to further analyze this crater and the subsurface modifications. The sample was made by taking a slice across the entire diameter of the crater. An overview of the thinned slice is shown in Figure 4.9. Arrows (a) and (c) point to where the slice goes through the rough areas of the outer ring. The dark lines present in the TEM image are caused by bend contours where the bending of the crystal causes the diffraction condition to be locally met in these areas and the electrons are more strongly diffracted out of the back focal plane aperture. These bend contours are unavoidable because the sample is quite thin (less than 100 nm). The tip of arrow (a) points to a line that is not a bend contour. This line goes across the entire crater and has a profile which would be expected for a conventional crater where the deepest part is in the center. However, there is no change in the crystal structure around this line and it appears to be caused by a change in thickness of the sample from ion milling. It is possible that some modification which cannot be detected has caused the area around the crater to be milled faster by the Ga ions in a FIB. The dark protective platinum and amorphous carbon layers are also shown. These layers are deposited by electrons and Ga ions to protect the surface during the milling and thinning process.

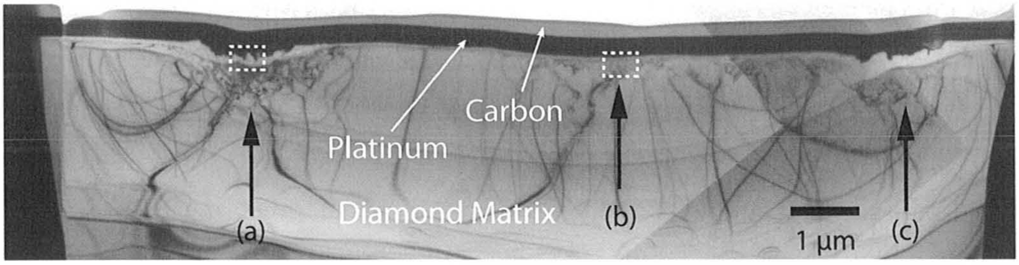

Figure 4.9: Bright field image showing a section of the 36.2 μJ single pulse crater from Figure 4.6

Figure 4.10 shows two magnified images of the top surface. Figure 4.10a is a bright field TEM image of the area inside the rectangle pointed to by arrow (a) in Figure 4.9. Figure 4.10b is the area in the rectangle pointed to by arrow (b) in Figure 4.9. The modified layer in Figure 4.10a is approximately 200 nm thick. This layer is very rough on the surface interface and much smoother on the interface between the modified layer and the main diamond matrix. Figure 4.10 shows how the modified layer looks in the center of the sample where less ablation has occurred. It is smooth both on the surface (which is now covered in platinum) and at the interface between the modified layer and diamond matrix. It is also much thinner (~50 nm) compared to the modified area in the rim region.

This modified layer is not large enough to obtain a selected area or convergent beam electron diffraction pattern of only this region. Selected area diffraction patterns which also included parts of the platinum layer had very faint diffuse rings. These rings are evidence that this modified layer could be polycrystalline diamond with very small grain sizes. Some amorphous carbon could also be present. The modified layer could have formed by nonthermal melting and a destabilization of the lattice. However, it is more likely this area was not in such a highly excited state and only normal melting took place because there was not enough energy to ablate the material in this region. The thickness of the modified layer at the rim compared to the center also supports the proposed mechanism that less ablation occurs in the center of the crater because the energy is absorbed on a very thin surface layer of highly excited plasma. In the outer area around the rim the energy should then be absorbed at greater depths where the effective absorption coefficient is smaller. The modified area where the crystal structure was damaged should then be thicker in this region as is confirmed by the TEM image.

The rough topography of the rim region compared to the inner crater region at the diamond-air interface supports the possibility that a different mechanism was responsible for ablation in each region. Evidence of different ablation mechanisms responsible for ablation in different areas of the same single pulse crater has been presented elsewhere [59]. Phase explosion has been proposed to occur in the center of craters which receive a higher fluence and Coulomb explosion has been proposed in outer regions which receive a lower fluence [29]. The rough outer ring observed in diamond could be caused by Coulomb explosion the created the observed micropatterning. Ablation in the central protrusion could then be dominated by a different mechanism.

The sharp optical interfaces between the air-modified and modified-diamond interfaces has been previously suggested by von der Linde *et al.* [60] in other materials. Single pulse craters were made on a number of semiconductors and metals using ultrashort laser pulses. Reflectivity measurements using a probe laser pulse produced Newton-ring interference fringes. By varying the wavelength of the probe pulse and observing changes in the ring pattern, they could infer the newton-rings were caused by interference between two optical interfaces. The formation of this interface was associated with a rarefaction wave which formed during the isentropic expansion of the surface layer into vacuum. Hydrodynamic models predict both the air-modified and modified-matrix interfaces from this wave should be very abrupt [60].

The profile of the craters from the AFM sections shown in Figure 4.7 could also be related to this rarefaction wave. The 21.5 μJ pulse in Figure 4.7 which does not show any impact of the Gaussian profile fluence has been seen in single pulse craters made on metals and semiconductors where a flat surface forms inside the crater [57]. This uniformity is believed to occur at lower energies where energy is absorbed into the solid at some characteristic optical penetration depth. A rarefaction wave then propagates into the solid and is reflected. The energy is absorbed in a uniform layer which is relatively independent of the fluence over a range of values [60].

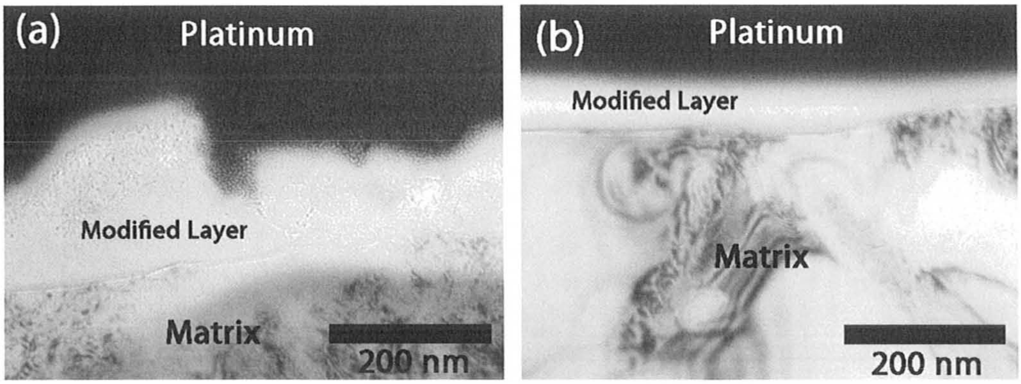

Figure 4.10: (a) Bright field TEM image of the area in the rectangle pointed to by arrow (a) in Figure 4.9. (b) Bright field TEM image of the area in the rectangle pointed to by arrow (b) in Figure 4.9.

4.4.5 Multiple Pulse Craters and Lines

LIPSS formation was first investigated in craters made with multiple laser pulses. Figure 4.11 is an optical microscope image of a series of craters made at different energies using a different number of pulses. As the number of pulses per crater increased, more pronounced LIPSS can be seen with all four pulse energies. The central protrusion observed for the single pulse craters became less pronounced as the number of pulses that irradiated the same crater increased. At the higher energies, ripple patterns were more noticeable after two pulses as opposed to some of the lower pulse energies which require many more pulses to produce LIPSS. It can take ten or more pulses to clearly see the ripples using pulse energies below the single pulse threshold for ablation. The effects of initial surface conditions are also quite noticeable at the lower energies and for low numbers of pulses. At higher energies and for large numbers of pulses the LIPSS pattern which forms no longer depends on the initial surface conditions. The LIPSS formed at all energies appeared to have a period of 600-650 nm. Lower period LIPSS (possibly HSFL) may be present. However, these LIPSS are hard to view in a light microscope.

Figure 4.12 shows select SEM images of craters made with a high number of pulses at lower energies. The N=10 pulse crater has only LSFL with a wavelength of ~600 nm as previously measured in optical microscope images. As the number of

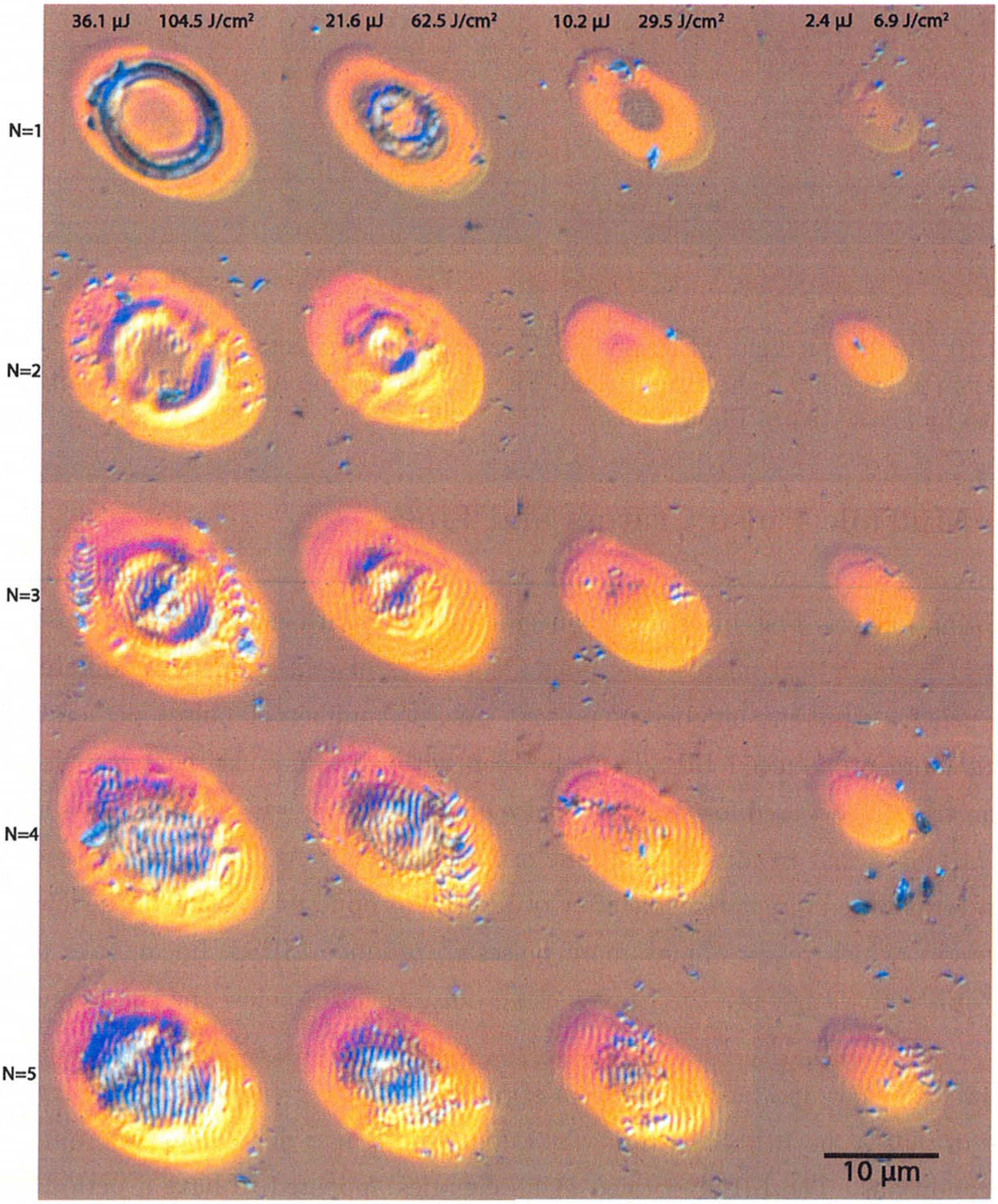

Figure 4.11: A comparison of single and multiple pulse craters made on diamond. The energy and peak fluence per pulse are given and remain constant down each column. The number of pulses, N, is the same across each row. The images were taken on the optical microscope in Nomarski mode. The polarization of the pulses was in the horizontal direction.

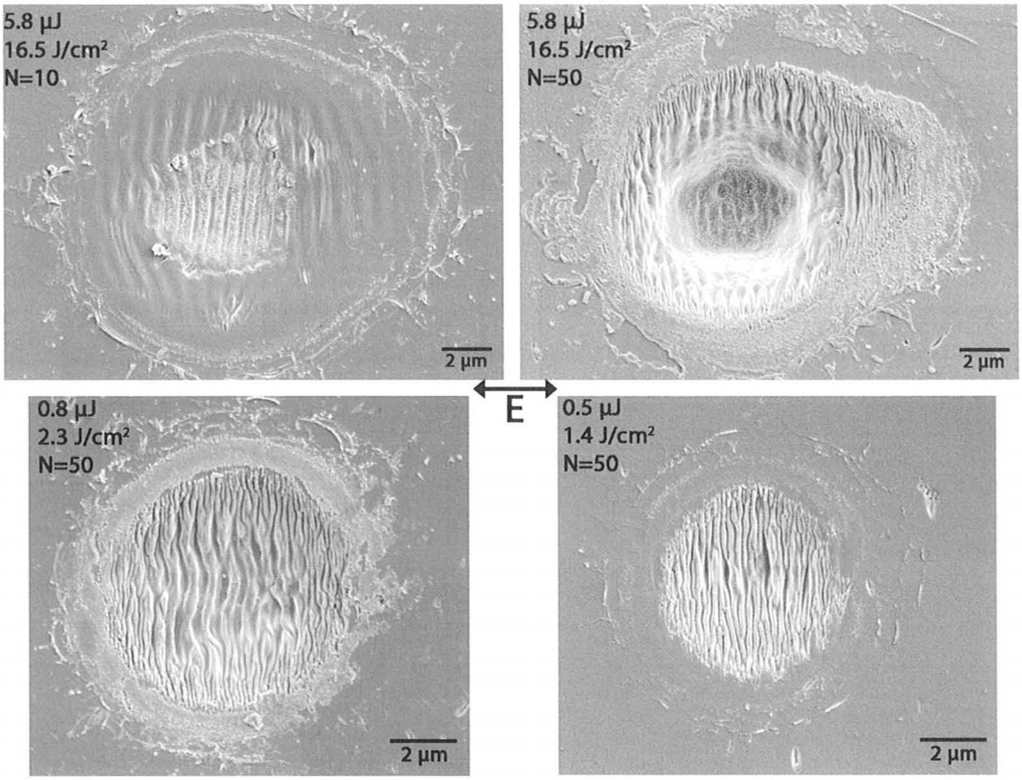

Figure 4.12: SEM images of craters formed with a high number of pulses at a low energy. The polarization of the pulses was in the horizontal direction.

pulses increases from N=10 to N=50, LIPSS can be seen on the edge of the crater which have a much higher spatial frequency (~210 nm). These HSFL only appear in areas where there is a low fluence per pulse. Fifty-pulse craters made with lower pulse energies have HSFL covering more of the crater area as shown in the lower right hand image of Figure 4.12. There was still a tendency for LSFL to form in the center of the craters even at these lower energies where the fluence is the greatest. All of these LIPSS formed perpendicular to the direction of the laser polarization which is in the horizontal direction (across the page) unless otherwise stated.

To further investigate these HSFL, a TEM cross section was made in an area of a crater where HSFL were present. Figure 4.13a is an SEM image of the crater used to make the cross section. The white rectangle denotes the area used to make the slice. Figure 4.13b is an overview of the section. The top dark layer is the

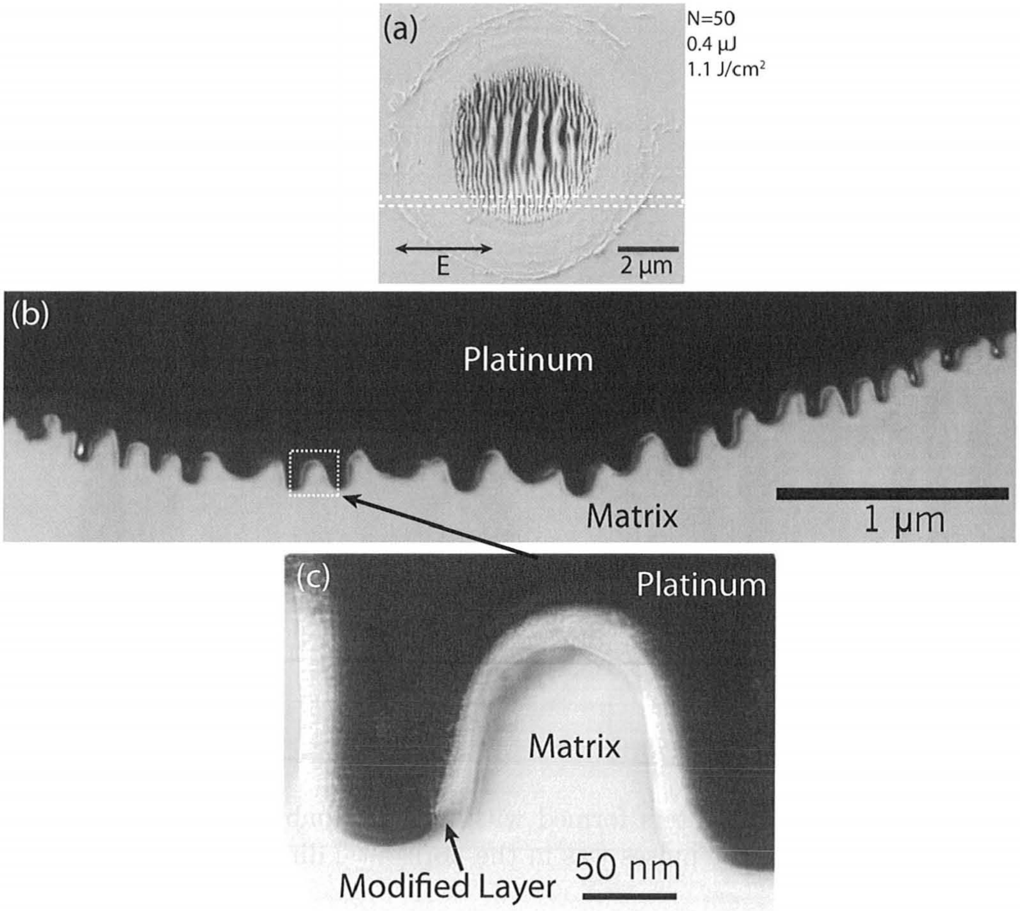

Figure 4.13: (a) SEM image of the crater used to make the cross section. (b) A bright field TEM image of the section. (c) a magnified view of the area inside the white rectangle from (b).

protective platinum layer. Next to the diamond this layer appeared lighter because the platinum was first deposited with electrons to minimize damage to the surface by ions as described in the previous chapter. Figure 4.13c is a magnified area of one of the ripples. Inside the ripple the BF image and selected area electron diffraction patterns indicate that this region is still single crystal and part of the main diamond matrix. There is a thin modified surface layer that is about 25 nm thick. This layer has a relatively uniform thickness over the entire ripple.

LIPSS formation on materials is often done by making lines with laser pulses. If the sample is being translated slow enough so that each pulse almost overlaps, the

LIPSS formed from each pulse will reinforce or seed the production of LIPSS by the next pulse. Figure 4.14 shows an overview of some of the lines made at a variety of pulse energies on diamond. At higher fluences LIPSS with a spacing of approximately 550-600 nm were the dominant feature. These LSFL were the main feature present in lines made with pulse energies greater than 1.9 μJ. At lower pulse energies, LIPSS with a spacing of 230-240 nm became more dominant. These LIPSS were also present on the edge of lines made with higher pulse energies where the fluence would be much less than in the center. Lines made with lower pulse energies of 1.9 and 1.4 μJ had both high and low spatial frequency LIPSS present. Because the lines were made by moving the sample as it was irradiated, even the center of a line experienced a low fluence from an individual pulse as the sample was translated to form the line. In the low energy pulses the LSFL could form as the center of the pulse moved over an area. The HSFL would then form as the pulses moved away and the edges of pulses, which have a lower fluence, irradiated the same area. These results for lines on the surface were consistent with the results for multiple pulse craters where LSFL formed at higher fluences per pulse and HSFL were more dominant in areas irradiated with many pulses that had a low fluence per pulse.

A TEM cross section was taken of the line made with 13.8 μJ pulses in the area marked by the white rectangle in Figure 4.14 to investigate the structure inside the lower spatial frequency ripples. Figure 4.15a is a bright field TEM image showing an overview of the TEM slice. Figures 4.15b and 4.15c show magnified images of the ripples. They are very similar to the fine ripples from Figure 4.13 only with a longer period. The modified layer is much thicker ($\sim$50 nm) compared to the layer observed in the fine ripples. The bright field images show the center of the ripple is still part of the main diamond matrix. There is also a very sharp boundary between the modified layer and the main diamond matrix.

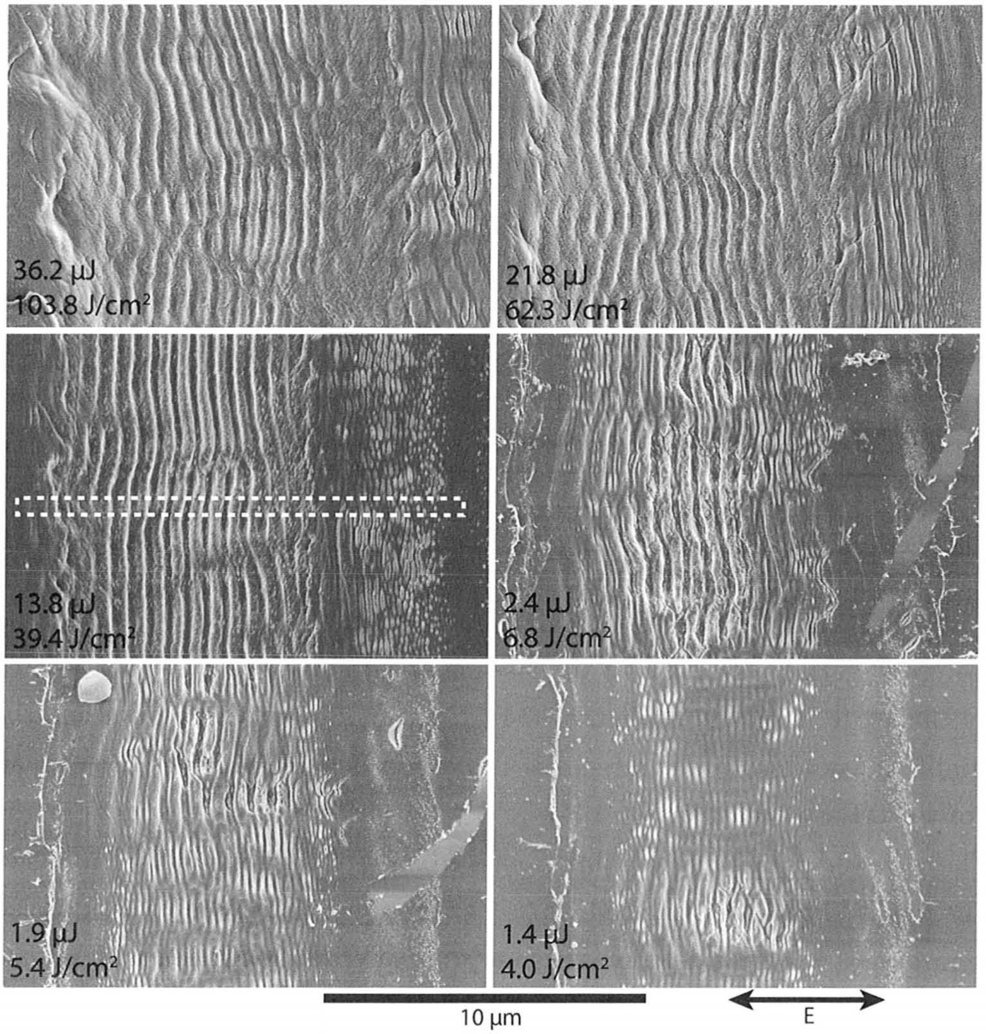

Figure 4.14: Lines made on diamond. The pulse energy and fluence given are the energy per pulse. The pulses were incident at a rate of 1 kHz while the sample was translated at 500 μm/s.

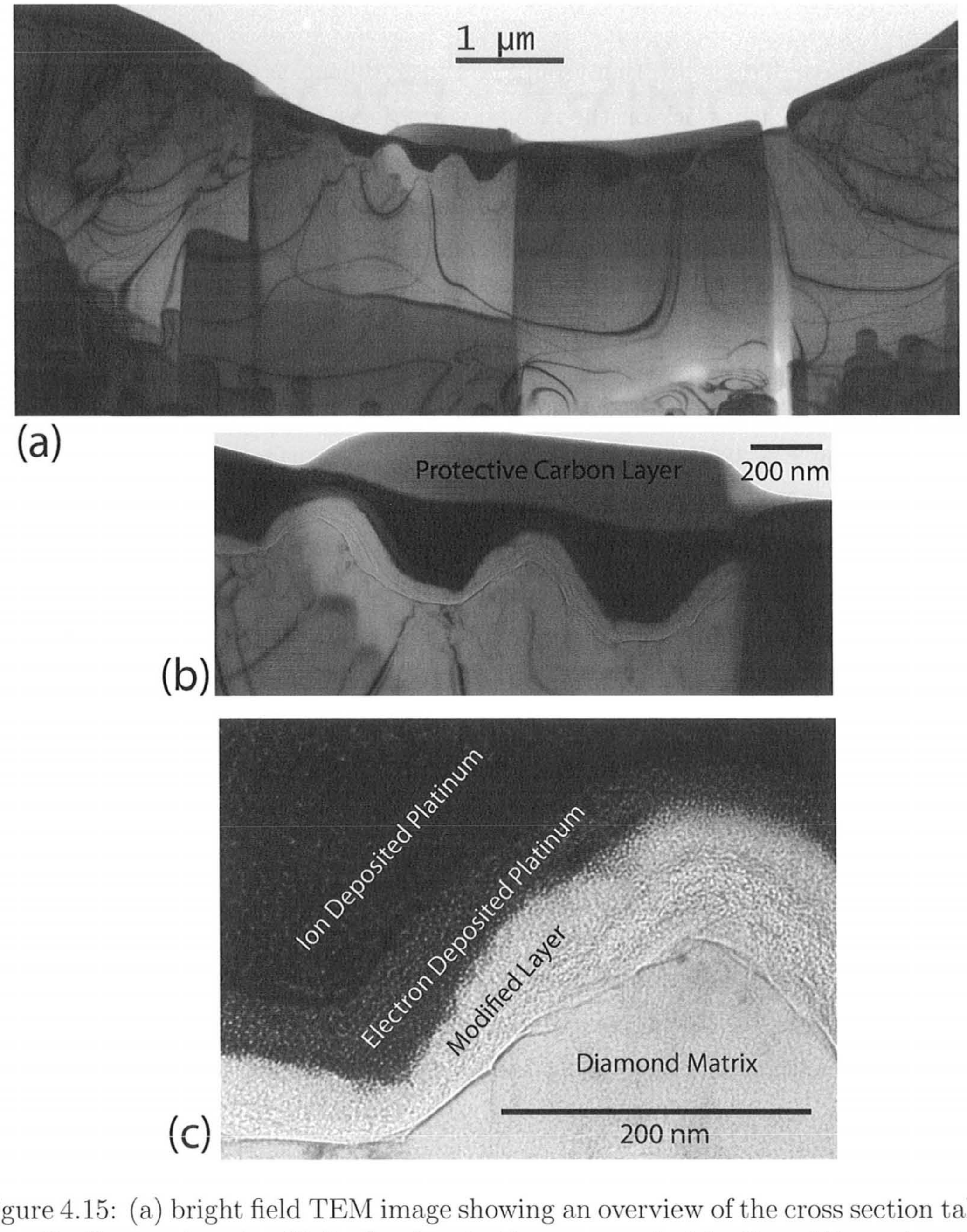

Figure 4.15: (a) bright field TEM image showing an overview of the cross section taken from the line made using 13.8 μJ pulses in the area marked by the white rectangle in Figure 4.14. (b) and (c) show magnified areas of the ripples from (a).

4.4.6 Discussion

There has been research done by other groups on the modification of diamond surfaces by laser pulses. Very early work on the interaction of laser light with diamond films was performed by Ageev *et al.* [61]. They grew diamond films with a thickness of 15-35 μm. The band gap of this diamond was $E = 5.4$ eV. The films were modified with a CO_2 laser ($\lambda = 10.6\ \mu$m, $\tau = 3\ \mu$s, $h\nu = 0.12$ eV) which produced ripples perpendicular to the direction of polarization. The LIPSS had a period of approximately 10 μm or about the wavelength of the laser.

Ozkan *et al.* [62] observed LIPSS on diamond using ultraviolet femtosecond laser pulses ($\lambda = 248$ nm, $\tau = 380$ fs, h$\nu = 5$ eV). Irradiating the surface of polycrystalline CVD diamond with 100 pulses that had a peak fluence of 1.5 J/cm^2 per pulse produced these surface ripples. The ripples were perpendicular to the laser polarization and had a period on the order of the laser wavelength. They attributed the formation of these features to the same mechanism proposed by Sipe *et al.* where the incident laser creates a reflective plasma and a surface scattering wave interferes with the incident laser radiation. However, it was also observed that ripples formed in some regions with a period substantially less than the wavelength of the laser (on the order of $50 - 100$ nm or a quarter of the laser wavelength). These ripples patterns appear similar to the lines in Figure 4.14 where both 550-600 nm and 230-240 nm ripples (which are also about one quarter of the laser wavelength) are present [62].

LIPSS parallel to the direction of laser polarization have also been observed on diamond films. Wu *et al.* [63] observed c-type LIPSS with a period close to one quarter the wavelength of the laser using 100 fs, 800 and 400 nm laser pulses with a 1 kHz repetition rate. LIPSS perpendicular to the direction of polarization with a periodicities of 750 nm and 210 nm were also observed. These LIPSS were made using 800 nm pulses [63]. In these cases the incidence angle was near normal (5°). To account for the spacing of these LIPSS which do not conform to the theory presented by Sipe, Wu also tried to take into account nonlinear effects. Free carrier generation by the laser pulses was measured by Jeschke *et al.* [64] to give an index of refraction for diamond as high as $n = 4$ directly after laser pulse irradiation. This value was measured using time resolved reflectivity measurements. The periodicity of the HSFL observed by Wu *et al.* would be in better agreement with Sipe theory on LIPSS formation if this index of refraction was used instead.

LIPSS were observed on bulk diamond samples using 800 nm, 100 fs pulses by Dumitru *et al.* [52]. The ripples on the diamond surface had a wavelength of ~610 nm and were perpendicular to the direction of the laser polarization. These ripples were seen for fluence ranges from 1.5-4.7 J/cm^2 on craters made with 1000 pulses. LIPSS with a much smaller period have also been made on single crystal diamond by Shindoa *et al.* [65]. Using 120 fs, 800 nm, pulses lines were made by moving the sample at 500 μm/s with a pulse repetition rate of 250 kHz. These lines produced grooves that had a spacing of ~146 nm. The grooves had a width of 40 nm and were very uniform compared to ripples observed in this thesis. The depth of these grooves was found to be ~500 nm by milling below the surface with a FIB. The depth was also found to depend on the repetition rate of the pulses and the scanning speed. Shindoa *et al.* attributed the formation of these deep grooves to the same mechanism proposed by Bhardwaj *et al.* [6] for the formation of nanoplanes inside fused silica. If the grooves formed by this mechanism the spacing should be close to $\frac{\lambda}{2n} = 167$ nm. The spacing of 146 nm was believed to be close enough to be in agreement with this value.

LIPSS on bulk diamond have also been observed by Huang *et al.* [66]. Natural, single crystal, optical grade diamond was irradiated with 800 nm, ~125 fs laser pulses at a repetition rate of 1 kHz. The samples were irradiated in air. LIPSS with a spacing of 170-190 nm were observed in areas irradiated with 3000-8000 pulses. The peak fluence of each pulse was 1.9-2.8 J/cm^2 (slightly above the ablation threshold for a single pulse). These HSFL were also very uniform grooves which looked similar to the grooves observed by Shindoa *et al.* However, no ion milling was done to determine if these grooves also had a high depth to width ratio. LIPSS were also made on graphite by Huang *et al.* [66]. The spacing and structure of these LIPSS was very similar to the spacing and structure of LIPSS observed on diamond. A summary of LIPSS observed on diamond in this thesis and by other research groups is given in Table 4.1.

The LIPSS on diamond observed in this thesis had a spacing that is not close to

Table 4.1: LIPSS spacing observed on diamond. ($\perp$) and ($\parallel$) denote LPPS perpendicular and parallel to the laser pulse polarization respectively.

Research Group	Material	Laser Wavelength (λ)	Pulse Duration	LIPSS Spacing (Δ)	λ/Δ
LIPSS in this thesis	Single Crystal CVD Diamond	800 nm	$\sim$190 fs	550-600 nm ($\perp$)	1.3-1.4
				200-250 nm ($\perp$)	3.2-4
Ageev *et al.* [61]	Polycrystalline Diamond Film	1060 nm	$\sim$3 μs	1060 nm ($\perp$)	1
Ozkan *et al.* [62]	Polycrystalline CVD Diamond	248 nm	$\sim$380 fs	248 nm ($\perp$) 50-100 nm ($\perp$)	1 2.5-5
Wu *et al.* [63]	Polycrystalline CVD Diamond	800 nm	$\sim$100 fs	750 nm ($\perp$)	1.1
				210 nm ($\perp$)	3.8
				210 nm ($\parallel$)	3.8
		400 nm	$\sim$100 fs	380 nm ($\perp$)	0.95
				90 nm ($\perp$)	4.4
Dumitru *et al.* [52]	Polycrystalline CVD Diamond	800 nm	$\sim$100 fs	610 nm ($\perp$)	1.3
Shinoda *et al.* [65]	Single Crystal CVD Diamond	800 nm	$\sim$ 120 fs	146 nm ($\perp$)	5.5
Huang *et al.* [66]	Single Crystal Natural Diamond	800 nm	$\sim$125 fs	170-190 nm($\perp$)	4.2-4.7

$\lambda = 800$ nm or $\lambda/n_{800} = 333$ nm which would correspond to Sipe theory. The spacing is not close to $\lambda/2n_{800} = 167$ nm which would correspond to the theory presented by Bhardwaj *et al.* [6]. It is also not close to $\lambda/2 = 400$ nm or $\lambda/2n_{400} = 163$ nm which would correspond to Sipe theory with SHG. It is unclear what mechanism is responsible for LIPSS formation in diamond. A summary of the spacings predicted by each theory is shown in Table 4.2. The refractive index of diamond is $\sim$2.40 for 800 nm light. Some theories for HSFL formation consider SHG. The refractive index of diamond at 400 nm is $\sim$2.45 [51]. There is very little wavelength dependence on the refractive index over this range of wavelengths. In general, if no wavelength was specified a refractive index of $n = 2.4$ was used for calculations.

The current theories presented in Table 4.2 do not give λ/Δ values which match the measured values for either the LSFL or the HSFL observed in this thesis. A nonlinear Sipe theory presented by Bonse *et al.* [26] may provide the best explanation for the period of the LIPSS observed on diamond. This theory takes into account

Table 4.2: LIPSS periods (Δ) predicted by different mechanisms for the formation of LIPSS. $n_{800} = 2.40$ and $n_{400} = 2.45$.

LIPSS Formation Theory	Formula ($\Delta =$)	Δ for 800 nm Light Pulses	λ/Δ
Sipe Theory	λ	800 nm	1
Sipe Theory	λ/n_{800}	333 nm	2.4
Sipe Theory with SHG	$\lambda/2$	400 nm	2
Sipe Theory with SHG	$\lambda/2n_{400}$	163 nm	4.9
Bhardwaj *et al.* [6]	$\lambda/2n_{800}$	167 nm	4.8

changes in the the refractive index because of free carrier generation. If SHG of light is also considered it may be possible to calculate peaks in the efficacy factor that correspond to the spacing of LIPSS observed on diamond in this thesis.

The LIPSS that formed on single crystal diamond did not have the uniformity that is observed on some materials irradiated with femtosecond laser pulses. The lines made on the surface with lower pulse energies produced both HSFL and LSFL. Figure 4.14 shows an example of these lines. In this figure the lines made with pulse energies ≤ 1.9 μJ generated both HSFL and LSFL in the center of the lines. There appeared to be an instability between the LSFL and HSFL. It is possible that the initial surface conditions played more of a role at this lower pulse energy. The grooves observed by Shindoa, Huang, *et al.* used a much higher number of pulses at energies near threshold. The surface lines presented in this thesis were made with one pulse incident every 0.5 μm the sample was translated. Using a higher number of pulses may produce more uniform lines and mitigate the effects caused by the initial surface conditions. The LIPSS formed in craters made with 50 laser pulses shown in Figure 4.12 also show a high sensitivity to the local fluence. LSFL in the form of ripples break into smaller ripples and form HSFL at the outer regions of the crater. These outer regions received less fluence. Other dielectric materials have also been shown to produce LSFL which break into HSFL in a similar pattern to the one seen in diamond [26, 29, 67].

Other important observations about these ripple structures came from cross sections taken made with a FIB and viewed in a TEM. Both the HSFL and LSFL had a similar structure. The inside of the ripples was part of the main diamond matrix and appeared to be unmodified by the laser. Both the HSFL and LSFL were covered in a thin modified layer. The LIPSS must form on the surface and only localized areas in the valleys of ripples undergo more ablation than the ripple peaks. This has been suggested by other groups who used Raman spectroscopy to determine only a thin modified layer was present on LIPSS made on diamond [66]. This rules out any mechanisms for the formations of LIPSS where a highly excited molten layer relaxes to form a periodic surface.

The depth to width aspect ratio of LIPSS made on single crystal diamond in this thesis is quite different from the depth to width aspect ratio of LIPSS made on single crystal by some other groups. The ripples observed in this thesis had more of a sinusoidal profile with a depth to width ratio of ~1. These types of LIPSS on diamond have been observed elsewhere (e.g. Wu *et al.*). However, the LIPSS made by Shinoda, Huang *et al.* [65, 66] could be better described as grooves instead of ripples. These grooves were only 40 nm wide (compared to an overall LIPSS period of 146 nm) and had a profile similar to a comb function instead of a more smooth sinusoidal function as seen in Figures 4.13 and 4.15. The formation of these grooves could be explained by the theory for the formation of nanoplanes in the bulk of dielectrics presented by Bhardwaj *et al.* [6] because the grooves appear very similar to bulk planes only on the surface. The spacing of the grooves was also close to the spacing that would be expected for the theory presented by Bhardwaj *et al.* The LIPSS in this thesis do not have the high aspect ratio or spatial period required for this mechanism to seem appropriate.

4.5 Bulk Experiments in Diamond

4.5.1 Overview

Femtosecond laser pulses with a central wavelength of 800 nm were focused in the bulk of CVD diamond plates using a 50x microscope objective for all of the bulk experiments. The pulses had a duration of ~170 fs. The diamond plates were 500 μm thick and the pulses were focused 250 μm below the surface. The pulses were initially focused on the surface. The 50x microscope objective was then translated 100 μm closer to the diamond surface. The depth below the diamond surface the pulses focused to is approximately equal to the depth below the surface the pulses would focus to in air multiplied by the index of refraction for diamond (assumed to be ~2.5). Therefore, the pulses should be focused ~250 μm below the diamond surface. The sample was then translated while being irradiated to make lines in the bulk. The lines started in the bulk and the sample was translated to have the line come out perpendicular to one of the sides of the diamond plate. All of the bulk experiments were also performed with the diamond samples in a vacuum of ~0.05 mbar.

One challenge with studying diamond modifications in the bulk is standard grinding and polishing techniques to remove material for accessing the interior of samples is not possible because diamond is too hard. A FIB can only remove a couple microns of material in a reasonable amount of time and accessing the lines from the top of the sample would not be possible as the modified area is supposed to be 250 μm below the surface. The side of the sample where the lines exit the plate had to be used to make TEM specimens.

The fluence values specified in Figure 4.17 and throughout the work done on bulk diamond are the values which apply to surface irradiation using a 50x microscope objective. However, non-linear effects which cause self-focusing will change the spot size of the laser pulse inside the sample. Another concern with focusing in the bulk is spherical aberration effects. Spherical aberration in the microscope objectives cause pulses to focus over a certain range along the optical axis. When focused inside a material, this range will be increased approximately by a factor of n. Refraction at the dielectric surface (diamond in this case) will also cause rays incident at higher angles to the surface normal to be focused farther along the optical axis than rays incident at an almost normal angle to the surface. Therefore, even if there was no spherical aberrations in the lens, refraction at the dielectric surface would cause a spreading of the focal point into a focal volume along the optical axis in a way similar to spherical aberration in the lens [68]. Pulses were also focused through the sample chamber window which would act as as two dielectric surfaces because the pulses must propagate through the window. The length along the optical axis which the focus is spread out over is called the longitudinal spherical aberration length. This length will be larger if the numerical aperture (NA) of the lens is high and the maximum incidence angle on the dielectric interface for light rays focused by the microscope is far from normal incidence. The 50x microscope objective has a NA=0.42 and therefore these considerations should to taken into account [69].

The fluence values quoted throughout this section are therefore only estimates. A more appropriate estimation would be an energy per volume instead of area which takes into account the focal volume due to spherical aberration and gives an accurate Rayleigh range. However, this value would be difficult to measure and calculate at the high intensities being used where nonlinear effects in diamond must be included.

4.5.2 Initial Observations

Figure 4.16 is an optical microscope image of a single crystal diamond plate after irradiation to form lines in the bulk. The microscope has been adjusted to focus into the bulk of the sample so that the subsurface changes can be seen. The laser beam was moved from left to right out over the edge of the sample at 500 μm/s. The top dark line which has a uniform thickness was a surface line made to track the position of the subsurface modification. At the higher pulse energies, darker regions can be seen along the line. These areas appear very wide at the higher energies; however, they are not uniform and the dark areas appear discontinuously along the line as seen in Figure 4.16. Other samples were also irradiated to form lines in the bulk using lower scanning speeds. These lines also exhibited the same dark appearance when viewed in the optical microscope.

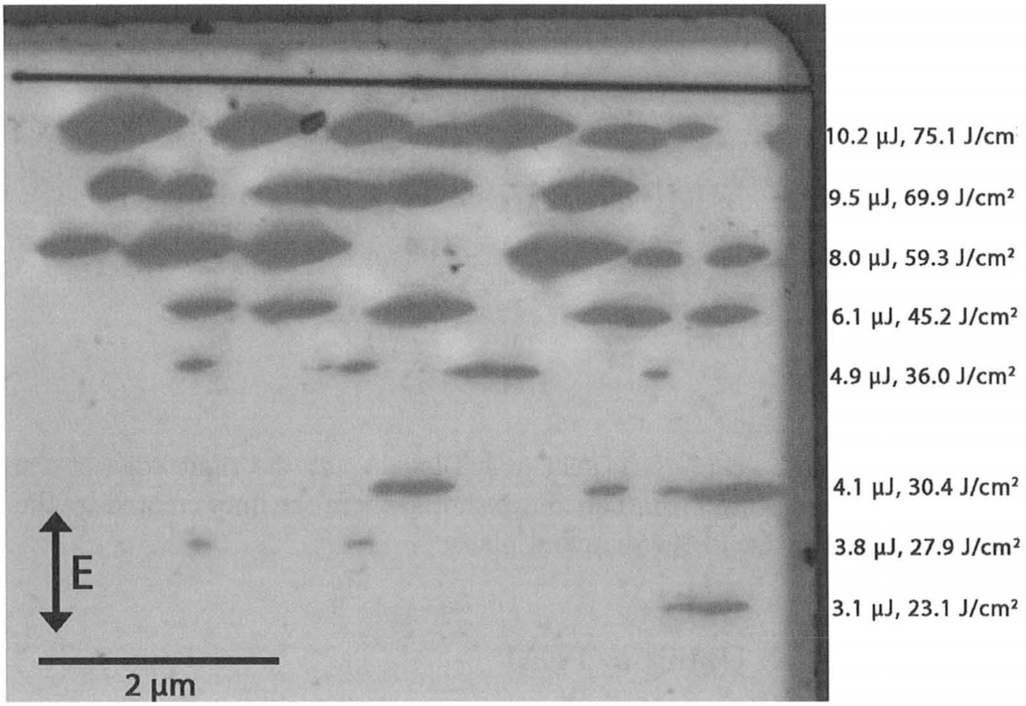

Figure 4.16: Optical microscope image focused into the bulk of transparent diamond. The polarization is in the vertical direction, perpendicular to the horizontal scan direction. The lines were made by translating the sample at 500 μm/s while the pulses were incident at a rate of 1 kHz.

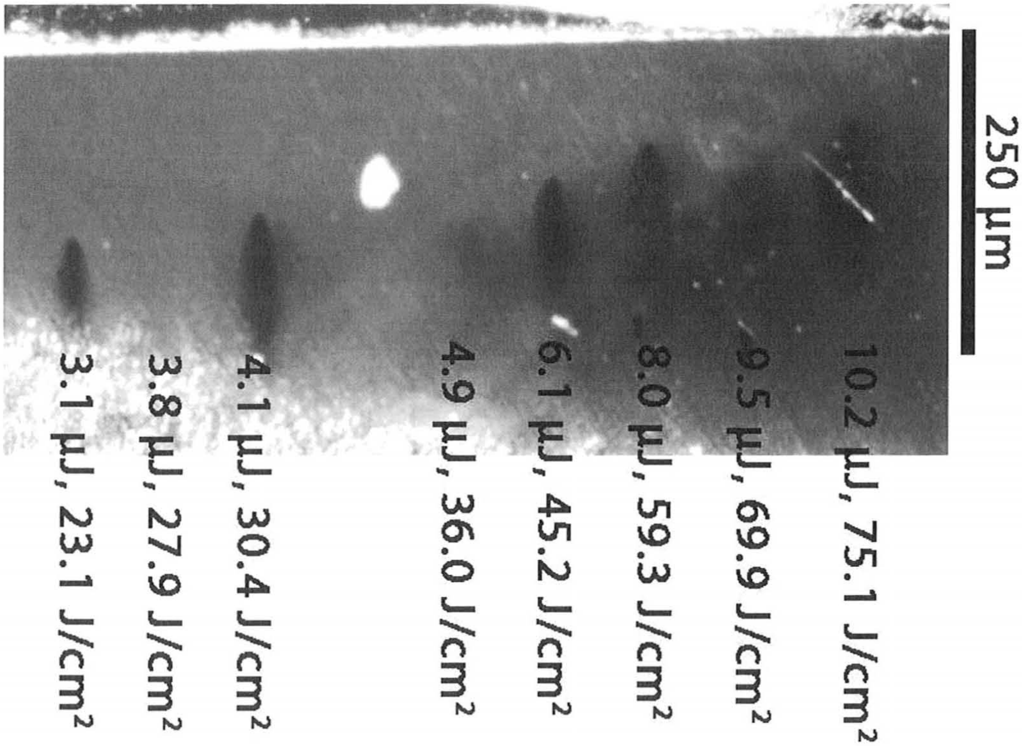

Figure 4.17: Optical microscope dark field image looking at the right edge of the diamond plate shown in Figure 4.16. The image shows where the lines created by the laser exited through the edge of the diamond plate.

4.5.3 Bulk Studies Using a TEM

An attempt was made at polishing the side of the diamond sample where the lines made in the bulk exited the sample. However, only a small amount of material could be removed. The results are shown in Figure 4.17. The polishing revealed that although the pulses were supposed to be focused ~250 μm below the surface, which corresponds to the bottom edge of the scale bar in Figure 4.17, the modified area appeared well above the focus especially at the higher pulse energies. It is possible that self-focusing, which would be more dominant at higher intensities, caused this shift in the vertical focus of the pulse [70].

A SEM image of the sample area presented in Figure 4.17 is shown in Figure 4.18. The most interesting feature is the cracks which have formed in very specific

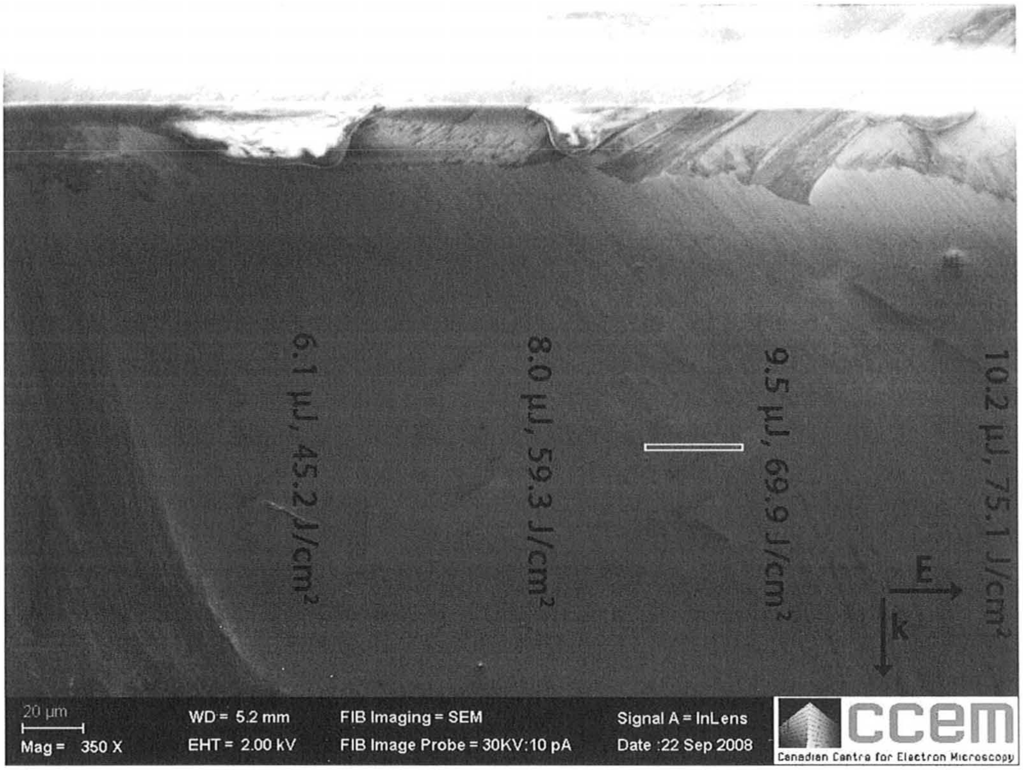

Figure 4.18: SEM image corresponding to the area shown in the optical microscope image from Figure 4.17. The energy labels are placed to the right of the modified area.

directions. The cleavage planes for diamond are the {111} planes [71]. The diamond was cut to have {100} type edges. Therefore, the angle of these cracks corresponds to the cleavage direction on the surface. No LIPSS could be seen on the exit surface.

A TEM sample was made using a FIB in the area marked by the white rectangle in Figure 4.18. The slice was taken parallel to the top surface shown in Figure 4.16 or perpendicular to the side in Figure 4.18. A bright field TEM image of the slice is shown in Figure 4.19. The only feature on the sample is the crack which goes back into the sample from the surface at an angle consistent with it being along a {111} type plane. The bend contours end at the crack indicating it is different from the main diamond matrix. A magnified image of this area is shown in Figure 4.20. The crack is approximately 200 nm thick. A selected area electron diffraction pattern (SAEDP)

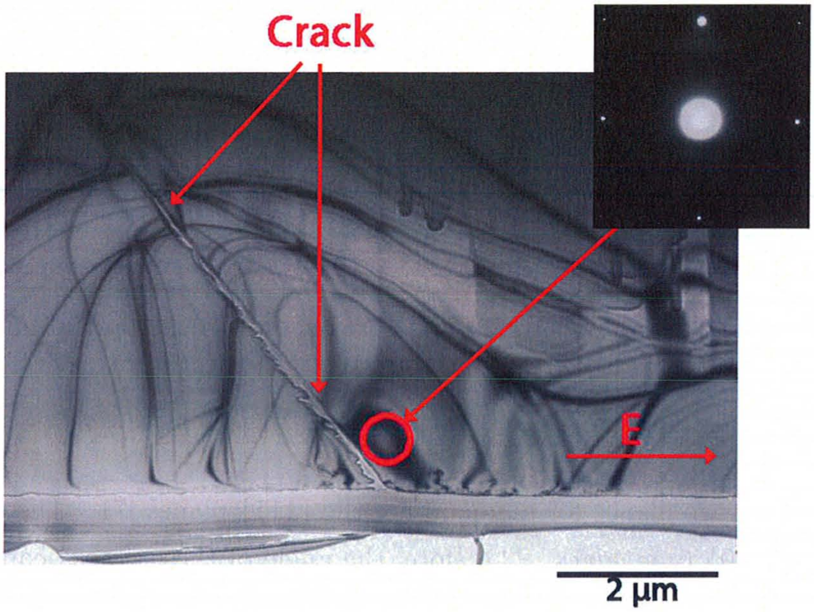

Figure 4.19: Bright field TEM image of a slice taken from an area irradiated to form a line in the bulk with 9.5 μJ pulses. Arrows point to the modified region or crack. The SAEDP shows the area around the crack appears crystalline.

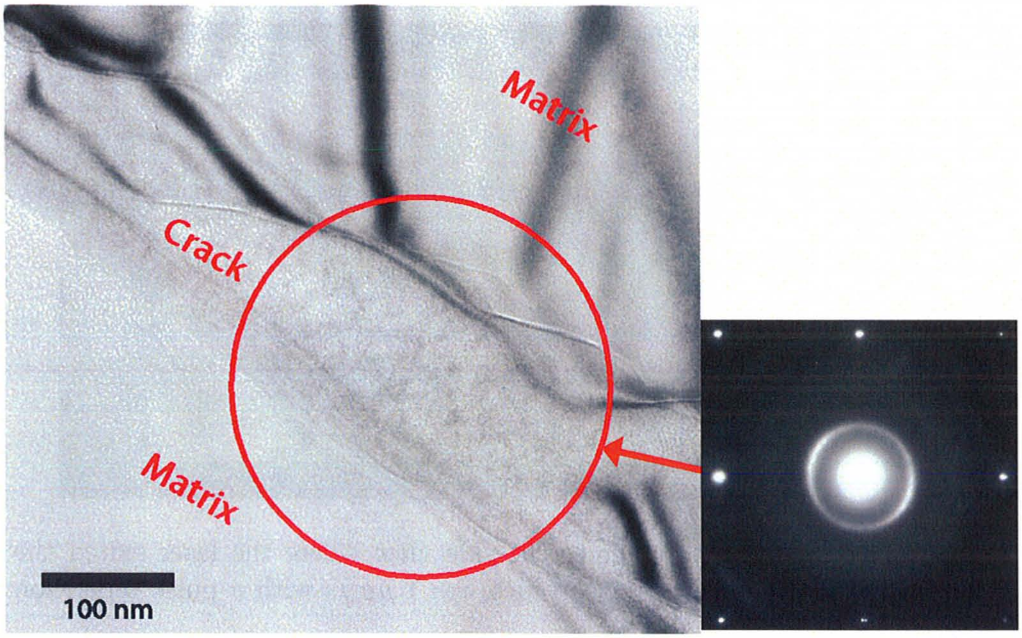

Figure 4.20: BF TEM image of the magnified crack region shown in Figure 4.19. The SAEDP was taken from the area pointed to by the arrow.

of the crack (Figure 4.20) displays spots which were present from the main matrix because the selected area aperture was too large to only sample the crack region. The very diffuse ring which is present and not seen in SAEDPs from outside the crack region indicates that the area inside the crack contains polycrystalline material with a very small grain size.

The experiment was repeated using higher energy pulses (up to 40 μJ instead of 10.2 μJ) and a much slower scan rate (1 μm/s as opposed to 500 μm/s) to explore more irradiation parameters. Changing both these parameters greatly increased the overall fluence and could help in the production of periodic bulk structures. The same 50x microscope objective was also used to tightly focus the laser beam 250 μm below the surface of the single crystal CVD diamond plate. The initial observations are shown in Figure 4.21. At the higher pulse energies, the laser modified the surface of the diamond plate and created deep trenches ($\sim$200 μm) into the sample. The modified area was not as deep below the surface as expected. Most of the modification occurred 150-200 μm below the surface even though the pulses were supposed to be focused

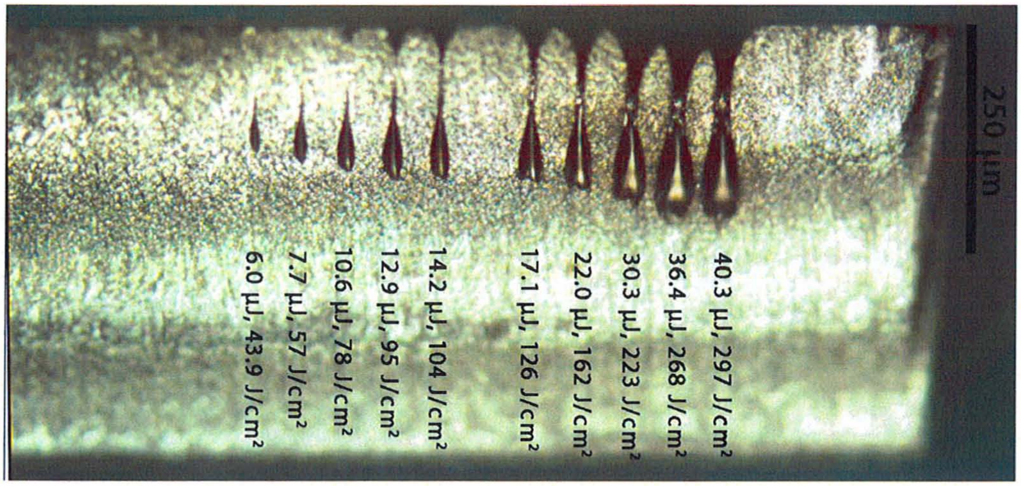

Figure 4.21: Optical microscope image of the side view where the laser exited the diamond plate from in the bulk. The scan rate was 1 μm/s with a pulse repetition rate of 1 kHz.

250 μm below the surface. Figure 4.22 shows an SEM image of the ten lines made with the highest pulse energies from Figure 4.21. At pulse energies below 6 μJ, no modification to the diamond by the laser pulses exiting through the surface could be observed in the optical microscope or SEM.

A TEM slice was made of the area irradiated with 7.7 μJ pulses. The thin slice was removed from the area marked in Figure 4.23. A magnified image of the region from which the TEM slice was taken is also shown in Figure 4.24. The most interesting feature is the needle-like structures present on the surface where the laser exited the sample. These structures exist over the entire modified region on the surface and are present for all the pulse energies labelled in Figure 4.22. The formation of these structures could be from laser pulses irradiating the sample as the focus area passed outside the diamond plate. These pulses would not have travelled through the bulk diamond and it would be more like a surface irradiation experiment with a glancing incidence angle ($\theta = 90°$).

Figure 4.25 shows the TEM section taken from the area marked in Figure 4.23. As with all of the TEM samples prepared in the FIB, the top light layer is a protective layer of carbon followed by a much darker layer of platinum. The spikes correspond

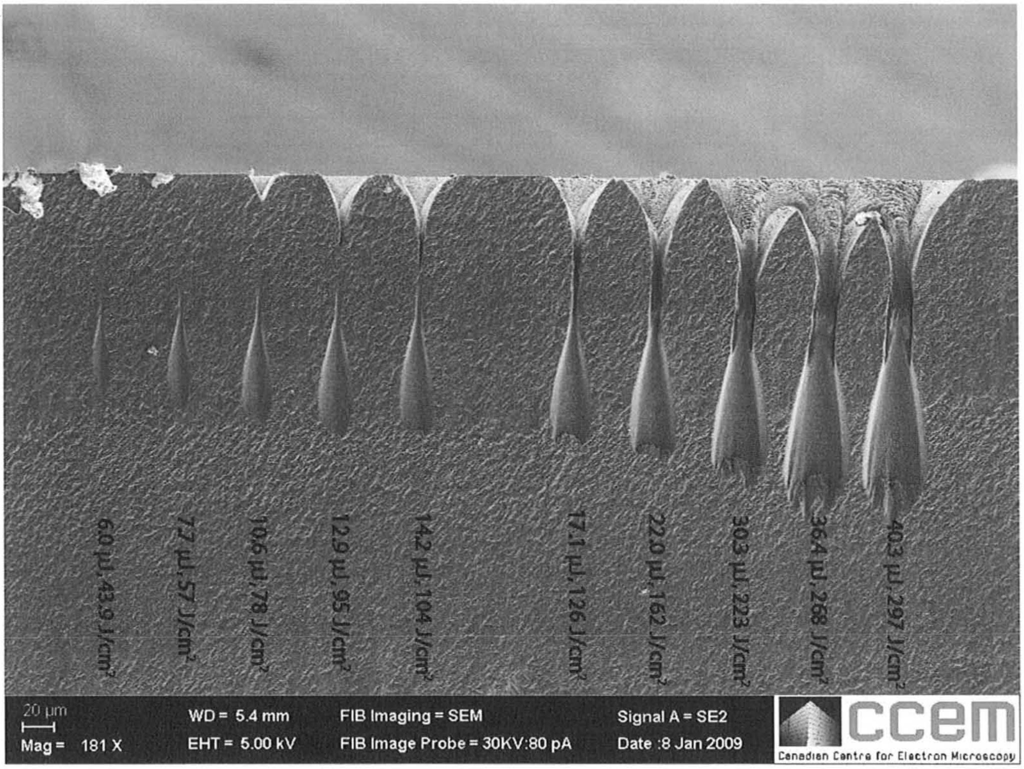

Figure 4.22: SEM image of same area shown in the optical microscope image from Figure 4.21.

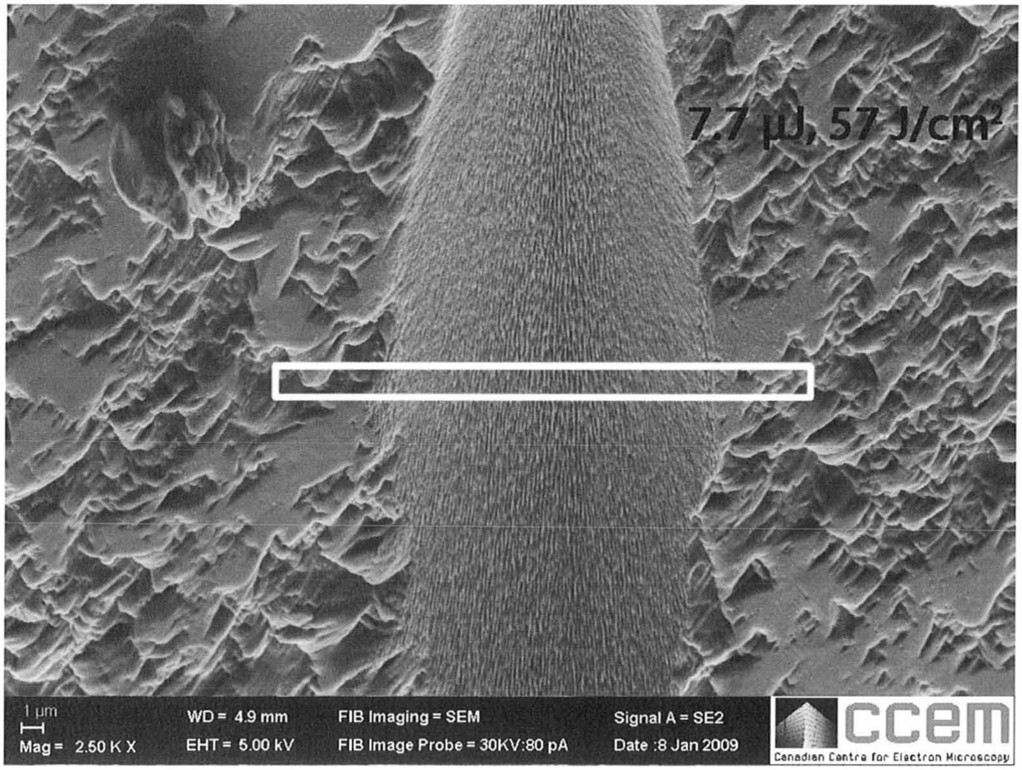

Figure 4.23: SEM image of where the line made using 7.7 μJ pulses exited through the side of the diamond plate. A TEM slice was taken in the area marked by the white rectangle.

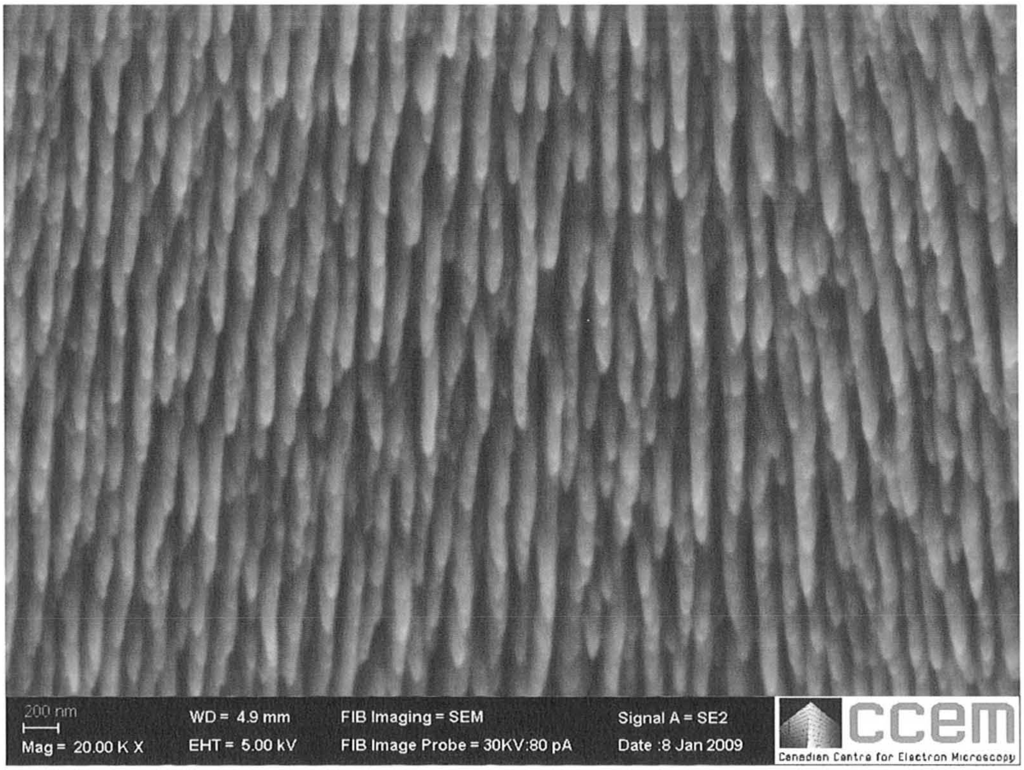

Figure 4.24: Magnified SEM image of the area around the white rectangle from Figure 4.23.

to the actual surface and the structures which appeared as needles in a SEM. The period of these structures as seen in the cross section is ~140 nm. The area underneath these spikes is single crystal and no modification caused by laser pulses is present. The only features present are bend contours and dark spherical structures believed to be artifacts from Ga ions during the milling process. To further confirm this, an EDS map was made of these spherical structures and the results are shown in Figure 4.27. The mapping was for the Kα_1 line of Ga, which has an energy peak of 9.2 keV. Lighter areas in Figure 4.27b correspond to higher Ga concentrations. The lines of spherical structures appear lighter and therefore have higher Ga concentrations. Also, the scanning transmission electron microscope (STEM) image (Figure 4.27a) shows these structures as appearing darker where there is more deflection of the electron beam by heavier Ga atoms.

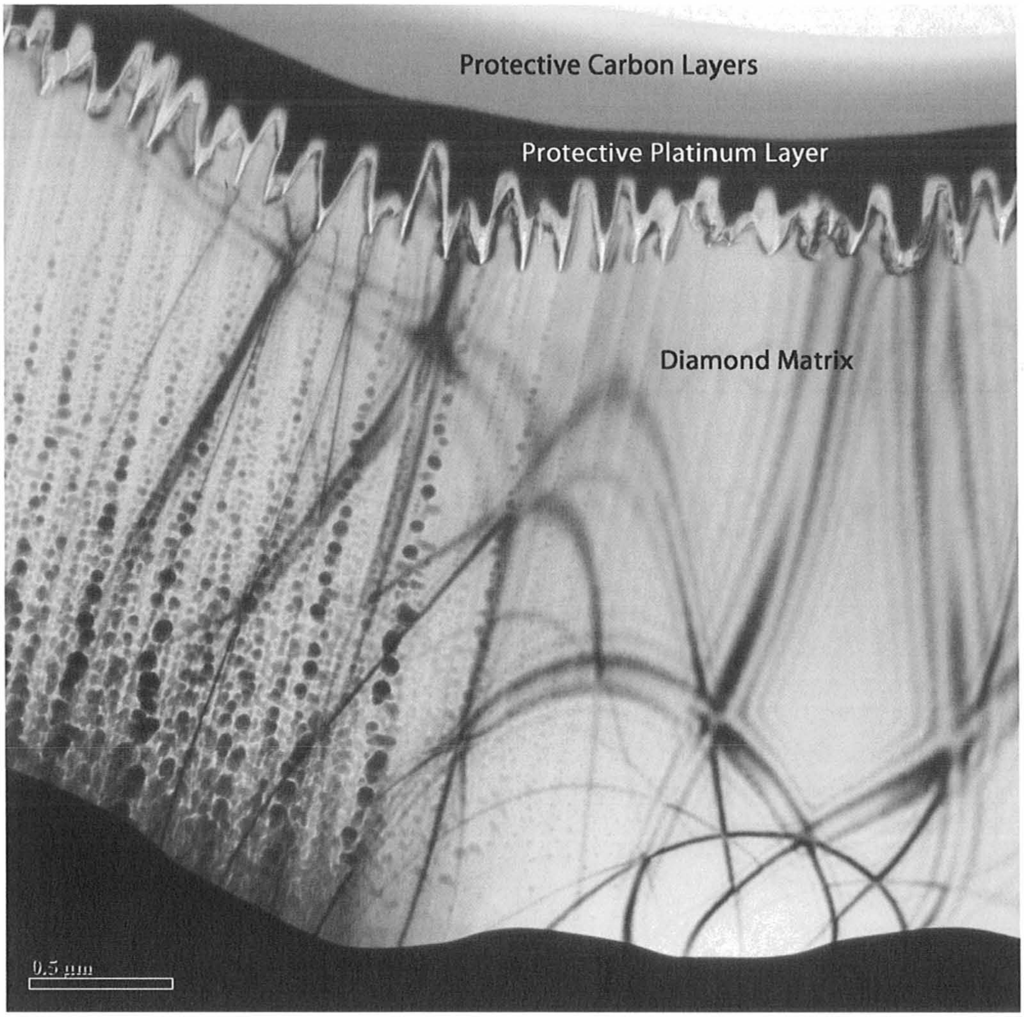

Figure 4.25: Bright field TEM image of the section taken from the area marked by the white rectangle in Figure 4.23.

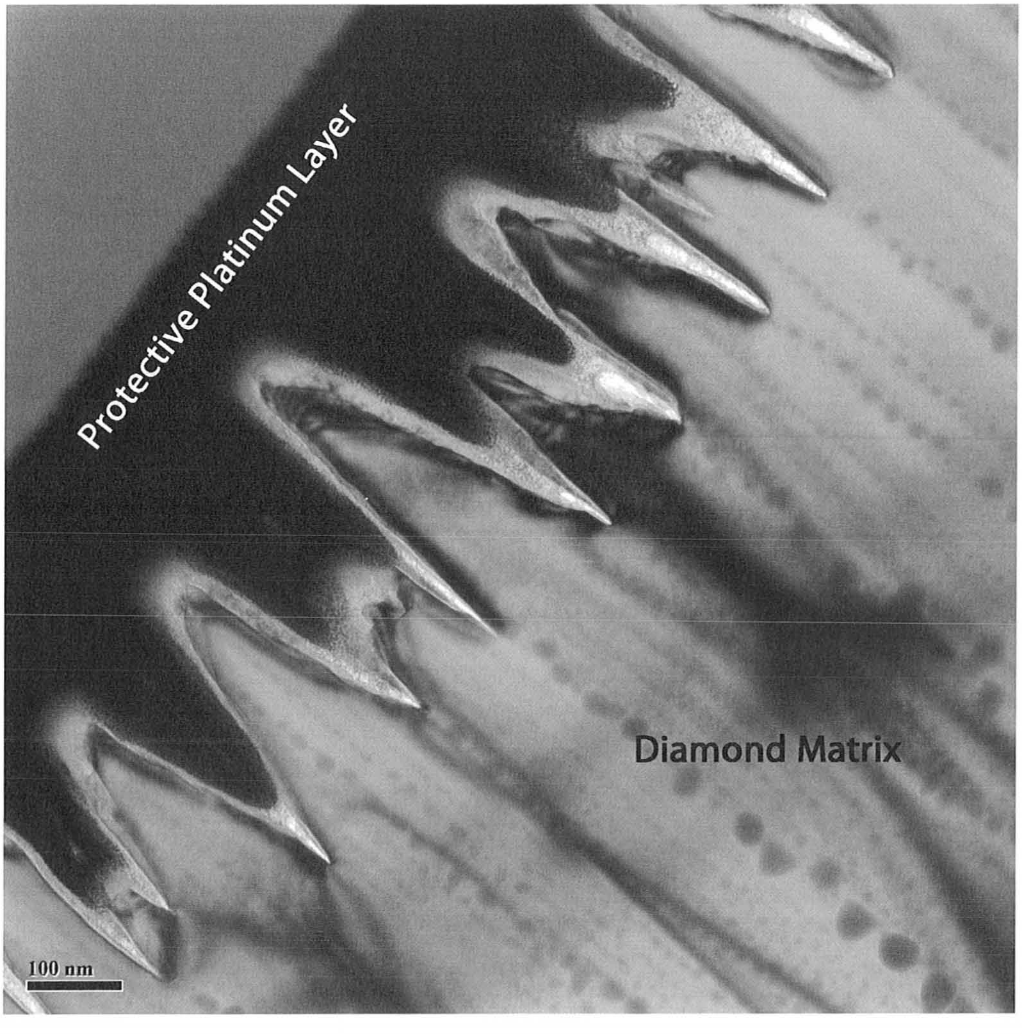

Figure 4.26: Magnified TEM image of the surface "spikes" seen in Figure 4.25. The spikes appear to be covered in a very thin (<10 nm) laser modified surface layer.

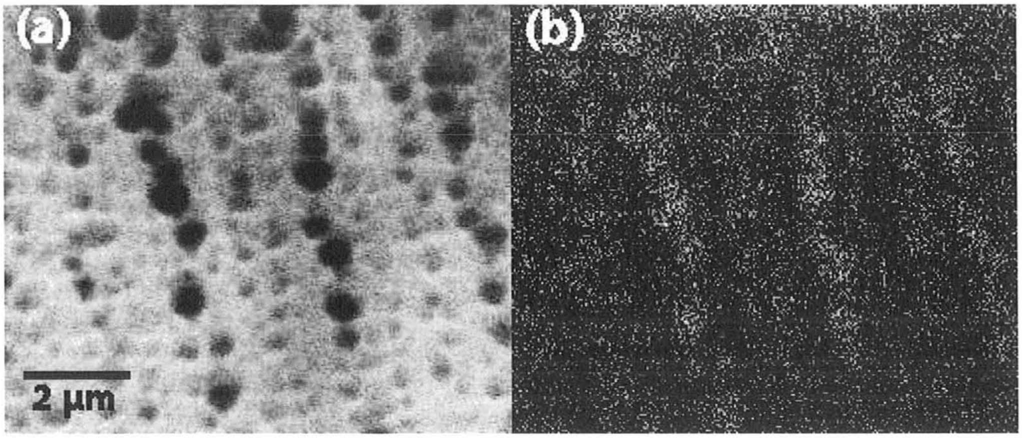

Figure 4.27: (a) STEM image of the region where the spherical structures are present. (b) the corresponding EDS map for Ga using the Kα_1 line of Ga.

To further study the possible formation of periodic structures in the bulk, another experiment was performed using the configuration shown in Figure 4.28 to irradiate down though the edge of the sample and come out through one of the polished faces. The sample was also kept at an angle of ~ 5° to reduce the amount of irradiation which only traveled through air and irradiated the side of the sample. This configuration should make it easier to see modifications in the bulk as the laser is now exiting through a polished surface. Figure 4.29a shows the results after bulk irradiation. The optical microscope image was taken by illuminating the sample from the bottom to observe the transmitted light.

The teardrop shapes seen for each line are very similar to the features seen in the two previous experiments. However, one difference which can be seen was lines which extend up to 200 μm below the teardrop shape. These lines were only visible when observing the sample with transmitted light and therefore do not appear to be surface features. Figure 4.29b is a magnified image of the area pointed to by the arrow. It shows these lines appear to have no defined periodicity. The lines also form a herring-bone pattern where smaller lines extend out from the central line at a downward angle of approximately 45°.

Figure 4.30 is an SEM image of the bottom of the teardrop feature made using 12.3 μJ pulses. The arrows point to the lines of cracks corresponding to the dark

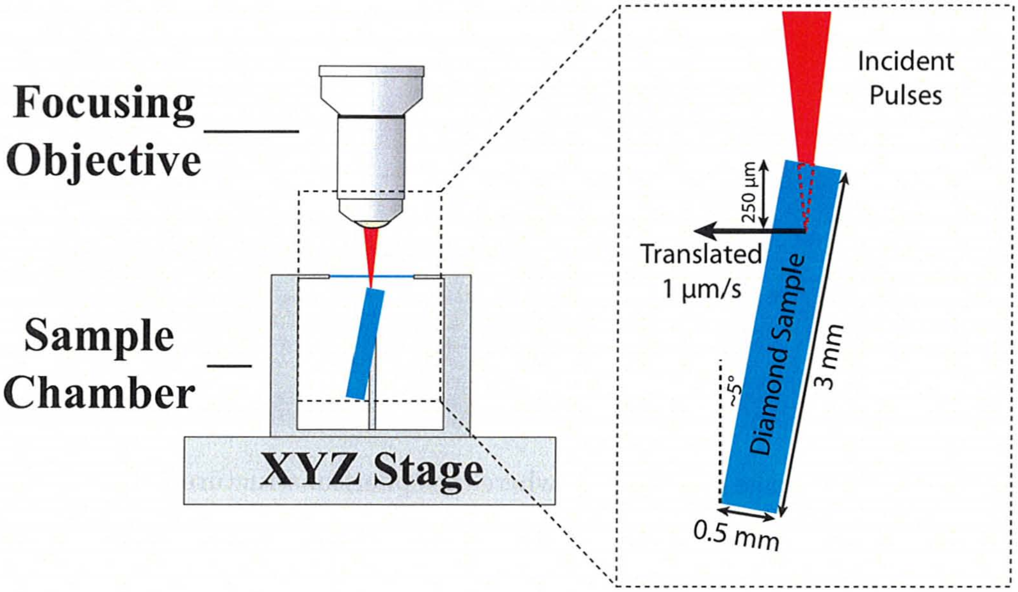

Figure 4.28: Configuration of the femtosecond laser machining setup to form lines in the bulk diamond plate which exit through the polished face. The image is not drawn to scale.

lines seen below the main tear drop shape in the optical microscope image from Figure 4.29. The cracks appear to be at an angle consistent with the {111} type planes as seen with previous cracking which leads to the herring-bone type pattern. The main teardrop formation has a periodic roughening on the surface that could be classified as LIPSS. The TEM sample made using a FIB out of the area marked by the white rectangle in Figure 4.30 was of very poor quality. Also, the only changes which were noticeable were cracks similar to the one seen in Figure 4.25. There was also a lot of re-deposition on the TEM sample from the Ga ion beam.

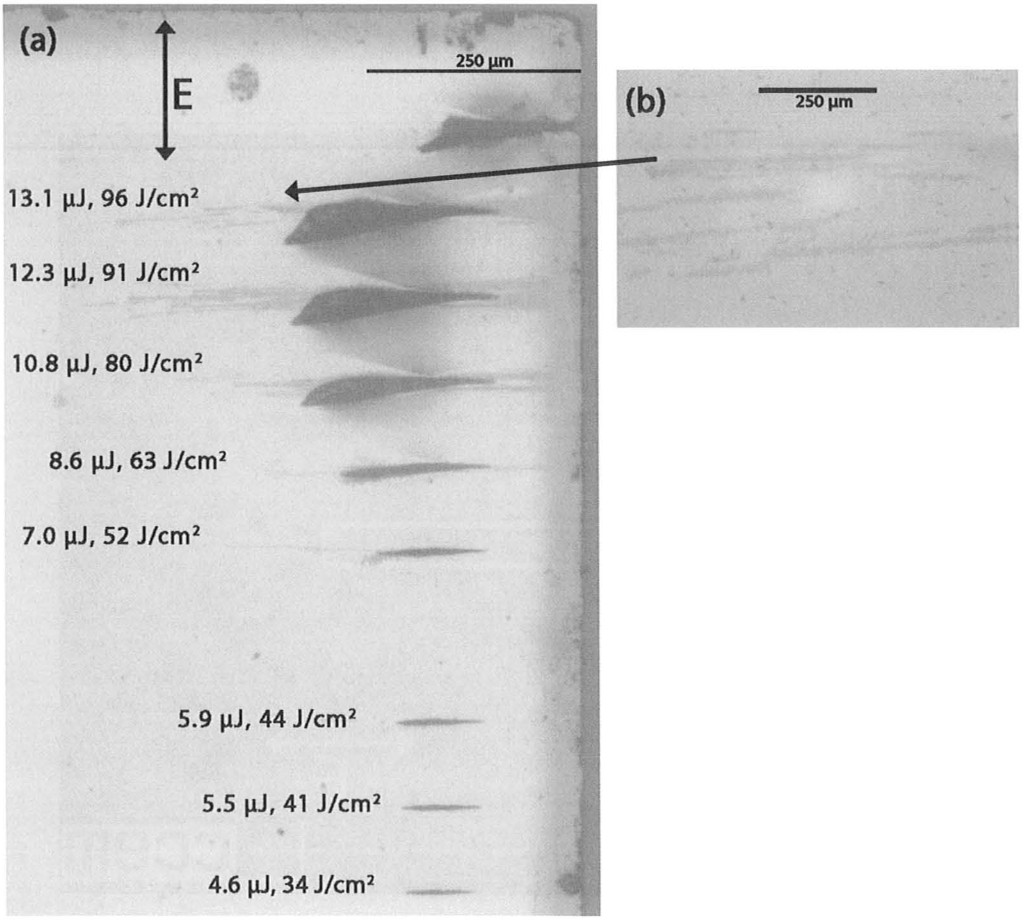

Figure 4.29: (a) Optical microscope image of the polished face where the laser pulses exited through the surface. The pulse energies for each line are shown. The sample was translated at 1 μm/s and the pulse repetition rate was 1 kHz. The top teardrop shape was a line made on the surface to track the location of the subsurface lines. (b) magnified image of the area marked by the arrow.

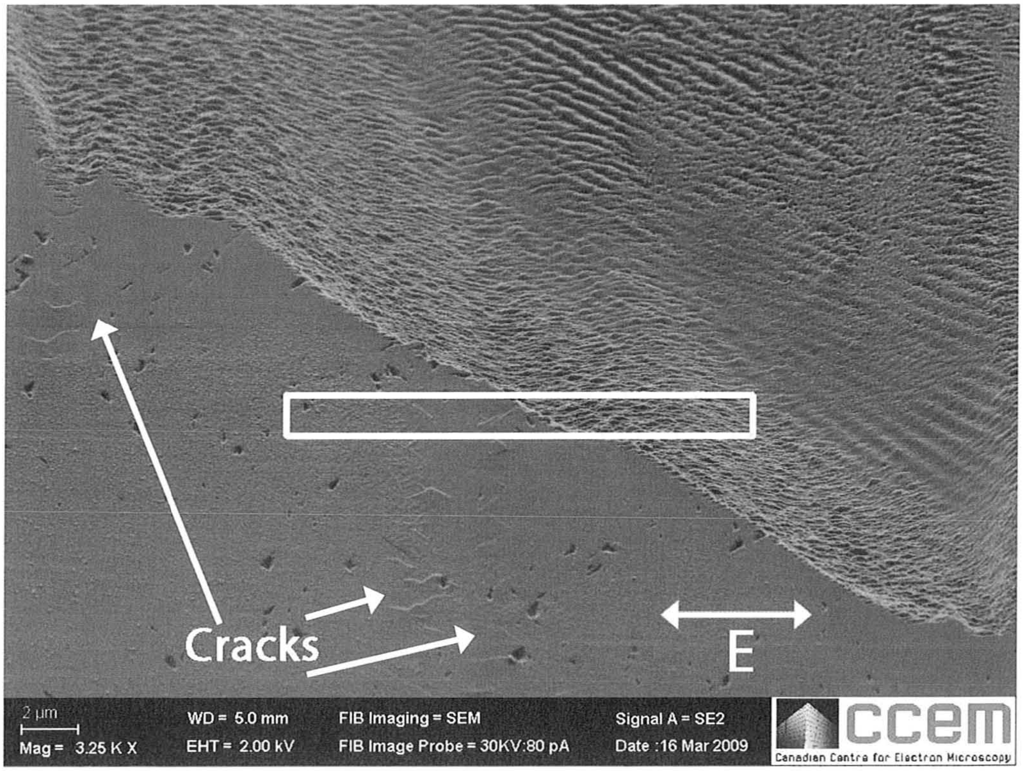

Figure 4.30: SEM image of the bottom of the teardrop formed when the line made in the bulk using 12.3 μJ pulses exited through the polished surface. The FIB section was made in the area marked by the white rectangle.

4.5.4 Discussion

Laser induced periodic structures in bulk diamond were not observed. It is possible that periodic structures did form inside bulk diamond. However, these structures may have been overlooked because a FIB can only sample a small area when making a TEM specimen. It is also possible that the modifications to the diamond lattice may not be detectable in a TEM. The proper experimental conditions (pulse energy, scan speed, intensity) may not have been used to produce periodic structures. Laser induced periodic structures may also be unable to form inside bulk diamond at any irradiation conditions for fundamental reasons.

The laser pulses were focused into the diamond samples taking an index of refraction for diamond of $\sim$2.5 into account. If the pulses were originally focused on the surface, translating the sample 100 μm in the z direction should then be approximately equivalent to focusing the pulses 250 μm into the bulk. Modifications seen on the surface may have appeared closer to the top face of the diamond plate than bulk modifications because parts of the pulse would have focused through air onto the sides of the diamond specimen. The modification seen on the side of the sample was used as a guide to select an area to make bulk TEM samples. Therefore, the wrong areas may have been selected to study bulk modification. However, the areas selected to make TEM samples were chosen carefully and in general as close to 250 μm beneath the surface as possible if modification was seen at that particular depth with the optical microscope. Nonlinear effects, such as self-focusing, could also focus the pulses closer to the surface in the bulk. These effects were also considered when selecting an area to make a TEM sample.

Modification to the bulk diamond may not have been detectable by studying the samples in a TEM. Very subtle changes to the crystal structure would not be detectable because of the poor quality of the TEM samples made using a FIB. These samples did not allow for high resolution imaging. For instance, the formation of color centers from atomic displacements or modification localized to a few nanometers in size could go unnoticed. The nanoplanes observed in fused silica required etching to reveal the planes in a SEM. The planes etched at a much faster rate which was believed to be caused by changes in the dielectric structure and possibly dislocations. It is not clear if these planes would be visible in a TEM section made using a FIB machine [6].

Finally, it may be possible that no periodic structures form for any irradiation condition in the diamond lattice and the dark areas seen in the optical microscope images are only from the cracks that form along cleavage planes. It is difficult for diamond to break down into other forms of carbon such as graphite. The density of diamond is about 3.5 g/cm^3 as compared to graphite which ranges from 1.8 – 2.25 g/cm^3 [72]. Therefore, the activation energy for graphite formation will be significantly less on the surface compared to the bulk, where the expansion required to form graphite will create large internal pressures. The reverse process may even occur where graphite is transformed back into diamond. Strekalov *et al.* found that a sphere of graphite growing from single crystal diamond in the bulk would lead to cracking of the crystal from mechanical stress when the sphere reached a radius of 2.3 nm [73]. Therefore, any modification to the diamond structure in the bulk may just lead to the formation of cracks in the single crystal lattice.

The grooves observed by Shinoda *et al.* [65] that were 40 nm wide but up to 500 nm deep were proposed to form by a mechanism similar to the one presented by Corkum *et al.* for the formation of the 20 nm wide planes in fused silica [6]. This theory has also been considered for other high aspect ratio features which have been observed through cross sections of surface features such as gallium phosphide [74]. Planes may form down into the bulk from the surface of diamond more readily because of the density, pressure, and energy considerations described above. Formation of planes from directly in the bulk, as was done with fused silica, may not be possible [6]. The "spikes" seen when lines made in the bulk exit through the surface (Figure 4.25) are the only features observed which have this high width to depth aspect ratio. The "spikes" have a period of ~140 nm (close to the value of ~146 nm observed by Shinoda) and are up to 400 nm in depth. However, these features were only seen on the surface and appear to be caused by pulses irradiating the surface through air at a grazing incidence. These spikes also appear to form with no dependence on the laser polarization. A TEM slice taken perpendicular to the one shown in Figure 4.25

would probably show a similar profile for the spikes based on the surface topography of the spikes. The experiment that used the setup from Figure 4.28 to minimize the possibility of a grazing incidence pulses along the exit surface revealed none of these "spikes" on the surface.

CHAPTER 5

Conclusion

5.1 Summary

The formation of LIPSS on the surface of diamond has been extensively studied. LIPSS were observed with a spacing of 550-600 nm using 800 nm, ~150 fs laser pulses. Also, HSFL with a spacing of 200-250 nm were observed in regions which received a lower fluence/pulse. The exact mechanism for the formation of these LIPSS is unclear. The theories which adequately predict the periodicity of LIPSS made using longer pulse and continuous wave lasers cannot explain the spacings of LIPSS made with ultra-short laser pulses. A nonlinear Sipe theory presented by Bonse *et al.* [26] may provide the best explanation for the spacing of the LIPSS observed on diamond. This theory takes into account changes in the refractive index due to free carrier generation. It also attempts to explain why LSFL form in areas irradiated with a higher fluence and HSFL form in areas irradiated with a lower fluence.

Other important observations about these ripple structures came from cross sections taken with a FIB and viewed in a TEM. Both the HSFL and LSFL had a similar structure. The inside of the ripples was part of the main diamond matrix and appeared to be unmodified by the laser. Both the HSFL and LSFL were covered in a thin modified layer. The depth to width ratio of these ripples compared to LIPSS in the form of periodic grooves that has been observed on single crystal diamond irradiated with femtosecond laser pulses by some research groups [65, 66] is quite different. The ripples observed in this thesis had more of a sinusoidal profile.

The deep rings around a central protrusion observed on single pulse craters made with pulses with peak fluences above ~45 J/cm^2 revealed that a more complex physical process was occurring than would otherwise be expected when samples were irradiated with single, high intensity femtosecond laser pulses. It would have been expected that when a Gaussian profile pulse irradiates a surface, a crater forms which has a depth profile that is also similar to a Gaussian profile or is relatively flat as observed in some semiconductors craters made with single laser pulses [35]. However, more recent work by Bonse *et al.* [54] has also revealed this phenomena on InP where a central protrusion forms in the center of craters made with higher pulse fluences. Appendix A gives an analysis of a TEM cross section of one of these craters made by Bonse *et al.*

The bulk experiments on diamond did not produce the periodic structures which were expected. The only observed modification was cracks filled with polycrystalline and amorphous material. These cracks all formed along the cleavage plane for diamond.

5.2 Suggestions for Future Work

One of the main areas where there is a need for further work is improving the quality of the diamond TEM samples made using a FIB. Diamond was very prone to re-deposition where the material being removed by the ion beam as it scans across the sample is redeposited as an amorphous layer on the sample. This amorphous layer makes it impossible to do any high resolution imaging of the sample. An attempt was made to improve the quality of the diamond TEM samples by polishing the samples with a Technoorg Linda Gentle Mill. This machine uses low energy ions to polish and thin samples that were initially prepared in a FIB. However, the Gentle Mill was also prone to re-deposition. It may be possible to find the right parameters for the ion beam current and accelerating voltage in a FIB and Gentle Mill which minimizes this re-deposition.

Modeling the effects of spherical aberrations and possible stretching of the pulse because of self-phase-modulation as the pulse transverses through diamond could be performed. This modeling would improve knowledge of the pulse parameters used to irradiate the inside of diamond samples during bulk modification experiments. Accurately determining the Raleigh length of the laser pulse inside diamond and changes in the focus position because of self-focusing could also be studied. Knowledge about these parameters could be used to better explain the results of the bulk diamond experiments.

A variety of other experiments exploring different parameters for laser modification could be considered. One of the main areas of interest would be in studying irradiation with pulses that have a peak fluence around the threshold value. The high ratio HSFL or grooves observed on diamond were always produced using a high number of pulses at an energy near the threshold for ablation. The grooves produced by Huang *et al.* [66] were made on a laser system had pulse parameters (pulse duration, wavelength, and repetition rate) that were very similar to the parameters of the femtosecond laser system in the Photonics Research Lab at McMaster. It would be interesting to see if the laser system at McMaster could also produce these grooves.

Further TEM analysis on cross sections of single pulse craters at a variety of pulse energies could also be performed. The evolution of the central protrusion and the modified layer below the surface as the pulse energy is changed could give insight into the formation of the central protrusion. If the modified layer under the central protrusion were to extend deeper below the surface for lower pulse energies, it would give confirmation that the proposed mechanism for the formation of the central protrusion is correct. It would also be interesting to make TEM sections for a series of craters made with increasing numbers of pulses at the same pulse energy. These cross sections would give an overall picture for the formation of LIPSS. However, these experiments would be very time consuming because it takes up to twelve hours or more to make one TEM sample of diamond on a FIB.

Other surface experiments which could be performed on single crystal diamond include irradiating the surface at different incident angles. The "spikes" seen on the surface of one of the bulk experiments where the laser exited through the side of the sample (Figure 4.23) appeared to be more of a surface phenomena caused by pulses irradiating the surface at a grazing incidence. The effects of using p- or s-polarized pulses could also be studied.

Time resolved microscopy measurements similar to the ones performed by Bonse *et al.* using a weak probe pulse to measure the reflectivity of the surface after irradiation with the initial femtosecond laser pulse could prove interesting on diamond. These measurements are useful for studying the evolution of a highly excited sample surface after irradiation by a femtosecond laser pulse. These measurements give some insight into the evolution of the carrier density and the amount of time it takes for material to be ablated from the surface. Pump probe measurements using Terahertz radiation could also give some insight into the carrier lifetime of diamond. These measurements would be useful to determine if the pre- or post-pulses change the morphology of the craters because of incubation effects.

It is unclear if any bulk experiments could be performed to produce periodic structures inside diamond. However, it may be useful to look for periodic structures by other means besides using a FIB. Etching samples has been done to observe periodic structures inside fused silica [6]. This method may also reveal periodic structures inside diamond. Precise etch rates for diamond using HF or some other chemical would have to be determined.

TEM analysis on other materials already known to produce periodic structures in the bulk could be performed. Studying samples irradiated by a single pulse in the bulk at energies low enough so that multiple pulses are required to modify the sample could be interesting. The initial pulse is supposed to produce defects that seed the modification by subsequent pulses. TEM analysis of these defects would provide insight into the mechanism for the formation of periodic structures inside dielectrics using low energy, femtosecond laser pulses. The quality of the TEM samples would have to be much better than the current samples made for analysis in this thesis to observe these defects. Re-deposition is less of a concern in other materials and it may be possible to make higher quality TEM samples of these materials using a FIB and gentle mill.

Modeling the formation of single pulse craters could give a better understanding of the central protrusion that forms. This would require precise knowledge of the pulse fluence to compare the models with the experimental results. Precise knowledge of the absorption rates for diamond would also have to be determined to perform accurate simulations [75]. Molecular dynamics simulations looking at the ablation of a wide range of solids have been studied by [14, 15, 76, 77]. These simulations assume atoms act through a Lennard-Jones potential. Energy is first absorbed by electrons and then transferred to the lattice. Ablation models specific to dielectrics have also been performed by [9, 78]. Modeling the interaction of femtosecond laser pulses with dielectrics is more complex. Multi-photon ionization rates and the effects of impact ionization have to be taken into account when calculating the absorption of energy by electrons. These models would have to determine changes in the absorption cross section because of free electron generation. The energy absorption at different depths below the diamond sample surface could then be calculated. If energy was found to absorb preferentially on the surface for higher pulse fluences, this would confirm the mechanism proposed by Bonse *et al.* for the formation of a central protrusion in single pulse craters [54].

A model to describe the the spacing of LIPSS observed on diamond using a non-linear Sipe theory could also be studied. This model would have to take into account changes in the refractive index because of free electron concentrations. Changes in the efficacy factor for different pulse fluences because of free carrier generation could be calculated. These calculations along with the effects of SHG could be used to better understand why either LSFL or HSFL are more likely to form on the surface of diamond depending on the laser pulse fluence. One possible concern with these simulations would be the effects from surface defects and defects directly below the surface in the bulk such as dislocations and impurities. Laser radiation could be preferentially absorbed at these sites during experiments. Most models do not take these defects into account. However, the diamond samples used in this thesis had a high number of surface defects which should also be considered [79].

Other areas of interest include molecular dynamic simulations of material modification inside diamond when the volume is confined. The overall energy and pressures associated with possible modifications to the crystal lattice could be studied to determine if the only likely formations are the observed cracks in the bulk of diamond. The possibility of diamond reformation could also be addressed.

APPENDIX A

TEM Analysis of a Single Pulse InP Crater

Bonse *et al.* [54] irradiated single crystal indium phosphide wafers with 800 nm, 10 fs laser pulses at the Max-Born-Institut für Nichtlineare Optik und Kurzzeitspektroskopie in Berlin, Germany. In collaboration with Bonse *et al.*, a paper has been submitted that included a section on the results of TEM analysis performed at McMaster on one of these single pulse craters. The paper also included complimentary optical microscope images and AFM measurements obtained by Bonse *et al.* The results of the TEM analysis are presented in this appendix.

It was observed that a central protrusion formed inside single pulse craters made on InP when the peak fluence of the Gaussian profile pulse focused to a $1/e^2$ spot size diameter of ~50 μm, exceeded 0.78 J/cm^2. Figure A.1 is an AFM image of a pulse made with a peak fluence of 0.91 J/cm^2. As with diamond, the deepest areas of the single pulse crater are in an outer ring and not in the center of the crater. The crater shown in Figure A.1 is over 120 nm deep in this ring. In the center there is a sudden step-like increase of ~60 nm to central protrusion which is 15 μm wide. This central protrusion observed inside single pulse craters made on InP at pulse energies well above threshold has been previously observed [54, 80].

Figure A.2 is a bright field TEM image of a thin section made along the line of

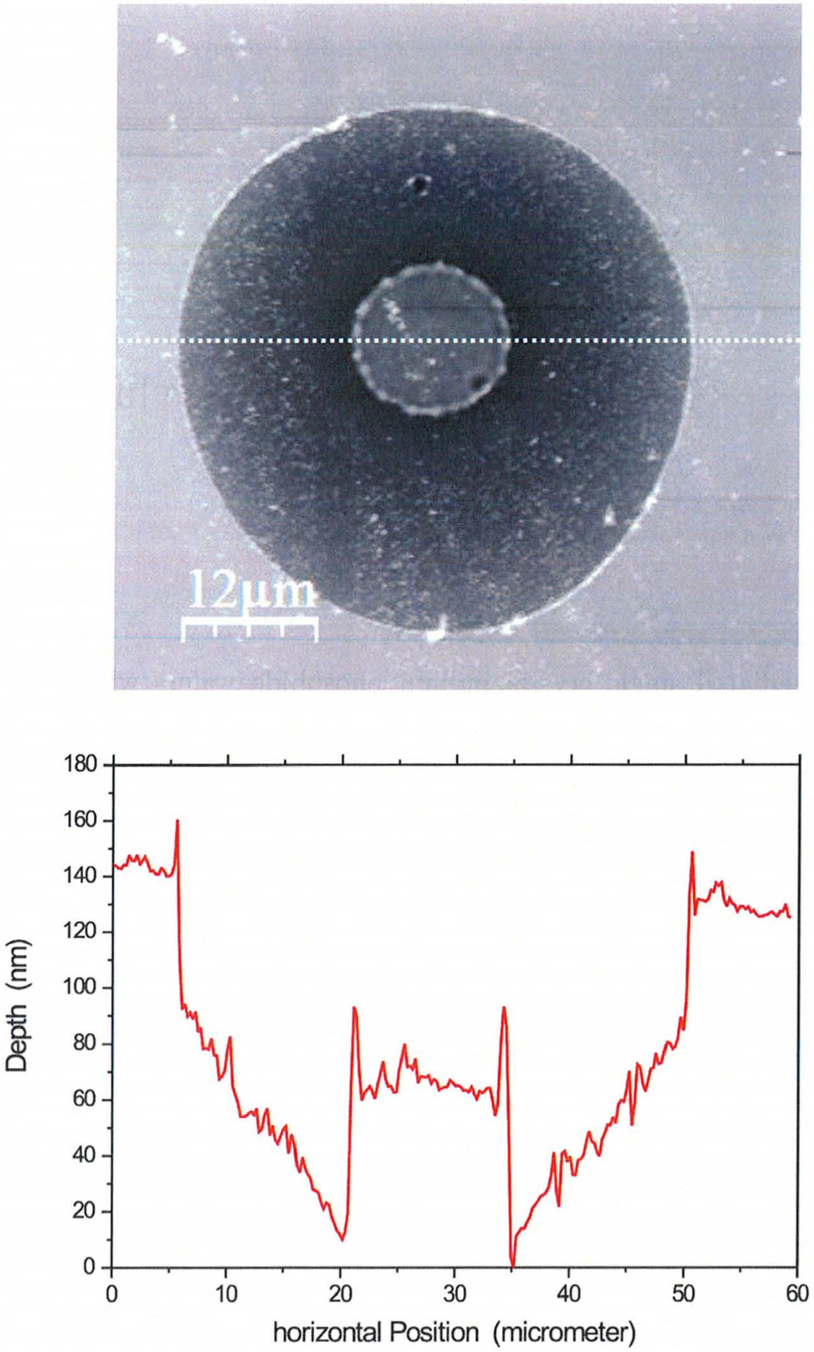

Figure A.1: AFM profile of a crater made with a single, 10 fs, 800 nm laser pulse. The pulse was focused to have a $1/e^2$ spot size diameter of ~ 50 μm and a peak fluence of 0.91 J/cm^2. The bottom graph is an AFM depth profile along the white line from the AFM image. This image was received from Bonse in private communications.

the crater shown in Figure A.1 using a FIB. The "protrusion edge" area in this image corresponds to the deepest part of the crater where the central protrusion begins. The "central protrusion" arrow points to an area of the TEM sample corresponding to the central region of the crater. A magnified image of the edge area is shown in Figure A.3. The modified layer directly below the carbon layer is 60 nm to 200 nm thick. The thickest part of this layer is at the central protrusion edge. There is a very sharp boundary between this layer and the unmodified layer. Also, the interface between the modified layer and InP matrix does not follow the same profile as the surface. This interface remains relatively flat even at the boundary to the central protrusion.

It is believed the interface between the modified and unmodified InP was relatively flat because the initial part of the pulse was absorbed into the material at some characteristic optical penetration depth. This characteristic depth created a modified layer with a uniform depth that did not follow a Gaussian profile. The central protrusion was then created when the center of the Gaussian profile laser pulse caused a highly excited electron plasma surface layer to form in the center of the area being irradiated. This highly excited layer was believed to absorb most of the energy from the center of the pulse before being ejected from the surface. In areas farther from the center of the crater energy was absorbed deeper into the InP and more ablation occurred because there was no highly excited electron plasma layer at the surface to absorb most of the laser radiation. Other observations also support this proposed mechanism. At lower laser pulse energies, craters were formed on InP with a relatively flat depth profile. These flat craters appeared to form because the energy was absorbed in a uniform layer determined by an optical penetration depth. However, no highly absorbing free electron surface layer was created in the center of these craters made with laser pulses that had a lower peak fluence. The energy from the laser pulse was then absorbed to a more uniform depth and the amount of ablation across the crater was more even.

Selected area electron diffractions patterns (SAEDPs) were taken to determine the material structure of the modified surface layer. The smallest aperture available on the CM12 microscope was still too large to only sample the modified area. In-

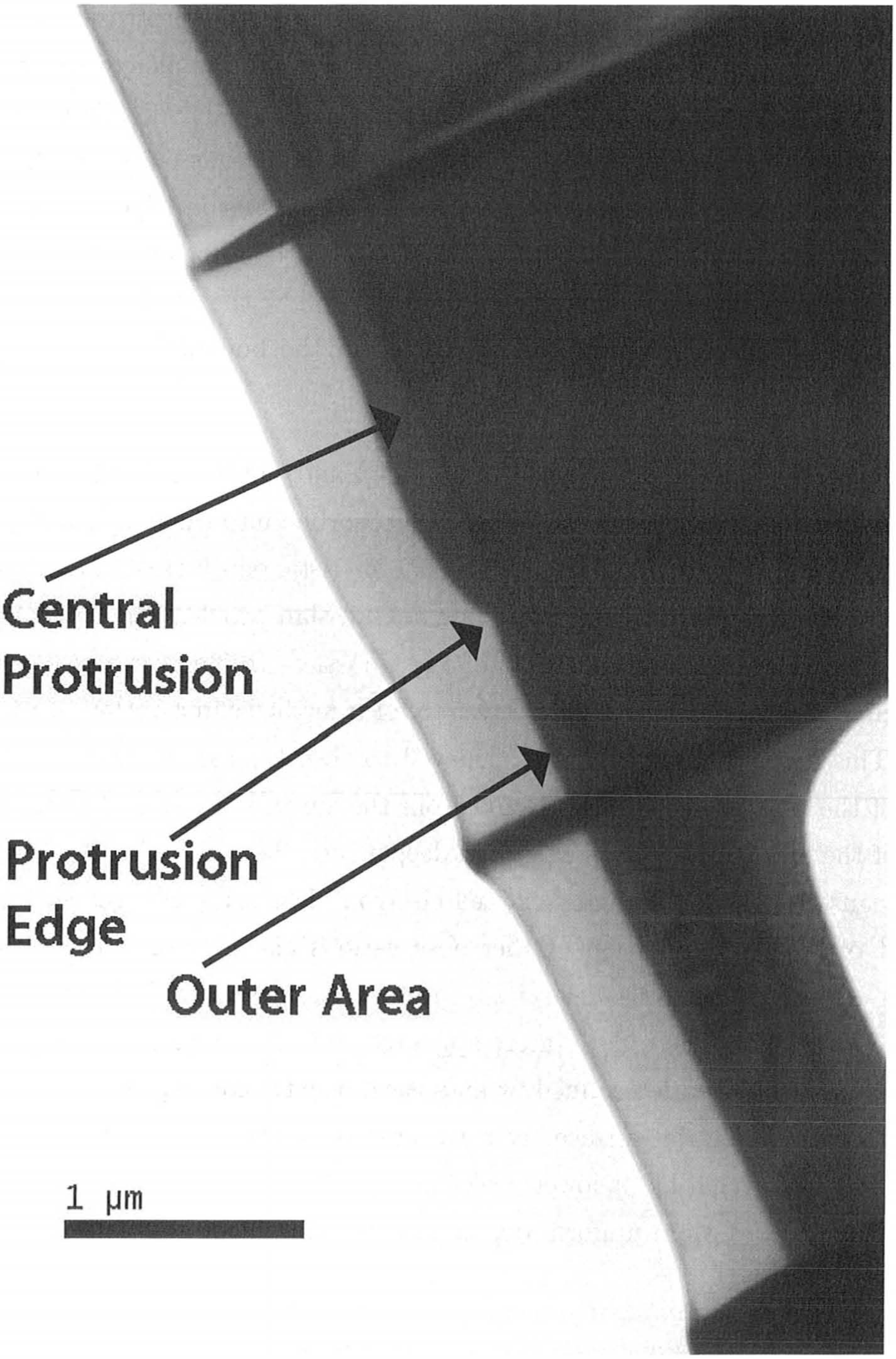

Figure A.2: Bright field TEM image of a thin cross section made with a FIB along the dashed white line from the 0.91 J/cm^2 crater shown in Figure A.1.

stead, multiple SAEDPs were taken. The circles in Figure A.3 show the areas the two SAEDPs, labelled SAEDP1 and SAEDP2, were taken. SAEDP1 sampled the modified layer and the main crystal matrix. The diffraction pattern contains both rings from polycrystalline material and brighter spots from the InP matrix. SAEDP2 sampled the area inside the central protrusion and the amorphous carbon layer used to protect the sample surface. This diffraction pattern contained both rings, due to polycrystalline material, and a diffuse background from amorphous material. These diffraction patterns indicate the modified layer is made up of polycrystalline InP. It is also possible that some amorphous InP is also present. The rings present in both diffraction patterns are diffuse and indicate the polycrystalline material is made up of small grains.

To better determine the grain size, dark field TEM images were taken of the laser modified layer. Dark field TEM images are formed in a similar way to bright field TEM images. Both types of images require an objective aperture to be placed at the back focal plane of the objective lens. However, in a bright field TEM image the objective aperture is placed so that only electrons that did not undergo diffraction are allowed to pass through the microscope and form an image. Areas which diffract more electrons will appear darker. A dark field TEM image is formed by moving the aperture out to one of the diffracted spots, or in this case one of the rings, to form an image from the diffracted electrons. This will create more contrast between different grains because the orientation of a particular grain with respect to the incident electron beam will determine how many electrons are diffracted into the objective aperture. Grains oriented to have diffraction spots on the area of the ring selected by the objective aperture to form the image will appear the brightest.

The dark field TEM images are shown in Figure A.4. Figure A.4b is a collage of several dark field TEM images in the same area the bright field TEM images were taken in Figure A.2. The uniform bottom layer that appears very dark in all the images from Figure A.4 is the unmodified InP matrix. Above this dark region the speckled layer is the laser modified region. The speckle pattern is caused by the polycrystalline material and the random orientation of the grains as previously described. The very bright spots correspond to grains with an orientation that strongly

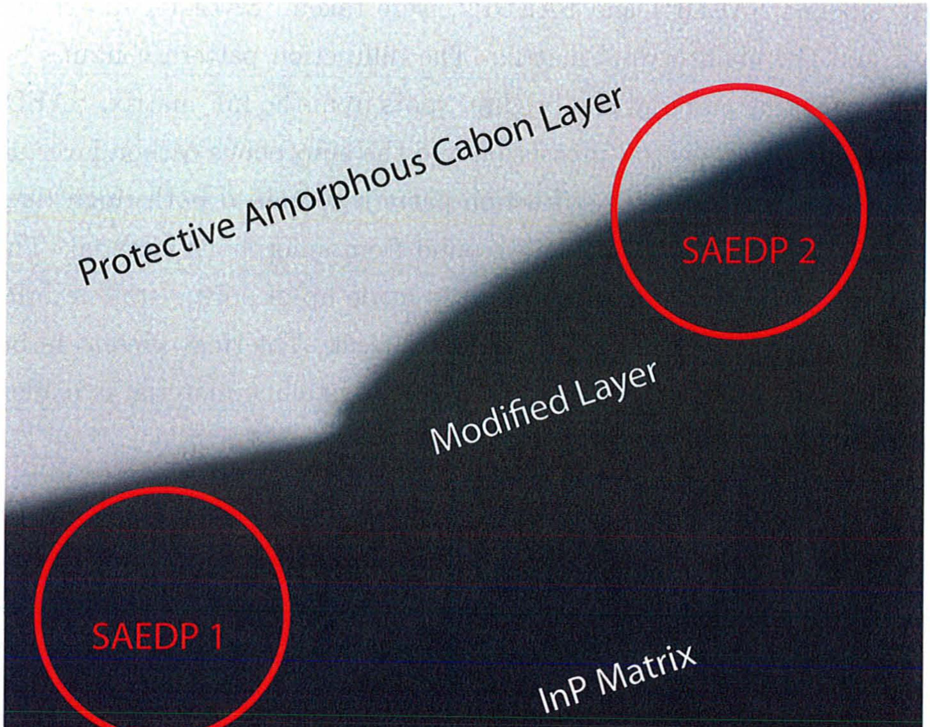

Figure A.3: Bright field TEM image of the edge area from Figure A.2. Diffraction patterns of the modified area are also shown.

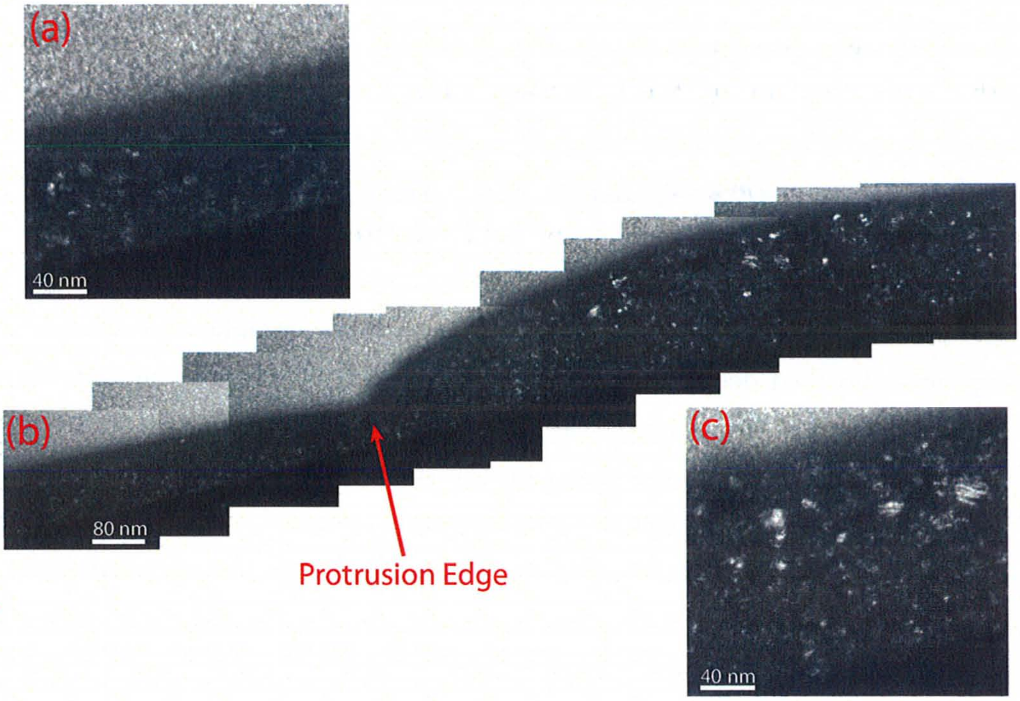

Figure A.4: Dark field images of the laser modified layer. (b) is a mosaic of dark field images taken at the edge of the central protrusion. (a) and (c) are magnified images of the modified layer outside and inside the central protrusion respectively.

diffracted electrons into the objective aperture. Figure A.4a is a magnified dark field image from the modified layer outside the central protrusion. Figure A.4c is a magnified dark field image from the modified layer inside the central protrusion. From the speckle pattern it can be seen that the polycrystalline layer inside the central protrusion is made up of larger grains (~10-15 nm wide) compared to the polycrystalline layer outside the central protrusion that is made of grains ~5-10 nm in size. Some of the bright grains in Figure A.4c also appear as stripes. These stripes could be due to twinning of the grains.

The same mechanism responsible for the formation of the central protrusion in single pulse InP craters is believed to be responsible for the central protrusion observed in single pulse diamond craters. However, TEM cross sections of the central protrusion observed in InP single pulse craters appears quite different from TEM cross sections of the central protrusion observed in diamond single pulse craters. The laser modified area in diamond was much thinner inside the protrusion and the thickest part was underneath the deep rim. In InP this layer was thickest inside the central protrusion. The interface between the modified layer and unmodified matrix in the diamond crater also followed the surface topography more closely than the interface in InP which was relatively flat. One possible explanation is although energy was initially absorbed into diamond at some characteristic optical penetration depth diamond is not as easily modified as InP. Therefore, in the center of the diamond crater although some energy was absorbed deeper into the matrix it was not enough to modify the material. A highly excited surface of free electrons was then generated which absorbed all of the energy in the center of the crater on the surface. There may also be less efficient absorption below this surface layer in diamond compared to semiconductors such as InP. The surface layer will attenuate the laser pulse. Lower intensity radiation will then propagate below the surface. A higher intensity is required for absorption of infrared photons in dielectric diamond compared to InP (E_g=1.27 eV) which can absorb single 800 nm photons as opposed to requiring multi-photon processes for absorption.

The different properties of the laser pulses used to make the craters should also be considered when comparing the diamond and InP craters. Bonse *et al.* used a pulse with a spot size of 25 μm as opposed to the 5 μm spot size used for surface experiments in this thesis. The larger spot size would have the effect of making the crater depth more uniform over a given surface area. Also, Bonse used 10 fs laser pulses which would be more intense than the 150 fs laser pulses used in this thesis that still have the same fluence. The surface experiments performed by Bonse *et al.* were also performed in air (~760 Torr) as opposed to the surface experiments performed in this thesis which were all performed in vacuum at ~0.04 Torr. It has been suggested by N.M. Bulgakova that a plasma could form in air above the sample surface and consume part of the pulse energy. This plasma would form preferentially in the center of the pulse where the intensity is highest. It would reduce the energy that reaches the sample in the center of the pulse. This effect could also help produce the central protrusion observed on InP. However, it is less likely to be a factor in diamond because the experiments were performed in vacuum. A simulation of plasma formation in air caused by optical breakdown could also be performed to determine the effects of this plasma. Accurate values for the Rayleigh length of the focused laser pulse would have to be known.

BIBLIOGRAPHY

[1] C Rullière, editor. *Femtosecond Laser Pulses: Principles and Experiments.* Springer-Verlag Inc., New York, 1998.

[2] T. Maiman. Stimulated optical radiation in ruby. *Nature*, 187(4736):493–494, 1960.

[3] W Ashcroft and N Mermin. *Solid State Physics.* Thompson Learning, Toronto, 1976.

[4] D Bäuerle. *Laser Processing and Chemistry.* Springer-Verlag Inc., Berlin, 2000.

[5] M. Birnbaum. Semiconductor surface damage produced by ruby lasers. *J. Appl. Phys.*, 36(11):3688–3689, 1965.

[6] V. Bhardwaj, E. Simova, P. Rajeev, C. Hnatovsky, R. Taylor, D. Rayner, and P. Corkum. Optically produced arrays of planar nanostructures inside fused silica. *Phys. Rev. Lett.*, 96(5):057404–4, 2006.

[7] B. Rethfeld, K. Sokolowski-Tinten, D. von der Linde, and S. I. Anisimov. Timescales in the response of materials to femtosecond laser excitation. *Appl. Phys. A*, 79(4):767–769, 2004.

[8] N. Bloembergen. Role of cracks, pores, and absorbing inclusions on laser induced damage threshold at surface of transparent dielectrics. *Appl. Opt.*, 12(4):661, 1973.

[9] B. Rethfeld. Free-electron generation in laser-irradiated dielectrics. *Contrib. Plasma Phys.*, 47(4-5):360–367, 2007.

[10] B. Rethfeld, K. Sokolowski-Tinten, D. von der Linde, and S. I. Anisimov. Ultrafast thermal melting of laser-excited solids by homogeneous nucleation. *Phys. Rev. B*, 65(9):092103, 2002.

[11] P. Bucksbaum and J. Bokor. Rapid melting and regrowth velocities in silicon heated by ultraviolet picosecond laser pulses. *Phys. Rev. Lett.*, 53(2):182, 1984.

[12] B. Chichkov, C. Momma, S. Nolte, F. von Alvensleben, and A. Tünnermann. Femtosecond, picosecond and nanosecond laser ablation of solids. *Appl. Phys. A*, 63(2):109–115, 1996.

[13] Y. Yao, H. Chen, and W. Zhang. Time scale effects in laser material removal: a review. *Int. J. Adv. Manuf. Technol.*, 26(5):598–608, 2005.

[14] D. Perez and L. Lewis. Ablation of solids under femtosecond laser pulses. *Phys. Rev. Lett.*, 89(25):255504, 2002.

[15] D. Perez and L. Lewis. Molecular-dynamics study of ablation of solids under femtosecond laser pulses. *Phys. Rev. B*, 67(18):184102, 2003.

[16] V. Mijoule, L. J. Lewis, and M. Meunier. Coulomb explosion induced by intense ultrashort laser pulses in two-dimensional clusters. *Phys. Rev. A*, 73(3):033203, 2006.

[17] R. Stoian, D. Ashkenasi, A. Rosenfeld, and E. E. B. Campbell. Coulomb explosion in ultrashort pulsed laser ablation of Al_2O_3. *Phys. Rev. B*, 62(19):13167–13173, 2000.

[18] Y. Dong and P. Molian. Coulomb explosion-induced formation of highly oriented nanoparticles on thin films of 3C-SiC by the femtosecond pulsed laser. *Appl. Phys. Lett.*, 84(1):10–12, 2004.

[19] D. Emmony, R. Howson, and L. Willis. Laser mirror damage in germanium at 10.6 μm. *Appl. Phys. Lett.*, 23(11):598–600, 1973.

[20] C. Walters. Surface scattering at LSD-wave initiation sites on nonmetallic materials. *Appl. Phys. Lett.*, 25(12):696–698, 1974.

[21] P. Temple and M. Soileau. Polarization charge model for laser-induced ripple patterns in dielectric materials. *IEEE J. Quantum Electron.*, 17(10):2067–2072, 1981.

[22] N. Isenor. CO_2 laser-produced ripple patterns on Ni_xP_{1-x} surfaces. *Appl. Phys. Lett.*, 31(3):148–150, 1977.

[23] H. Leamy, G. Rozgonyi, T. Sheng, and G. Celler. Periodic regrowth phenomena produced by laser annealing of ion-implanted silicon. *Appl. Phys. Lett.*, 32(9):535–537, 1978.

[24] H. van Driel, J. Sipe, and J. Young. Laser-induced periodic surface structure on solids: A universal phenomenon. *Phys. Rev. Lett.*, 49(26):1955–1959, 1982.

[25] M. Couillard, A. Borowiec, H. K. Haugen, J. S. Preston, E. M. Griswold, and G. A. Botton. Subsurface modifications in indium phosphide induced by single and multiple femtosecond laser pulses: A study on the formation of periodic ripples. *J. Appl. Phys.*, 101(3):033519, 2007.

[26] D. Dufft, A. Rosenfeld, S. K. Das, R. Grunwald, and J. Bonse. Femtosecond laser-induced periodic surface structures revisited: A comparative study on ZnO. *J. Appl. Phys.*, 105(3):034908, 2009.

[27] A. Borowiec and H. K. Haugen. Subwavelength ripple formation on the surfaces of compound semiconductors irradiated with femtosecond laser pulses. *Appl. Phys. Lett.*, 82(25):4462–4464, 2003.

[28] F. Costache, M. Henyk, and J. Reif. Modification of dielectric surfaces with ultra-short laser pulses. *Appl. Surf. Sci.*, 186(1-4):352–357, 2002.

[29] F. Costache, M. Henyk, and J. Reif. Surface patterning on insulators upon femtosecond laser ablation. *Appl. Surf. Sci.*, 208-209:486–491, 2003.

[30] E. M. Hsu, T. H. R. Crawford, H. F. Tiedje, and H. K. Haugen. Periodic surface structures on gallium phosphide after irradiation with 150 fs–7 ns laser pulses at 800 nm. *Appl. Phys. Lett.*, 91(11):111102, 2007.

[31] Y. Shimotsuma, P. G Kazansky, J. Qiu, and K. Hirao. Self-organized nanogratings in glass irradiated by ultrashort light pulses. *Phys. Rev. Lett.*, 91(24):247405, 2003.

[32] J. Liu. Simple technique for measurements of pulsed gaussian-beam spot sizes. *Opt. Lett.*, 7(5):196–198, 1982.

[33] S. E. Kirkwood, A. C. van Popta, Y. Y. Tsui, and R. Fedosejevs. Single and multiple shot near-infrared femtosecond laser pulse ablation thresholds of copper. *Appl. Phys. A*, 81(4):729–735, 2005.

[34] D. Puerto, W. Gawelda, J. Siegel, J. Solis, and J. Bonse. Erratum: "Plasma formation and structural modification below the visible ablation threshold in fused silica upon femtosecond laser irradiation" [Appl. Phys. Lett. 91, 082902 (2007)]. *Appl. Phys. Lett.*, 92(21):219901–2, 2008.

[35] A. Borowiec, H.F. Tiedje, and H. K. Haugen. Wavelength dependence of the single pulse femtosecond laser ablation threshold of indium phosphide in the 400-2050 nm range. *Appl. Surf. Sci.*, 243(1-4):129–137, 2005.

[36] E. M. Hsu. Study of ultrashort pulse laser induced surface ripples and investigation of other applications of ultrashort pulse laser micromachining and ablation. Master's thesis, McMaster University, Hamilton, Ontario, October 2007.

[37] C. Byvik and A. Buoncristiani. Analysis of vibronic transitions in titanium doped sapphire using the temperature of the fluorescence spectra. *IEEE J. Quantum Electron.*, 21(10):1619–1624, 1985.

[38] P. Lacovara, L. Esterowitz, and M. Kokta. Growth, spectroscopy, and lasing of titanium-doped sapphire. *IEEE J. Quantum Electron.*, 21(10):1614–1618, 1985.

[39] Spectra Physics Inc. *User's Manual: Tsunami Mode-locked Ti:Sapphire Laser, Part Number 0000-232A, Rev. B*, December 1999.

[40] L. E. Hargrove, R. L. Fork, and M. A. Pollack. Locking of He-Ne laser modes induced by synchronous intracavity modulation. *Appl. Phys. Lett.*, 5(1):4–5, 1964.

[41] R. Y. Chiao, E. Garmire, and C. H. Townes. Self-trapping of optical beams. *Phys. Rev. Lett.*, 13(15):479–482, 1964.

[42] J. Squier, F. Salin, G. Mourou, and D. Harter. 100-fs pulse generation and amplification in Ti:Ai_2O_3. *Opt. Lett.*, 16(5):324–326, 1991.

[43] D. Strickland and G. Mourou. Compression of amplified chirped optical pulses. *Opt. Commun.*, 56(3):219–221, 1985.

[44] Spectra Physics Inc. *User's Manual: Spitfire Multikilohertz Pulsed Ti:Sapphire Amplifier with Pulse Stretcher and Compressor.*

[45] F. Salin, P. Georges, G. Roger, and A. Brun. Single-shot measurement of a 52-fs pulse. *Appl. Opt.*, 26(21):4528–4531, 1987.

[46] L. Giannuzzi, B. Kempshall, S. Schwarz, J. Lomness, B. Prenitzer, and F. Stevie. FIB lift-out specimen preparation techniques. *Introduction to Focused Ion Beams*, pages 201–228, 2005.

[47] R. M. Langford and A. K. Petford-Long. Preparation of transmission electron microscopy cross-section specimens using focused ion beam milling. *J. Vac. Sci. Technol. A*, 19(5):2186–2193, 2001.

[48] L. S. Hounsome, R. Jones, P. M. Martineau, D. Fisher, M. J. Shaw, P. R. Briddon, and S. Oberg. Origin of brown coloration in diamond. *Phys. Rev. B*, 73(12):125203, 2006.

[49] D. Ramanathan and P. Molian. Micro- and sub-micromachining of type IIa single crystal diamond using a ti:sapphire femtosecond laser. *J. Manuf. Sci. Eng.*, 124(2):389–396, 2002.

[50] S. Preuss and M. Stuke. Subpicosecond ultraviolet laser ablation of diamond: Nonlinear properties at 248 nm and time-resolved characterization of ablation dynamics. *Appl. Phys. Lett.*, 67(3):338–340, 1995.

[51] M. Shinoda, K. Saito, T. Kondo, A. Nakaoki, M. Furuki, M. Takeda, M. Yamamoto, T. J. Schaich, B. M. Van Oerle, H. P. Godfried, P. A. C. Kriele, E. P. Houwman, W. H. M. Nelissen, G. J. Pels, and P. G. M. Spaaij. High-density near-field readout using diamond solid immersion lens. *Jpn. J. Appl. Phys.*, 45(No. 2B):1311–1313, 2006.

[52] G. Dumitru, V. Romano, H.P. Weber, M. Sentis, and W. Marine. Femtosecond ablation of ultrahard materials. *Appl. Phys. A*, 74(6):729–739, 2002.

[53] N. Boling, M. Crisp, and G. Dubé. Laser induced surface damage. *Appl. Opt.*, 12(4):650–660, 1973.

[54] J. Bonse, G. Bachelier, J. Siegel, J. Solis, and H. Sturm. Time- and space-resolved dynamics of ablation and optical breakdown induced by femtosecond laser pulses in indium phosphide. *J. Appl. Phys.*, 103(5):054910–6, 2008.

[55] J. Bonse, S. Wiggins, and J. Solis. Ultrafast phase transitions after femtosecond laser irradiation of indium phosphide. *J. Appl. Phys.*, 96(5):2628–2631, 2004.

[56] P. Stampfli and K. Bennemann. Theory for the instability of the diamond structure of Si, Ge, and C induced by a dense electron-hole plasma. *Phys. Rev. B*, 42(11):7163, 1990.

[57] N. Stojanovic, D. von der Linde, K. Sokolowski-Tinten, U. Zastrau, F. Perner, E. Forster, R. Sobierajski, R. Nietubyc, M. Jurek, D. Klinger, J. Pelka, J. Krzywinski, L. Juha, J. Cihelka, A. Velyhan, S. Koptyaev, V. Hajkova, J. Chalupsky, J. Kuba, T. Tschentscher, S. Toleikis, S. Dusterer, and H. Redlin. Ablation of solids using a femtosecond extreme ultraviolet free electron laser. *Appl. Phys. Lett.*, 89(24):241909–3, 2006.

[58] T. Malinauskas, K. Jarasiunas, E. Ivakin, V. Ralchenko, A. Gontar, and S. Ivakhnenko. Optical evaluation of carrier lifetime and diffusion length in synthetic diamonds. *Diamond Relat. Mater.*, 17(7-10):1212–1215, 2008.

[59] D. Ashkenasi, R. Stoian, and A. Rosenfeld. Single and multiple ultrashort laser pulse ablation threshold of Al_2O_3 (corundum) at different etch phases. *Appl. Surf. Sci.*, 154-155:40–46, 2000.

[60] D. von der Linde and K. Sokolowski-Tinten. The physical mechanisms of short-pulse laser ablation. *Appl. Surf. Sci.*, 154-155 IS -:1–10, 2000.

[61] V. P. Ageev, L. L. Bullov, V. I. Konov, A. V. Kuzmichev, S. M. Pimenov, A. M. Prokhorov, V. G. Ralchenko, B. V. Spitsyn, and B. I. Chapliev. Interaction of laser light with diamond films. *Sov. Phys. Dokl.*, 33(11):840–842, 1988.

[62] A. Ozkan, A. Malshe, T. Railkar, W. Brown, M. Shirk, and P. Molian. Femtosecond laser-induced periodic structure writing on diamond crystals and microclusters. *Appl. Phys. Lett.*, 75(23):3716–3718, 1999.

[63] Q. Wu, Y. Ma, R. Fang, Y. Liao, Q. Yu, X. Chen, and K. Wang. Femtosecond laser-induced periodic surface structure on diamond film. *Appl. Phys. Lett.*, 82(11):1703–1705, 2003.

[64] H. Jeschke, M. Garcia, and K. Bennemann. Microscopic analysis of the laser-induced femtosecond graphitization of diamond. *Phys. Rev. B*, 60(6):R3701, 1999.

[65] M. Shinoda, R. R. Gattass, and E. Mazur. Femtosecond laser-induced formation of nanometer-width grooves on synthetic single-crystal diamond surfaces. *J. Appl. Phys.*, 105(5):053102, 2009.

[66] M. Huang, F. Zhao, Y. Cheng, N. Xu, and Z. Xu. Mechanisms of ultrafast laser-induced deep-subwavelength gratings on graphite and diamond. *Phys. Rev. B*, 79(12):125436–9, 2009.

[67] N. Yasumaru, K. Miyazaki, and J. Kiuchi. Fluence dependence of femtosecond-laser-induced nanostructure formed on TiN and CrN. *Appl. Phys. A*, 81(5):933–937, 2005.

[68] Q. Sun, H. Jiang, Y. Liu, Y. Zhou, H. Yang, and Q. Gong. Effect of spherical aberration on the propagation of a tightly focused femtosecond laser pulse inside fused silica. *J. Opt. A: Pure Appl. Opt.*, 7(11):655–659, 2005.

[69] N. Huot, R. Stoian, A. Mermillod-Blondin, C. Mauclair, and E. Audouard. Analysis of the effects of spherical aberration on ultrafast laser-induced refractive index variation in glass. *Opt. Express*, 15(19):12395–12408, 2007.

[70] V. P. Kandidov, A. Dormidonov, O. G. Kosareva, S. L. Chin, and W. Liu. Self-focusing and filamentation of powerful femtosecond laser pulses. *Self-focusing: Past and Present*, pages 371–398, 2009.

[71] R. Telling, C. Pickard, M. Payne, and J. Field. Theoretical strength and cleavage of diamond. *Phys. Rev. Lett.*, 84(22):5160, 2000.

[72] T. V. Kononenko, M. Meier, M. S. Komlenok, S. M. Pimenov, V. Romano, V. P. Pashinin, and V. I. Konov. Microstructuring of diamond bulk by IR femtosecond laser pulses. *Appl. Phys. A*, 90(4):645–651, 2008.

[73] V. N. Strekalov, V. I. Konov, V. V. Kononenko, and S. M. Pimenov. Early stages of laser graphitization of diamond. *Appl. Phys. A*, 76(4):603–607, 2003.

[74] E. M. Hsu, T. H. R. Crawford, C. Maunders, G. Botton, and H. K. Haugen. Cross-sectional study of periodic surface structures on gallium phosphide induced by ultrashort laser pulse irradiation. *Appl. Phys. Lett.*, 92(22):221112–3, 2008.

[75] H. Furukawa and M. Hashida. Simulation on femto-second laser ablation. *Appl. Surf. Sci.*, 197-198:114–117, 2002.

[76] H. Jeschke, M. Garcia, and K. Bennemann. Theory for the ultrafast ablation of graphite films. *Phys. Rev. Lett.*, 87(1):015003, 2001.

[77] C. Cheng, A. Q. Wu, and X. Xu. Molecular dynamics simulation of ultrafast laser ablation of fused silica. *J. Phys. Conf. Ser.*, 59:100–104, 2007.

[78] M. Perry, B. Stuart, P. Banks, M. Feit, V. Yanovsky, and A. Rubenchik. Ultrashort-pulse laser machining of dielectric materials. *J. Appl. Phys.*, 85(9):6803–6810, 1999.

[79] A. Kaiser, B. Rethfeld, M. Vicanek, and G. Simon. Microscopic processes in dielectrics under irradiation by subpicosecond laser pulses. *Phys. Rev. B*, 61(17):11437, 2000.

[80] J. Bonse, J. Wrobel, K. Brzezinka, N. Esser, and W. Kautek. Femtosecond laser irradiation of indium phosphide in air: Raman spectroscopic and atomic force microscopic investigations. *Appl. Surf. Sci.*, 202(3-4):272–282, 2002.

5359 12